PTB bericht Opt-75
Wissenschaftliche Veröffentlichungen
Dezember 2014

Dissertation

Tatsiana Wiegner

High Accuracy Measurements of Standard Reflection Materials and Goniochromatic Effect Pigments

ISSN 0341-6712
ISBN 978-3-95606-139-4

Physikalisch-Technische Bundesanstalt

Optik
PTB-Opt-75
Braunschweig, Dezember 2014

Tatsiana Wiegner

High Accuracy Measurements of Standard Reflection Materials and Goniochromatic Effect Pigments

Von der Fakultät für Elektrotechnik, Informationstechnik, Physik der Technischen Universität Carolo-Wilhelmina zu Braunschweig genehmigte Dissertation

ISSN 0341-6712
ISBN 978-3-95606-139-4

HIGH ACCURACY MEASUREMENTS OF STANDARD REFLECTION MATERIALS AND GONIOCHROMATIC EFFECT PIGMENTS

Von der Fakultät für Elektrotechnik, Informationstechnik, Physik
der Technischen Universität Carolo–Wilhelmina
zu Braunschweig
zur Erlangung des Grades einer
Doktorin der Naturwissenschaften
(Dr. rer. nat.)

genehmigte
D i s s e r t a t i o n

von **Tatsiana Wiegner** (geb. **Atamas**)
aus Baranovichi, Weißrussland

1. Referent: Hon.–Prof. Dr. Stefan Kück
2. Referent: Prof. Dr. rer. nat. habil. Andreas Waag

eingereicht am:	5 Mai 2014
mündliche Prüfung (Disputation) am:	22 September 2014

Braunschweig, 2014

PREFACE

The research work presented in this thesis was carried out in the Reflection and Transmission working group 4.24 in the Physikalisch–Technische Bundesanstalt (PTB) in Braunschweig during 2010 – 2013.
I am most grateful to my supervisors, Prof. Stefan Kück and Prof. Andreas Waag, for their help, guidance and support provided during the development of the research project.
I wish to express my gratitude to Dr. Andreas Höpe, the leader of the Reflection and Transmission working group for the opportunity to widen my knowledge in the field of optical reflectometry and optical metrology, for the discussion of the work process and results, for sharing with me his knowledge and providing many useful references. I appreciate Dr. Saulius Nevas for stray–light measurements, as well as helpful and useful discussions. I am grateful to Dr. Alfred Schirmacher and Mrs. Eva Velke for measurements of transmittance of the neutral density filter for my experimental facility.
I would like to thank all the members of the Reflection and Transmission group: Mr. Kai–Olaf Hauer, Mr. Dirk Hünerhoff, Mr. Sven Teichert and Mr. Bernd Campe, for their help provided and for sharing their experience during these years with me.
I am grateful for the financial grant from the International Graduate School Braunschweig (IGSM–Braunschweig) for the first year of the research project.
Finally, I am deeply thankful and profoundly grateful to my parents, my sister and my husband for their love, care, patience, and encouragement during yeasr of study. I would have never the chance to achieve many things without their support.

ABSTRACT

In this thesis a new facility named 3D Appearance Robot–based Gonioreflectometer (ARGon^3) for measurements of the spectral radiance factor and bidirectional reflectance–distribution function is built up and described. The ARGon^3 enables high precision goniometric measurements of diffuse reflecting materials within the whole hemispheric range above the surface of the sample. The wavelength range of the facility is 350 nm to 1100 nm. This new facility was compared with the Gonioreflectometer of the Physikalisch–Technische Bundesanstalt (PTB), which is used for calibration of diffuse reference reflection materials. The new measurement facility is established with the opportunity of absolute measurements of the spectral radiance factor with photodiode and with charge–coupled device (CCD) line–scan camera, the last one allows to make the measurements in reasonably short time. The calculation of the measurement uncertainty of the spectral radiance factor for both configurations of the ARGon^3 facility is introduced in this thesis. The investigation of the non–Lambertian reflection behavior of diffuse standard reflection materials is presented. The reflection behavior of five different materials has been studied. The investigation of the samples is presented for three wavelengths, i.e. 400 nm, 550 nm and 700 nm, for the whole hemispheric range above the surface of the sample for four incident irradiation angles.

This work contains the description of the optical properties and of the colour of special effect pigments, so–called goniochromatic effect pigments, which have rather wide application in automotive, printing, plastics and cosmetics industries. The spectral radiance factor of goniochromatic effect pigments describes the dependence of the optical properties on the geometric configuration of the light source and detector relative to the sample normal.

This thesis presents studies on accurate surface colour measurements. The results of the investigation of the different effect pigments are presented and discussed for different geometrical configurations according to the recommendations of American Society for Testing and Materials (ASTM) and Deutsche Industrie Norm (DIN). The uncertainty of colour measurements is also presented.

KURZFASSUNG

Diese Arbeit beschreibt die Entwicklung des "3D Appearance Robot–based Gonioreflectometer" (ARGon^3), das für die Messung des spektralen Strahldichtefaktors und der bidirektionalen Reflektanzverteilungsfunktion verwendet wird. Das ARGon^3 ermöglicht hochpräzise Messungen von diffus reflektierenden Materialien im gesamten Hemisphärenbereich oberhalb der Probe. Der Spektralbereich der Messapparatur beträgt 350 nm bis 1100 nm. Die neue Messapparatur wird mit dem Gonioreflektometer der Physikalisch–Technischen Bundesanstalt (PTB), welches für die Kalibrierung von diffus reflektierenden Materialien benutzt wird, verglichen. Das ARGon^3 wurde für absolute Messungen des spektralen Strahldichtefaktors entwickelt, welches zwei Messmöglichkeiten, mit Photodiode und CCD–Zeilenkamera, besitzt. Die Berechnungen der Messunsicherheit für beide Messkonfigurationen des ARGon^3 werden in dieser Arbeit beschrieben.

Das non–Lambertsche Reflektionsverhalten von diffus reflektierenden Materialien wird dargestellt. Weiterhin wurde das Reflektionsverhalten von fünf verschiedenen Materialen für drei Wellenlängen, 400 nm, 550 nm und 700 nm, untersucht. Der Strahldichtefaktor wurde für repräsentative geometrische Konfigurationen gemessen: 4 feste Einfallswinkel mit je 187 verschiedenen Reflektionswinkeln gleichmäßig verteilt über den Viertelraum oberhalb der Probe.

Die Arbeit beinhaltet die Beschreibung der optischen Eigenschaften und Farben von Effektpigmenten, sogenannte goniochromatische Effektpigmente, deren Anwendung in der Automobil–, Druck– sowie in der chemischen und kosmetischen Industrie weit verbreitet ist.

Diese Arbeit präsentiert die Untersuchung und die Ergebnisse der präzisen Farboberflächenmessungen und deren Messunsicherheiten. Dabei sind die von der American Society for Testing and Materials (ASTM) und Deutsche Industrie Norm (DIN) empfohlenen geometrischen Konfigurationen benutzt worden.

Contents

ABBREVIATIONS vii

MATHEMATICAL SYMBOLS ix

INTRODUCTION 1

SCIENTIFIC CONTRIBUTION 3

1 RADIOMETRY AND PHOTOMETRY 5

1.1 Quantities and Units of Radiometry and Photometry 6

1.2 Lambertian Source and Lambertian Surface 10

2 COLORIMETRY 13

2.1 Light Sources Quantities and Units of Radiometry and Photometry 13

2.2 Illuminants 14

2.3 Spectral Weighting Function 15

2.3.1 Spectral Response Function of the Human Eye 15

2.3.2 Colour-Matching Function and the CIE Standard Observer 17

2.3.3 The Y Tristimulus value 21

2.4 Colour Calculation from Spectral Data, Chromaticity Coordinates 21

2.5 Uniformity of Colour Spaces 24

2.5.1 Uniformity of the CIE Chromaticity Diagram 24

2.5.2 Uniform Colour Spacing and Colour Difference 24

3 INSTRUMENTAL SETUP 29

3.1 Light Sources of ARGon^3 30

3.2 Sample Alignment: 5–Axis–Robot 32

3.3 Rotation Stage 33

3.4 Detection System. Beam Profiling Optics 34

3.5 Monochromator 35

3.6 CCD Line–Scan Camera 36

3.6.1 Linearity of the CCD Line–scan Camera 37

3.7 High–Resolution Video Photometer System 40

4 RADIANCE FACTOR $\beta(\lambda)$ AND METHOD OF ITS MEASUREMENT 43

4.1 Reflection Standards 43
4.2 Method of Goniometric Measurements of the Spectral Radiance Factor $\beta(\lambda)$ 46
4.3 Uncertainty of Spectral Radiance Factor Measurements with ARGon^3. Scale Comparison 47
4.3.1 Uncertainty for the configuration photodiode–picoamperemeter . . 47
4.3.2 Uncertainty for ARGon^3 in CCD–configuration 51
4.3.2.1 Stray–light Effect 54
4.3.3 Scale Comparison 56

5 3D–MEASUREMENTS OF STANDARD REFLECTION MATERIALS 59

6 EFFECT PIGMENTS 67

6.1 Measurements of Reflection and Colour of Goniochromatic Effect Pigments 70
6.2 Polarization Effects in the Measurement of Reflection Properties of Effect Pigments 75
6.3 3D Colour Measurements 79

7 UNCERTAINTY OF COLOUR MEASUREMENTS 87

7.1 Propagation of the Uncertainty 87
7.2 Variance and Covariance Tristimulus Value 88
7.2.1 Matrix for the Variation and Covariation of Colour Values 89
7.3 Sensitivity Coefficient of Tristimulus Value 90
7.3.1 Sensitivity Matrix for (x, y, Y) Colour Coordinates 91
7.3.2 Sensitivity Matrix for CIELAB 91
7.4 Uncertainty of Colour Coordinates of Ceramic Matt Tiles 91

CONCLUSION 95

APPENDIX

APPENDIX A Wavelength adjustment of the line–scan camera CCD array 98

APPENDIX B 3D–Indikatix of Standard Reflection Materials 100

REFERENCES 116

List of Figures

1.1 The solid angle definition . . . 6
1.2 The luminous intensity of a point light source . . . 7
1.3 The illuminance . . . 8
1.4 The definition of the luminance . . . 9
1.5 Lambertian surface . . . 11

2.1 SPD of the illuminants A and D65 . . . 15
2.2 Human eye $V(\lambda)$–function . . . 16
2.3 The visual field . . . 17
2.4 Representative spectral sensitivity curves . . . 18
2.5 Colour matching functions $\overline{r}$, $\overline{g}$ and $\overline{b}$ . . . 19
2.6 Standard colour–matching functions $\overline{x}$, $\overline{y}$ and $\overline{z}$ . . . 20
2.7 Chromaticity diagram . . . 23
2.8 CIELAB colour space . . . 25
2.9 L*u*v* colour space . . . 26

3.1 ARGon^3 facility with focusing optics . . . 29
3.2 Sphere radiator . . . 30
3.3 Homogeneity of the sphere radiator . . . 31
3.4 SPD of ARGon^3 light sources . . . 31
3.5 RV–2AJ robot . . . 32
3.6 Geometry of measurements in the spherical coordinate system . . . 33
3.7 Focusing optics into the spectrometer . . . 34
3.8 CZ–monochromator . . . 35
3.9 Signals from the 1st and 2nd grating . . . 36
3.10 The efficiency of the 3rd grating in logarithmic scale . . . 37
3.11 The linearity deviation of the CCD array . . . 39
3.12 The linearity of CCD array via exposure time . . . 40
3.13 The photometric camera . . . 41
3.14 CMFs of the LMK–5 Color camera . . . 41
3.15 Spatially high resolved luminance distribution of an effect pigment . . . 42

4.1 Standard reflection materials . . . 44
4.2 Spectral radiance factor curves . . . 45
4.3 Measurement uncertainty ARGon^3 in photodiode–picoamperemeter config. . . . 50

4.4 Comparison Gonioreflectometer ARGon^3 facility in photodiode–picoamperemeter 51
4.5 Spectral radiance factor measured with ARGon^3 CCD–configuration 53
4.6 Stray–light correction 55
4.7 Comparison Gonioreflectometer with ARGon^3 in CDD–config. 56

5.1 3D–geometry configurations 60
5.2 Three–dimensional reflection indicatrix of the PRD 61
5.3 Three–dimensional reflection indicatrix of the BS 85–15 63
5.4 The "in–plane" reflection data of the BS 85–15 65

6.1 Spectral radiance factor $\beta(\lambda)$ of pigments 67
6.2 Colour diagram of typical absorption pigments 69
6.3 ASTM WK 1164 and DIN 6175–2 recommended geometries 70
6.4 Geometrical configurations for the measurement of colour traveling 71
6.5 Aspecular colour shift of the Viola Fantasy 72
6.6 Interference colour shift of the Viola Fantasy 73
6.7 Colour traveling of the Viola Fantasy with recommended geometries 74
6.8 Rochon Prism Polarizer 75
6.9 The polarization effect 76
6.10 a*b* colour data of the Viola Fantasy 78
6.11 L*a*b* colour data of different effect pigments 81
6.12 Viewing angle of ARGon^3 facility spherical light source 83
6.13 L*a*b* colour coordinates of the Viola Fantasy 84

A.1 Wavelength adjustment of the iHR–550 with CCD line–scan camera 99

B.1 Three–dimensional reflection indicatrix of A 07 101
B.2 The "in–plane" reflection indicatrix of A 07 103
B.3 Three–dimensional reflection indicatrix of OG A 5–14–01 105
B.4 The "in–plane" reflection indicatrix of OG A 5–14–01 107
B.5 Three–dimensional reflection indicatrix of Ceram#35 109
B.6 The "in–plane" reflection indicatrix of Ceram#35 111
B.7 Three–dimensional reflection indicatrix of PTBSRS–1 113
B.8 The "in–plane" reflection indicatrix of PTBSRS–1 115

List of Tables

2.1 Light Sources Classification 13

4.1 Uncertainty budget of ARGon^3 photodiode–picoamperemeter configuration . . . 48
4.2 Uncertainty budget of ARGon^3 CCD–configuration 52

6.1 L*a*b* colour coordinates of Viola Fantasy depending on polarization 78
6.2 Special effect MERCK pigments 79

7.1 The components of surface colour value uncertainty 92
7.2 Colour value of ceramic tile with uncertainty 93

A.1 Wavelength adjustment of the CCD array 98

ABBREVIATIONS

3D	three–dimensional
ADU	analog–to–digital units
A	illuminant A (blackbody radiator with a correlated colour temperature of 2856 K)
ARGon^3	3D Appearance Robot–based Gonioreflectometer
ASTM	American Society for Testing and Materials
$BaSO_4$	barium sulphate
BRDF	bidirectional reflectance distribution function
C	illuminant C (average day light with a correlated colour temperature of 6774 K)
CCD	charge–coupled device
CCT	correlated colour temperature
(x, y)**–diagram**	chromaticity diagram
CIE	International Commission on Illumination (Commission Internationale de l'Éclairage)
CIELAB	L*a*b* colour space
CMF	colour–matching function
CNC	computerized numerical control
CZ–monochromator	Czerny–Turner monochromator
d	diameter of the aperture of the spherical light source of the ARGon^3 facility
D65	illuminant D65 (day light with a correlated colour temperature of 6500 K)
DIN	Deutsche Industrie Norm
EM	electromagnetic radiation
ES	equi–energy stimulus
FFT	Full Frame Transfer
FWHM	full width at half maximum
GUM	Guide to the Expression of Uncertainty in Measurements

HDR	high dynamic range
ICMD	imaging colour measurement device
IDD	Institute of Printing Science and Technology of the Technische Universität Darmstadt
IGSM–Braunschweig	International Graduate School Braunschweig
ILMD	imaging luminance measurement device
ISO	International Organization for Standardization
LSF	line–spread function
ND filter	neutral density filter
NMI	National Metrological Institute
PLACOS	Pulsed Laser setup for Advanced Characterization of Spectrometers
PRD	perfectly reflecting diffuser
PTB	Physikalisch–Technische Bundesanstalt
PTFE	polytetrafluoroethylene
RGB	red, green, blue colour value
S_{DI}	incident dark signal
S_{DR}	reflection dark signal
S_{HI}	incident signal
S_{HR}	reflection signal
SPD	spectral power distribution
UCS	uniform colour scale diagram
UV–range	ultraviolet range of the light spectrum
$V(\lambda)$	spectral luminous efficiency function of the human eye
XYZ	XYZ colour space (XYZ colour system)

MATHEMATICAL SYMBOLS

A	area in m^2
a^*	redness, red to green (a^* value of CIELAB colour space)
α	scalar quantity
a^*_M	redness of perfect mirror
a, b, c	any three colour values
$A \cdot cos(\theta_i)$	projected solid angle Ω_i
b^*	yellowness, yellow to blue (b^* value of CIELAB colour space)
b	Wien Constant in $m \cdot K$
$\beta(\lambda)$	spectral radiance factor
$\overline{b}$	colour–matching function for blue–secretive sensor of the human eye
$\beta(\theta_i, \phi_i, \theta_r, \phi_r, \lambda)$	spectral radiance factor
B	blue
b^*_M	yellowness of perfect mirror
c_1	constant
c_2	constant
C^*_{ab}	chroma
c	velocity of light in vacuum in m/s
u'	chromaticity co–ordinate of uniform colour space
v'	chromaticity co–ordinate of uniform colour space
x	chromaticity co–ordinate
y	chromaticity co–ordinate
r	correlation coefficient
C_{Corr}	correction matrix
dA	area of the surface element
Δa^*	redness–greenness difference
Δb^*	yellowness–blueness difference
ΔC^*_{ab}	chroma difference
ΔE^*_{ab}	colour difference

Δ_i	i^{th} integral contribution
$\frac{\partial f}{\partial x_i}$	weighting coefficient (sensitivity coefficient)
$\frac{\partial f}{\partial x_j}$	weighting coefficient (sensitivity coefficient)
Δh^*_{ab}	hue angle difference
ΔH^*_{ab}	hue difference
R	distance to the point light source in m
ΔL^*	lightness difference
$d\lambda$	wavelength interval
$\Delta\lambda$	equally spaced interval
$d\Omega$	solid angle in sr
E_i	irradiance
E_ν	illuminance in lx
$E(\theta_i, \phi_i, \theta_r, \phi_r, \lambda)$	irradiance
f	function of the measured values
$f_r(\lambda)$	bi–directional reflectance distribution function (BRDF)
$\Phi_{e,\lambda}$	radiant flux in W
ϕ_i	azimuth incident angle in °
ϕ	azimuth angle of the cylindrical coordinate system
Φ_ν	luminous flux in lm
$\Phi_{\nu 0}$	luminous flux normal to the surface direction in lm
f_x	vector of sensitivity coefficients
G	geometrical extent
γ	spectral radiance factor of a “perfect mirror”
Γ	matrix denotes a suitably chosen regularization matrix
$\overline{g}$	colour–matching function for green–secretive sensor of the human eye
G	green
h	Planck Constant in $m^2 \cdot kg/c$
h^*_{ab}	hue angle in °
I	identity matrix
I_ν	luminous intensity in cd
$I_{\nu,\lambda}$	luminous intensity in cd
k	constant
K_m	photometric constant

K	constant
k	Boltzmann Constant in $J \cdot K^{-1}$
L^*	lightness (L^* value of CIELAB colour space)
L^*_M	lightness of perfect mirror
L^*_{PRD}	lightness of PRD
λ	wavelength in nm
L	luminance in cd/m^2, radiant power per small constant–wavelength interval
L_i	radiance of the radiator
λ_m	maximal wavelength in nm
λ_{max}	maximal wavelength in nm
L_ν	luminance in cd/m^2
L_r^{PRD}	radiance reflected by the PRD
L_S	linearity of the picoamperemeter
L_s	linearity of the CCD array
A	is the instrumental line–spread function in matrices form
$L(\theta_i, \phi_i, \theta_r, \phi_r, \lambda)$	radiance
$L(\theta_i, \phi_i, \theta_r, \phi_r)$	radiance
X	measured signal
Y	measured signal vector
N	number of independent variables
P	power
ϕ	azimuth angle in $^\circ$
ϕ_r	azimuth reflection angle in $^\circ$
ϕ_r	azimuth reflection angle in $^\circ$
θ	angle between the plane of the transmitted signal and the plane of oscillation of the electric vector of the incident light in $^\circ$
$P \cdot V$	radiant power
$q(\theta_i, \phi_i, \theta_r, \phi_r)$	radiance coefficient
Q_{abc}	sensitivity coefficient matrix
$Q_{e,\lambda}$	radiometric quantity
Q_ν	photometric quantity
Q	row sensitivity coefficient matrix for the output quantities in terms of each of the input quantities
R	sphere radius in m

R	distance between the radiator and surface
R	red
$R(\lambda)$	reflectance factor
$R(\theta_i)$	reflectance factor in °
$R(\lambda)$	spectral reflectance factor (or spectral radiance factor or spectral reflectance respectivety) of the object colour
$\overline{r}$	colour–matching function for red–secretive sensor of the human eye
ρ	reflectance
ρ	radial distance
SL	stray–light
$S(\lambda)$	SPD of the light source
$S(\lambda, T)$	radiation power of blackbody in W/m
T	temperature in K
θ	polar angle in °
θ	angle between the normal to the section and the direction of the light propagation in °
θ	direction angle in °
θ_r	aspecular reflection angle in °
θ_i	polar incident angle in °
θ_i	irradiation angle in °
θ_r	polar reflection angle in °
θ_r	reflection angle in °
θ_{rS}	specular reflection angle in °
S	transmitted light signal
S_2	minimum value of transmitted light signal
S_1	maximum value of transmitted light signal
$u^2(x_i)$	covariance with itself
U_x	input quantities
$u(x_i)$	uncertainty of the variable x_i
$u(x_i, x_j)$	covariance of component
$u(x_j)$	uncertainty of the variable x_j
$u(X, Y)$	covariance between two combinations
$u(X, Y)$	covariance between X and Y tristimulus value
U_{XYZ}	variance–covariance matrix

U_y	output quantities
$u(Y, Z)$	covariance between Y and Z tristimulus value
α	viewing angle in °
$V(\lambda)$	spectral luminous efficiency function of the human eye
$V(\lambda)$	spectral luminous efficiency function for photopic vision
$V'(\lambda)$	spectral luminous efficiency function for scotopic vision
X	tristimulus value in XYZ colour space
X	quantity of the function of the measured values
X	amount of X colour value
x_i	variable
x_j	variable
$\overline{x}(\lambda)$	colour–matching function for red–secretive sensor of the human eye
$\overline{x}_{10}$	colour–matching function for red–secretive sensor of the human eye with the visual field at 10°
X_n, Y_n, Z_n	white object colour stimulus
Y	tristimulus value in XYZ colour space
Y	quantity of the function of the measured values
Y	amount of Y colour value
Y_L	luminance of the colour in cd/m^2
$\overline{y}(\lambda)$	colour–matching function for green–secretive sensor of the human eye
$\overline{y}_{10}$	colour–matching function for green–secretive sensor of the human eye with the visual field at 10°
Z	tristimulus value in XYZ colour space
Z	amount of Z colour value
$\overline{z}(\lambda)$	colour–matching function for blue–secretive sensor of the human eye
$\overline{z}_{10}$	colour–matching function for blue–secretive sensor of the human eye with the visual field at 10°
z	height of the cylindrical coordinate system

INTRODUCTION

An object is visible because it reflects light, i.e. an interaction of the light with the matter takes place. Matter is able to change the propagation direction of the light waves. By the interaction with an object surface, light waves can undergo refraction, transmission, absorption or scattering. Two types of reflection take place. The first type is a specular reflection, in which of reflection is obtained for hard polished (shiny, varnished) surfaces (mirror, glass, lacquering). The second kind of reflection is a diffuse reflection, which is obtained from particulate substances. For instance, if you shine light on baking flour, you will not see a directionally shiny component. The baking flour will appear uniformly bright from every direction. Often a spread reflection, i.e. a combination of both diffuse and specular components (effect pigments and mostly natural materials) takes place [1]. An object has colour due to its wavelength–dependent reflection of the incident light. The colour measurement of objects is getting more and more relevant for many fields of industrial applications. The visual appearance of commercial products of paint, paper, printing, photography, textiles and plastics industries is significant for customer demands [2–4]. The absolute colour values of the sample is complicated to define, because we always deal with some approximations. Even the human eye is perceiving the colour of the objects not always in the same manner. This perception by the human eye depends on the age, gender, emotional and fatigue state of the human, illumination and many other factors. Colour is a sensation generated in the human brain. The eye is able to distinguish millions of colours, and thus colour measuring instruments should accurately match the sensitivity of the human eye [5]. The functionality of the colour perception process is only basically understood. We know just the basics of the sensory system of the human eye and the fact that human colour perception shows differences among people. A standard observer is needed to be defined and described in terms of the spectral response function of the reseptors of "standard" human eye. That was done at first in 1931 for a 2° field of view by two equivalent sets of colour matching functions. Likewise, in 1964 the standard observer has been defined for the 10° field of view. These sets of colour matching functions are used in industry [6].

The best accuracy in colour measurement can be achieved by the use of the method of the absolute measurement of the spectral radiance factor of the sample. The accuracy of this method may depend on different influencing factors such as non–linearity of detection,

wavelength error, dark level error, etc. More complex is the problem of the measurement of reflection and colour of samples used increasingly in modern industry, because modern technology allows nowadays to produce rather complex paints, pigments and surface effects. So the complexity of their accurate measurements is continually increased, that means, that the accuracy of the spectrophotometer used for colour measurement has to have be improved.

This work contains the description of the optical properties and colour of special effect pigments, so–called goniochromatic effect pigments, which have rather wide application in automotive, printing, plastics and cosmetics industries. In the thesis the colour characterization of goniochromatic effect pigments is presented. The spectral radiance factor of goniochromatic effect pigments describes the dependence of the optical properties on the geometric configuration of the light source and detector relative to the sample orientation.

This thesis presents studies on accurate surface colour measurements. Some basic theoretical backgrounds of photometry and colorimetry are introduced in **Chapter 1** and **Chapter 2**. In **Chapter 3** a new facility for measuring of the spectral radiance factor and visual appearance–related quantities is introduced: 3D Appearance Robot–based Gonioreflectometer (ARGon^3).

The colour of the sample can be calculated from its spectral radiance factor, the precise spectral radiance factor measurements is most important for many branches of industry. The method of spectral radiance factor measurements with estimated uncertainty for different configurations of the ARGon^3 is discussed and presented in **Chapter 4**. The ARGon^3 is able to absolute measure the spectral radiance factor of samples in two ways: measurements with photodiode–picoamperemeter and with CCD line–scan camera. The last one can be carried out very fast in comparison with the measurements with photodiode–picoamperemeter, but the uncertainty of this measurements is higher than the uncertainty of measurements of spectral radiance factor with photodiode–picoamperemeter. The measurements with CCD line–scan camera has the intention to carry out measurements in relative short time (for instance the spatial measurements of the spectral radiance factor).

The spatial three–dimensional (3D) measurements of the spectral radiance factor are presented in **Chapter 5** for the example of the pressed barium sulphate ($BaSO_4$) sample. In **Chapter 6**, the results of the investigation of the different effect pigments are presented and discussed for different geometrical configurations according to the recommendations of American Society for Testing and Materials (ASTM) and Deutsche Industrie Norm (DIN). The uncertainty of colour measurements is discussed in **Chapter 7**.

SCIENTIFIC CONTRIBUTION

This research work contains the following scientific results:

- A new 3D Appearance Robot–based Gonioreflectometer (ARGon^3) has been developed capable of measuring spectral radiance factors, respectively the bidirectional reflectance distribution function, in full $V(\lambda)$–range (360 nm to 830 nm) with arbitrary angles of irradiation and detection relative to the surface normal, on a sufficient short time scale of about 3 min for one measuring configuration. ARGon^3 is also capable to measure visual appearance–related quantities like colour coordinates, hue, chroma, lightness and color shift.

- The common assumption of Lambertian behavior of standard reflective materials was studied in 3D–measuring configuration for four incident angles of 0°, 22.5°, 45° and 67.5° and wavelengths of 400 nm, 550 nm and 700 nm. The deviation of all investigated materials from the perfectly reflecting diffuser (PRD) was investigated.

- The uncertainty of the measurements of colour coordinates for (x,y,Y) and CIELAB colour spaces measured with 3D Appearance Robot–based Gonioreflectometer are calculated with MatLab and presented in this work.

- The method of absolute measuring the spectral radiance factor was introduced, the uncertainty of the measurements of the spectral radiance factor has been derived for both ARGon^3 configurations.

- First goniometric measurements of diffuse reflection within 3D–space above the sample with subsequent colorimetric representation of the obtained data of special effect pigments based on the interference effect are introduced.

1 RADIOMETRY AND PHOTOMETRY

Radiometry is the science of measurement of electromagnetic radiation within the range of optical frequencies ($3 \cdot 10^{11}\,Hz$ to $3 \cdot 10^{16}\,Hz$, the wavelength range between 0.01 μm and 1000 μm). Radiometry investigates the electromagnetic radiation (EM) as it is emitted and detected, and measures values in connection with the radiation energy. The relevant quantities of radiometry are derivatives of Joules.
A radiation source in radiometry is assessed by the quantities associated with the radiant energy and flux (an average radiant power on the time scale much greater than the period of EM wave oscillation).
In photometry, on the other hand, the light source investigation is evaluated on the established human eye perception. The radiant flux estimated by the visual perception is called the luminous flux. Photometric assessments are based on the human eye perception of the radiation, while the system of terms and designations in radiometry is based on the energy assessment of the radiation.
The part of the electromagnetic spectrum, which can be detected by the human eye, is called light (i.e. the frequency range from about $3.61 \cdot 10^{14}\,Hz$ to about $8.33 \cdot 10^{14}\,Hz$, corresponding to a wavelength range from about 830 nm to 360 nm). For quantitative assessment of the light with respect to the human eye visual perception it is necessary to know the so–called spectral response function of the human eye.
The spectral luminous efficiency function of the human eye ($V(\lambda)$) is established by the International Commission on Illumination (CIE) and determined as spectral luminous efficiency function of the human eye [7].
The relation between radiometric and photometric quantities can be described by the following equation

$$Q_\nu = K_m \cdot \int_{380nm}^{830nm} Q_{e,\lambda} \cdot V(\lambda)\, d\lambda \tag{1.1}$$

where Q_ν is the photometric quantity, $Q_{e,\lambda}$ is the radiometric quantity, $V(\lambda)$ is the spectral luminous efficiency function of the human eye, K_m is the photometric constant.

The radiometric and photometric quantities are expressed by the light propagation in

space. The idea of solid angle is used for the characterization of the spatial direction of the radiation. The solid angle is the part of the space bounded by a conus.
The solid angle ($d\Omega$) is defined as the ratio of the spherical area with the center in the cone vertex to the surface element this cone boarded (Fig. 1.1).

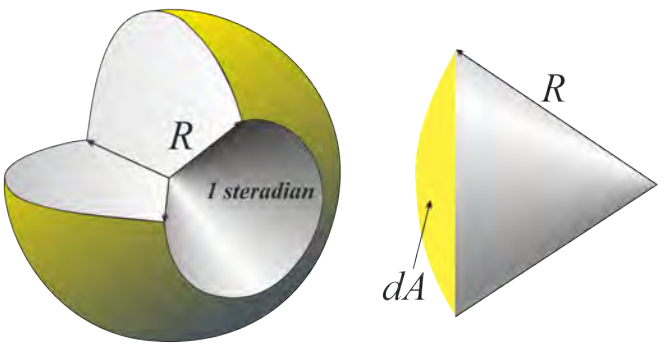

Figure 1.1: The solid angle definition [1]

The unit of the solid angle is the square area of the surface element (dA). The sphere floats the solid angle in

$$d\Omega = \frac{dA}{R^2} \tag{1.2}$$

where R is the sphere radius.

If the surface element is obtained in units of the solid angle, the area of this surface element is $dA = R^2$. The solid angle of the sphere is 4π. The unit of the solid angle is steradian [sr].

1.1 Quantities and Units of Radiometry and Photometry

The definitions in radiometry and photometry presume a point radiant source. This is a common and simple physical model of the radiant source (the geometrical size of a point light source is much smaller than the distance to the observer and its luminous intensity is the same in all directions). In an isotropic and homogeneous medium the wave emitted by the point light source is spherical.
The photometric equivalent of the radiance power is the luminous flux. It is defined as power emitted in unit of time evaluated to the spectral luminous efficiency functions of the human eye

$$\Phi_\nu = \int \Phi_{e,\lambda} \cdot V(\lambda) \cdot d\lambda \qquad [lm] \tag{1.3}$$

where $\Phi_{e,\lambda}$ is the radiant flux, Φ_ν is the luminous flux and $V(\lambda)$ is the spectral luminous efficiency function of the human eye.

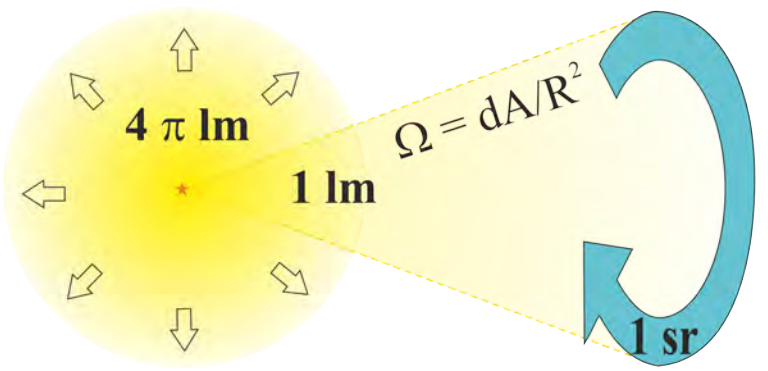

Figure 1.2: The luminous intensity of a point light source [1]

The luminous intensity is defined as the ratio of luminous flux to unit of the solid angle (Fig. 1.2)

$$I_\nu = \frac{d\Phi_\nu}{d\Omega} \qquad \left[\frac{lm}{sr}\right] \tag{1.4}$$

where I_ν is the luminous intensity, $d\Omega$ is the solid angle.
The luminous intensity is a function of polar and azimuth angle in a polar system of coordinates, so it depends on the direction of light propagation

$$I_\nu = I_\nu(\theta, \phi) \tag{1.5}$$

where I_ν is the luminous intensity, θ is the polar angle and ϕ is the azimuth angle.

If the luminous intensity of the point light source is independent of the direction of light propagation, this light source is isotropic. As the solid angle of the sphere is 4π, the luminous intensity of the light source in all directions of propagation is

$$I_\nu = \frac{\Phi_\nu}{4\pi} \tag{1.6}$$

where I_ν is the luminous intensity, Φ_ν is the luminous flux.

Equation (1.6) is assumed to be valid, if the size of the light source is not larger than approximately 10% of the distance to the illuminated surface area [7].

The influence of a light source on a detector depends only on the distance between them and on the detector area. A surface illuminated by a light source is characterized by its illuminance. The illuminance in a given direction at a given point of the surface is a ratio of the luminous flux to the surface area obtained in the solid angle contained the given direction of the light propagation.

$$E_\nu = \frac{d^2\Phi_\nu}{dA \cdot cos(\theta) \cdot d\Omega} \qquad [lx] \tag{1.7}$$

where dA is the area of the surface element of a section containing the given point, θ is the angle between the normal to the section and the direction of the light propagation and E_ν is the illuminance.

The illuminance and luminous intensity are closely related quantities. The relation between illuminance and luminous intensity can be established, considering a point light source S illuminating an area dA of the surface element with a distance to the point light source R between the light source and the surface (Fig. 1.3). The distance can be determined by the following equation

$$R^2 = dA \cdot cos(\theta) \tag{1.8}$$

where dA is the area of the surface element, θ is the angle between the normal to the section and the direction of the light propagation and R is the distance to the point light source.

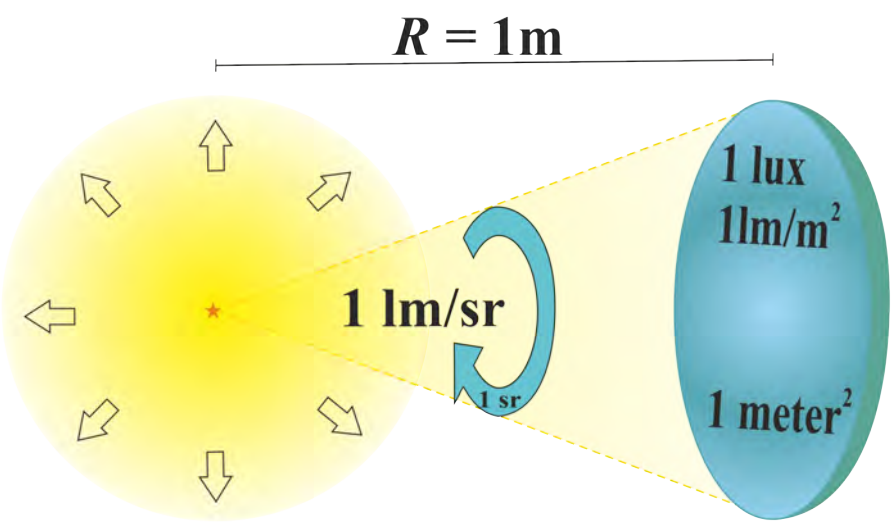

Figure 1.3: The illuminance [1]

From equation (1.4), (1.7) and (1.8) the illuminance the point light source is directly proportional to the luminous intensity ($I_{\nu,\lambda}$) and inversely proportional to the square distance to the point light source.

$$E_\nu = \frac{I_{\nu,\lambda}}{R^2} \qquad \left[\frac{lm}{m^2}\right] \tag{1.9}$$

where $I_{\nu,\lambda}$ is the luminous intensity, R is the distance to the point light source and E_ν is the illuminance.

Comparing the illuminance of two surface areas (A_1 and A_2) placed at distances (R_1 and R_2) from the point light source,

$$\frac{E_{\nu,1}}{E_{\nu,2}} = \frac{R_2^2}{R_1^2} \tag{1.10}$$

From (1.4) and (1.7), it follows that,

$$E_\nu \sim \frac{I_\nu}{cos(\theta)} \tag{1.11}$$

where θ is the angle between the normal to the section and the direction of the light propagation.

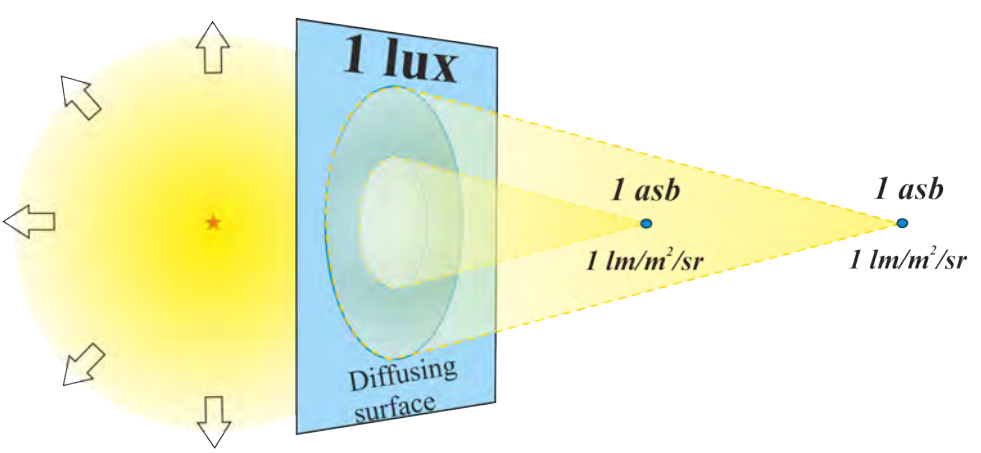

Figure 1.4: An illustration to the definition of the luminance [1]

The illuminance of the surface area is directly proportional to the cosine of the angle between the incident light and the normal to the surface. This is the Cosine(s) Law of

Illuminance. Illuminance created by a point light source on the surface area is directly proportional to the luminous intensity multiplied by cosine the angle between incident light and the normal to the surface and is inversely proportional to the square ratio of the distance between them.
Luminance describes the light emitted in a defined direction. The luminance is the ratio of the luminous flux transmitted by an elementary beam passing through a given point and expanded on a solid angle contained in the direction of expansion (Fig. 1.4).

$$\begin{aligned} L_\nu &= \frac{d^2\Phi_\nu}{dA \cdot cos(\theta) \cdot d\Omega} \\ &or \\ L_\nu &= \frac{dI_\nu}{dA \cdot cos(\theta)} \end{aligned} \tag{1.12}$$

where L_ν is the luminance, Φ_ν is the luminous flux, dA is the area of the surface element, $d\Omega$ is the solid angle, I_ν is the luminous intensity and θ is the direction angle.

1.2 Lambertian Source and Lambertian Surface

A source for which the luminance is equal in all directions of light propagation is called a Lambertian source [8].

$$L_\nu = Const \qquad \left[\frac{lm}{m^2 \cdot sr}\right] \tag{1.13}$$

where L_ν is the luminance.

A blackbody radiator is an appropriate model of a Lambertian light source. If a light source is not a point light source, i.e. it has a geometrical size, it is called a Lambertian surface. According to the Cosine Law of Luminance, the luminous flux emitted from the Lambertian surface in a plane $\phi = const$, in a solid angle $d\Omega$, is independent from the direction angle θ (Fig. 1.5)

$$\Phi_\nu = \Phi_{\nu 0} \cdot cos(\theta) \tag{1.14}$$

where $\Phi_{\nu 0}$ is the luminous flux normal to the surface direction, Φ_ν is the luminous flux, θ is the direction angle.

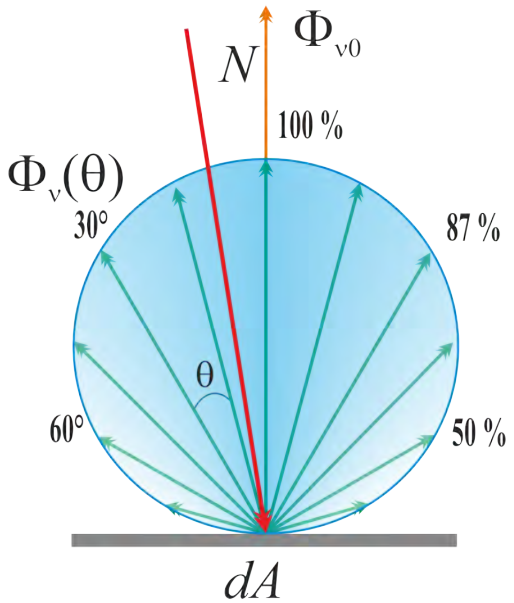

Figure 1.5: Lambertian surface

More data and details about the radiometric and photometric units and quantities can be found in [7, 9].

2 COLORIMETRY

Colorimetry as a scientific subject was established in 1924 at the 6th Session of the CIE in Geneva due to the increased demand from the industries and scientific laboratories in the measurement of color. The specifications of the main standards used in colorimetry are based on definitions of CIE.

2.1 Light Sources Quantities and Units of Radiometry and Photometry

Light sources can be divided in two categories, based on the mechanism of light generation (see Table 2.1) [10].

Table 2.1: Light Sources Classification

Artificial (technical) Light Sources		Natural Light Sources
Luminescence Radiator	Temperature Radiator	
Gas discharge tube, fluorescent lamps, LEDs, OLEDs, lasers	Blackbody radiator, incandescent lamps and arc lamps	Sunlight, light from other natural objects (stars) and etc.

The output distributions of optical radiation sources are compared with the spectral power distribution (SPD) of a blackbody radiator. An appropriate approximation of a blackbody is a cavity with a small aperture. The light coming through the aperture into the cavity will be almost completely absorbed by the walls of the cavity after multiple reflections. To approximate the SPD of the blackbody radiation the cavity is used in thermodynamic equilibrium at some given temperature T. If the temperature inside of the cavity increases, the output radiation will also increase and its frequency contents will change. The energy distribution depends on the wavelength of the blackbody radiation at some temperature T and is characterized by the radiation power (Planck's Law of Radiation) [11]

$$S(\lambda, T) \cdot d\lambda = \frac{c_1}{\lambda^5 \cdot (exp[\frac{c_2}{\lambda T}] - 1)} \tag{2.1}$$

where $S(\lambda, T)$ is the radiation power of blackbody, c_1 and c_2 are the constants:
$c_1 = 2\pi \cdot hc^2 = 3.74185 \cdot 10^{-16}\ W \cdot m^2$ and $c_2 = \frac{hc}{k} = 1.743884185 \cdot 10^{-12}\ m \cdot K$
where h is the Planck Constant, c is the velocity of light in vacuum, k is the Boltzmann Constant.

If the blackbody temperature increases, the SPD maximum shifts to shorter wavelengths. The product of the temperature corresponding to the maximum of the SPD and the wavelength is a constant (Wien's Displacement Law of Radiation)

$$\begin{aligned} \lambda_m \cdot T &= b \\ b &= 2.898 \cdot 10^{-3}\ m \cdot K \end{aligned} \tag{2.2}$$

where λ_m is the maximal wavelength, b is the Wien Constant and T is the temperature.

One of the defenition of the term color temperature was introduced by G.A Klein:

> "Because the color of the spectrum emitted by a blackbody radiator changes with temperature, it is useful to introduce the term color temperature. With this quantity, the emitted light of a source is compared with that of a blackbody radiator and thus characterized. The color temperature of an illuminant corresponds to the temperature of the blackbody radiator which emits the maximum of light at the same color as the actual illuminant. Strictly speaking, only a temperature radiator can be assigned a color temperature. Other optical radiators such as luminescence radiators are characterized by a so-called similar or correlated colour temperature." — *G.A Klein, Industrial Color Physics [12, p. 16].*

Usually tungsten filament lamps are used as temperature radiators. Their colour temperature varies in the range of 2800 K to 3000 K according to the applied voltage and the type of gas filling of the bulb. The group of discharge lamps and photoluminescence sources represent luminescence radiators. These radiators emit a line spectrum (discrete wavelengths) or a band spectrum. The temperature of luminescence lamps is lower than the surface temperature of the temperature radiators at the same colour temperature. A detailed description of these light sources can be found in [9, 11, 13].

2.2 Illuminants

CIE recommends theoretical light sources with tabulated relative spectral power distributions $S(\lambda, T)$. Usually their spectral power distribution is normalized to 550 nm. These

standardized light sources are called illuminants. Only two illuminants are established by the CIE as standard light sources for colorimetry which are illuminant A and illuminant D65 (Fig. 2.1).

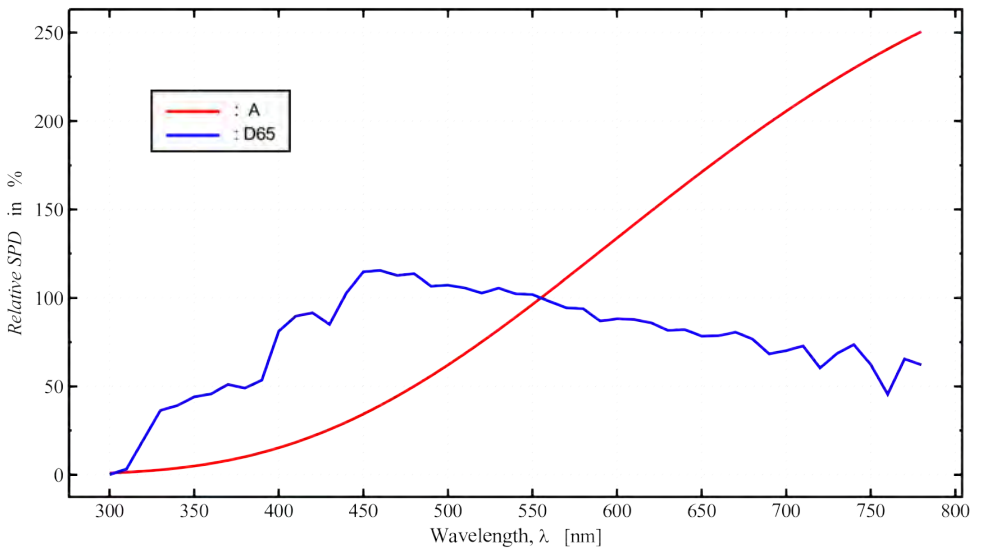

Figure 2.1: The spectral power distribution of standard the illuminants A and D65

Illuminant A represents the tungsten–filament lighting. The SPD of the illuminant A is that of a blackbody radiator at a temperature of about 2856 K. A disadvantage of this illuminant is its very low SPD in the short wavelength range. Illuminant A is applied in applications of colorimetry involving the use of incandescent lighting, unless there is no need to use another illuminants.
In 1964 CIE recommended a new average daylight light source — the illuminant D65. The SPD of illuminant D65 was defined similar to the SPD of diffuse daylight at midday on a cloudless northern sky with a correlated colour temperature (CCT) of 6500 K. All tabulated values for the illuminants A and D65 are given in units relative to the maximum of the spectral luminous efficiency function of human eye, according to the spectral response function of the human eye.

2.3 Spectral Weighting Function

2.3.1 Spectral Response Function of the Human Eye

The sensitivity of the eye to light for different wavelengths is given in Figure 2.2. The light–adapted spectral response of the eye is the spectral luminous efficiency function for photopic vision ($V(\lambda)$). The dark–adapted relative spectral response of the eye is the

spectral luminous efficiency function for scotopic vision ($V'(\lambda)$). The luminosity curve for photopic vision has a peak at 555 nm (in the yellow–green region). It is 50% at near 510 nm and 610 nm and runs off at about 380 nm and 780 nm (Fig. 2.2).

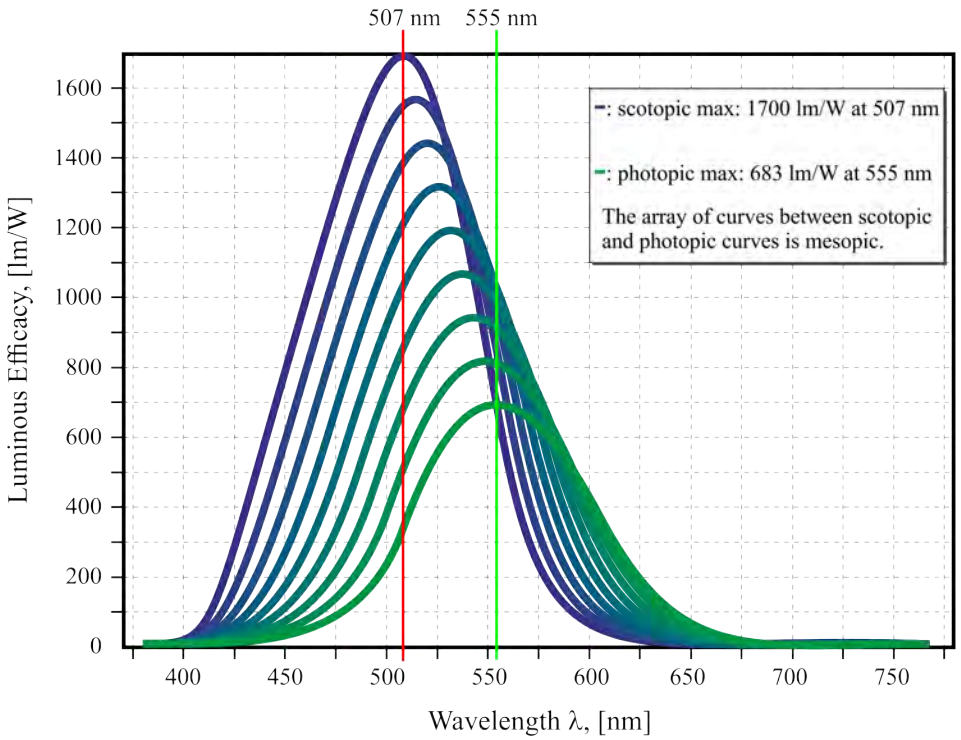

Figure 2.2: Spectral luminous efficiency function of the human eye

The maximum of the scotopic spectrum is shifted to shorter wavelengths compared to the photopic spectrum. The scotopic curve has a peak at 507 nm, reaches 50% at about 455 nm and 550 nm, and runs off at about 380 nm and 645 nm.
For a luminance higher than $3\,cd/m^2$, the photopic vision is active. Scotopic vision is active for a luminance lower than $0.01\,cd/m^2$. The vision between these values is the so–called mesopic vision (Fig. 2.2). More details about human colour vision can be found in [14].
Both spectral luminous efficiency functions of the human eye are normalized at the maximum sensitivity at wavelengths $\lambda_{max} = 555$ nm and 507 nm (sensitivity maximum for every function). These weighting functions for the photopic vision $V(\lambda)$ and for the scotopic vision $V'(\lambda)$ are used for colour evaluation.

2.3.2 Colour-Matching Function and the CIE Standard Observer

According to Young–Helmholtz colour vision theory [15, 16], a colour perception is the result of the excitation of the three–receptor light receivers in the retina of the human eye. Every receptor has its own maximum excitation in the short (Blue), medium (Green) and long wavelength (Red) part of the light spectrum. A calculation of colour from spectral power data uses the mentioned three receptor selectivity curves. It was experimental proven that the colour can be matched using three matching stimuli in mixture (the so–called trichromatic matches). For trichromatic matches, the angular size of the matching field must be specified. The view angle was defined at 2° for the first colour matching experiment (Fig. 2.3).

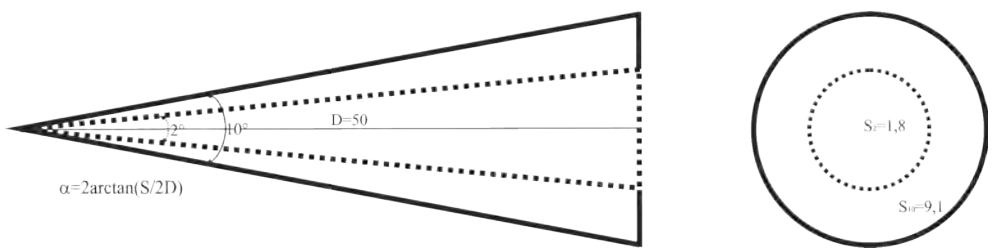

Figure 2.3: The visual field at 2° (dotted line) and 10° (solid line)

The perceived colours of red, green and blue were defined at wavelengths 700 nm, 546.1 nm and 435.8 nm, respectively (the so–called colour matching stimuli) (Fig. 2.4). For instance, as described by R.W.G. Hunt and R.M. Pointer in [17, p.27],:

> "to match 5.650 cd/m^2 of a white light composing of equal amounts of power per small constant–width wavelength interval throughout the spectrum (a stimulus known as the equi–energy stimulus (ES)), the amounts of these red, green and blue matching stimuli are:

Red	1.000	cd/m^2
Green	5.5907	cd/m^2
Blue	0.0601	cd/m^2
Mixture	5.6508	cd/m^2

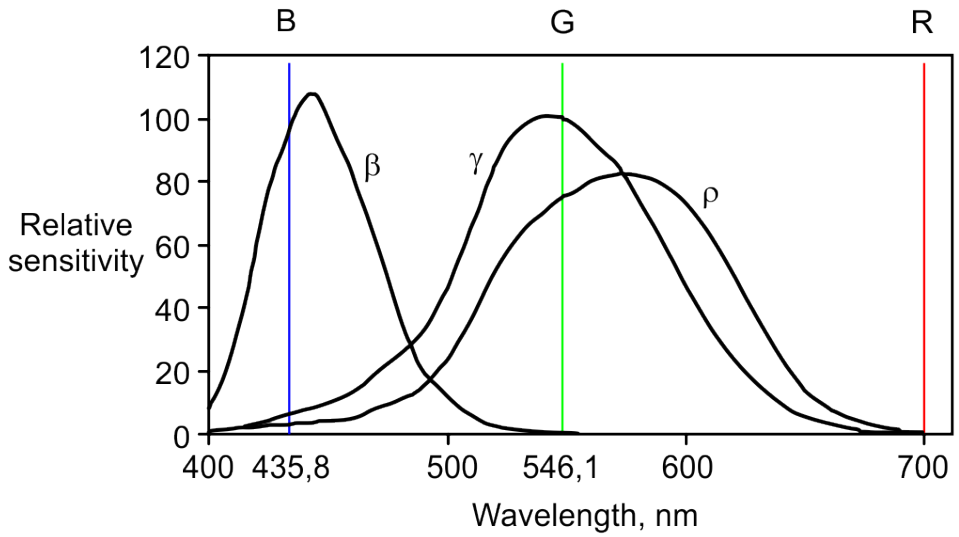

Figure 2.4: *Hunt, Pointer, Measuring Colours, [17, p. 28]*: *"Representative spectral sensitivity curves of the three different types of the cone in the retina, together with the wavelengths R,G and B use for defining the cie 1931 Standard Colorimetric Observer,* $700\,nm$*,* $546.1\,nm$ *and* $435.8\,nm$*, respectively."*

But, because white is a colour that is not perceptually biased to either red, green, or blue. It was decided to measure the amount of green in a unit that was $4.5907\,cd/m^2$, and the amount of blue in a unit that was $0.0601\,cd/m^2$. The match for $\mathbf{5.6508}\,cd/m^2$ of **ES** is then represented by:

Red	1.000	cd/m^2
Green	1.000	*new green units*
Blue	1.000	*new blue units*"

Nowadays the amount of these three matching stimuli is called the red, green, blue colour value (RGB). The RGB expressed in terms of matching stimuli are the colour–matching functions (CMFs) [18], which was confirmed by the CIE 1931 Standard Colorimetric Observer (Fig. 2.5) [19–21]. The tristimulus value are evaluated as

$$\begin{aligned} R &= K \cdot (P_1 \cdot \overline{r}_1 + P_2 \cdot \overline{r}_2 + \cdots + P_n \cdot \overline{r}_n) \\ G &= K \cdot (P_1 \cdot \overline{g}_1 + P_2 \cdot \overline{g}_2 + \cdots + P_n \cdot \overline{g}_n) \\ B &= K \cdot (P_1 \cdot \overline{b}_1 + P_2 \cdot \overline{b}_2 + \cdots + P_n \cdot \overline{b}_n) \end{aligned} \tag{2.3}$$

where R is the red, G is the green, B is the blue, K_m is the photometric constant and P is an amount of power per small constant–width wavelength interval throughout the spectrum (radiant flux).

The quantities $\overline{r}$, $\overline{g}$ and $\overline{b}$ are the CMFs.

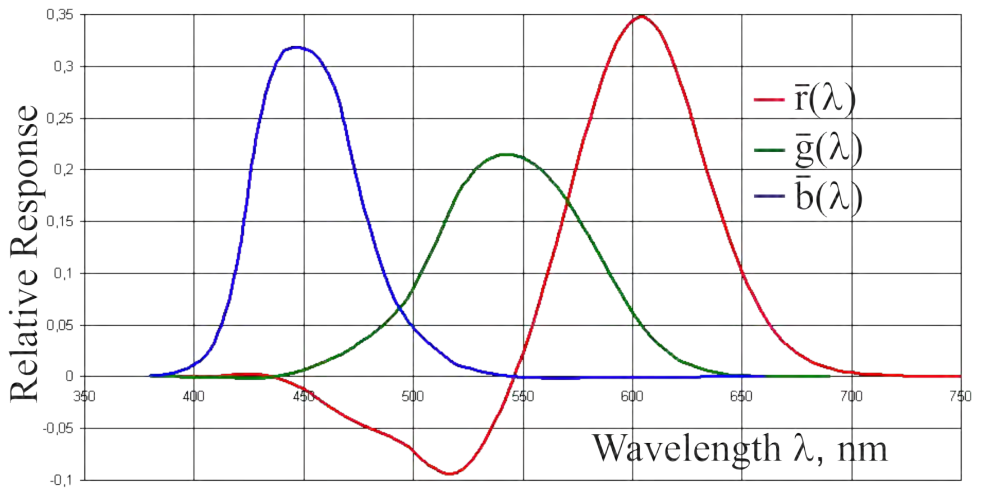

Figure 2.5: Colour matching functions $\overline{r}$, $\overline{g}$ and $\overline{b}$ in terms of spectral stimuli consisting of monochromatic stimuli of wavelength [21]

The luminance of the colour matched for these amounts of R, G and B is

$$L = 1.000 \cdot R + 5.5907 \cdot G + 0.0601 \cdot B \tag{2.4}$$

where L is the luminance, radiant power per small constant–wavelength interval.

In common ways, every colour perception can be computed accordingly to equations (2.3) and (2.4) [17].

$$L = K \cdot (P_1 \cdot V_1 + P_2 \cdot V_2 + \cdots + P_n \cdot V_n) \tag{2.5}$$

where the product $P \cdot V$ is the radiant power per small constant–width wavelength interval throughout the visible spectrum. K is the constant mentioned in equation (2.4).

$K = 683$ for the luminous flux in lumen for photopic vision, and K is given as $K_m = 1700$ for the luminous flux in lumen for scotopic vision. If the radiant flux is expressed in cd/m^2, the colour symbols are presented with the indices L for the luminance–related tristimulus values. According to the human perception, K was chosen so that $Y_L = 100$

for a PRD, which will be described in **Chapter 5**.
As can be found in literature, the values of R, G and B were computed by the method described before. They provide a system of colour values which is precise to the human eye. The presence of negative values in the CMFs leads to negative tristimulus colour values which is not suitable for colour specifications. In 1964 the CIE adopted the new system XYZ colour space (XYZ). This system avoids negative numbers in colour specification. These values are obtained by means of the equations

$$\begin{aligned} X &= 0.49 \cdot R + 0.31 \cdot G + 0.20 \cdot B \\ Y &= 0.17697 \cdot R + 0.81240 \cdot G + 0.01063 \cdot B \\ Z &= 0.00 \cdot R + 0.01 \cdot G + 0.99 \cdot B \end{aligned} \tag{2.6}$$

where X, Y, Z are tristimulus values and they are always positive for all colours.

The clear explanation of the coefficients in equation (2.6) is given in [17, p. 32–33]. From equation (2.6), it is possible to compute the $\overline{x}(\lambda)$, $\overline{y}(\lambda)$ and $\overline{z}(\lambda)$ colour–matching functions (CMFs) for the CIE 1931 colour space, where the visual field is 2° (Fig. 2.6).

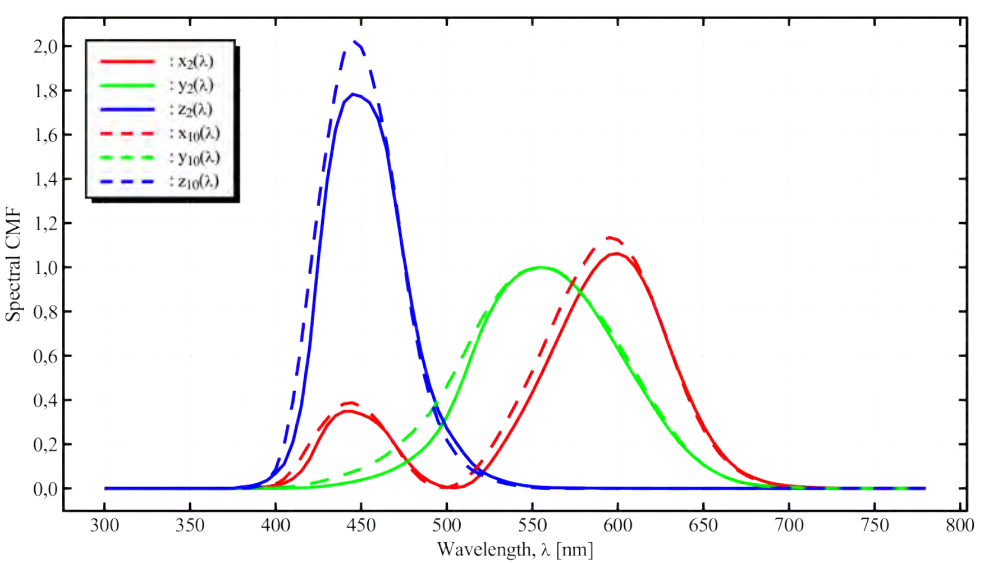

Figure 2.6: Standard colour–matching functions of the 2° (solid line) and 10° standard observer (dashed line) (CIE 1931 and CIE 1964 observer)

The colour match was done with a 2° field of view. If the viewing field size reduces, the ability of the retina to discriminate one colour from another also reduced. So the 2° provide an appropriate matching. From the other side, if the field of view increases, the colour discrimination also becomes more pronounced as matched at the 2° field. In 1964,

CIE recommended CMFs for the standard colorimetric observer with a field of view of 10°, $\overline{x}_{10}$, $\overline{y}_{10}$ and $\overline{z}_{10}$ [22].

2.3.3 The Y Tristimulus value

The Y_L tristimulus value represents the luminance of the colour if it is evaluated on an absolute basis (Y_L in cd/m^2) and supposing the luminance is approximately correlated to the brightness (brightness is a visual perception property according to which an area appears to represent more or less light). Y_L is 100 for the PRD. Y_L expresses the reflectance factor (the ratio of the radiant that is reflected in a given solid angle to the reflectance of the PRD identically irradiated in the same cone direction). Y_L ranges from 100 for a white object to 0 for a black objects that completely absorb light.

2.4 Colour Calculation from Spectral Data, Chromaticity Coordinates

To define the colour coordinates of an object, it is required to determine the matching stimuli according to their spectral components and the units in which the functions are measured. According to the Grassmann's law we can write the colour equation and calculate the colour [12]

$$[Colour] \equiv X \cdot [X] + Y \cdot [Y] + Z \cdot [Z] \tag{2.7}$$

where X, Y and Z are the values for $[X]$, $[Y]$ and $[Z]$ units used for the achievement of the colour match.

X, Y and Z values are calculated as

$$\begin{aligned} X &= k \cdot \int_{380nm}^{780nm} S(\lambda) \cdot R(\lambda) \cdot \overline{x}(\lambda)\, d\lambda \\ Y &= k \cdot \int_{380nm}^{780nm} S(\lambda) \cdot R(\lambda) \cdot \overline{y}(\lambda)\, d\lambda \\ Z &= k \cdot \int_{380nm}^{780nm} S(\lambda) \cdot R(\lambda) \cdot \overline{z}(\lambda)\, d\lambda \end{aligned} \tag{2.8}$$

where $S(\lambda)$ is the SPD of the light source, $R(\lambda)$ is the spectral reflectance factor of the object colour and the constant k depends on the chosen light source.

Due to the assumption that $\overline{y}(\lambda)$ is the identical to the light sensitivity of the human eye $V(\lambda)$, which is adjusted to the standard colour value Y and for the PRD $Y = 100$ for every illuminant and light source (the reflectance factor $R(\lambda) = 1$ for all wavelengths) and k is calculated by

$$k = \frac{100}{\int\limits_{380nm}^{780nm} S(\lambda) \cdot \overline{y}(\lambda)\, d\lambda} \tag{2.9}$$

where $S(\lambda)$ is the SPD of the light source, $\overline{y}(\lambda)$ is the colour–matching function for green–secretive sensor of the human eye, $d\lambda$ is the wavelength interval and λ is the wavelength.

As we know Y is correlated with the brightness or lightness. The X and Z values are not correlated with any perception attributes. The relative magnitudes of the tristimulus value are usually correlated. The relative tristimulus values are named chromaticity co–ordinates [17].

$$\begin{aligned} x &= \frac{X}{X+Y+Z} \\ y &= \frac{Y}{X+Y+Z} \\ z &= 1-(x+y) \end{aligned} \tag{2.10}$$

where x and y represent chromaticity.

According to [17], **chromaticity** is a property of a color stimulus. The chromaticity combines the hue and colorfulness.
In compliance with *International Lighting Vocabulary* [23], **Hue** is the attribute of visual perception according to which a surface appearers to be similar to one of the perceived colours (red, green, blue and yellow).
Colorfulness is the attribute of visual perception, according to which the perceived colour of the surface appears to be more or less chromatic.
For example if we have a sample with the following colour coordinates:

$X = 50 \qquad Y = 14 \qquad Z = 5 \quad$ the summ of colour coordinates is $\quad X + Z + Y = 69$

This indicates that the colour ratio is 72 % of X, 20 % of Y and 7 % of Z. It means that the sample is red with the following chromaticity coordinates
$x = 50/69 = 0.72 \quad y = 14/69 = 0.20 \quad z = 5/69 = 0.07$
The human eyes percive the colour of a sample like very colourfull and without any hue. Accordingly as described in the above example and assuming that white is the equi–

energy stimulus, the colour coordinates of white X, Y and Z are equal to 1, adequately the chromaticity co–ordinates x, y and z are coequal 1/3.
The chromaticity diagram shown in Fig 2.7 represents one of the colour maps. The limited horseshoe–line is the spectrum colour locus (spectrum locus), since the curve represents the wavelengths of the optical radiation range. The corresponding wavelength values are indicated along the curve in figure 2.7 in 20 nm intervals. The ends of the spectrum

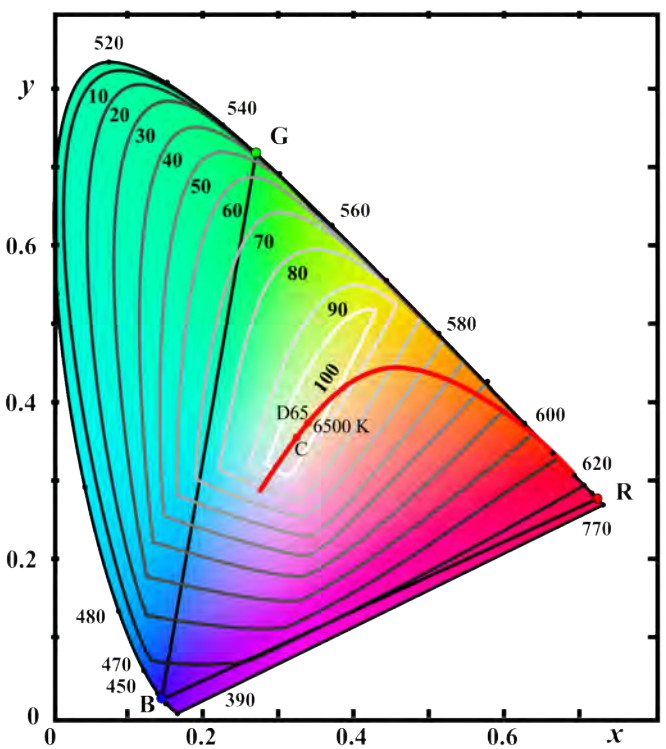

Figure 2.7: Chromaticity diagram with the CIE red green and blue matching stimuli

locus are joined at 380 nm and 780 nm of the spectrum locus (these points represent two original colours) by a straight line. This line expresses the additive colour mixing. Mixed colours represent the light mixture of the ends of the real optical spectrum, and is also called the purple boundary.
The chromaticity co–ordinates are enough to describe the chromaticity of a surface. For the description of its brightness (lightness) the colour value Y is used. The value Y lies in the interval from 100 to 0. The area in the spectrum locus of Fig. 2.7 runs off with increasing lightness, as a result the whole colours tend to the appropriate achromatic value until they become white. The volume hold by the surface extending along the lightness axes is the colour body. In this volume, it is possible to introduce whole colours with chromaticity coordinates except the ideal black.

The chromaticity points of the illuminants D65 and C are presented in Fig. 2.7 and the red curve is called the Planckian locus. This locus is determinated from the temperature-dependent Planck law of radiation. The colour coordinates of temperature radiators are located on this locus.

2.5 Uniformity of Colour Spaces

2.5.1 Uniformity of the CIE Chromaticity Diagram

The chromaticity diagram is widely used as a colour description system. The disadvantage is the non–uniform colour distribution in the diagram. MacAdam shows in [24] that the equal distance of the CIE chromaticity diagram does not correspond to the same visual differences. If we take in the chromaticity diagram two points, presenting two colours with the same luminance, but the perception for the human eye of these two points (colours) is different, and join these points with a straight line, it is revealed that the distances in the chromaticity diagram between such points have different magnitudes. These distances are called colour differences [25].
In the ideal case, identical colour differences will be represented by equidistance, but in the chromaticity diagram the colour difference in the green part is much longer, shorter in the blue range and in the violet part colour differences have an average length. Judd [25,26] in his work shows a possibility to find an approximation of a uniform colour plane. In the Judd's colour graphic the barely perceptible differences in colour correspond to almost the same distance for the diagram, the so–called CIE 1976 uniform colour scale diagram (UCS) or (CIE 1976 UCS diagram) [25, 27].
More information about color difference can be found in [17, p. 48–52].

2.5.2 Uniform Colour Spacing and Colour Difference

The CIE 1976 uniform colour scale diagram (UCS) is advised to use a transformation of the (x, y)–diagram yielding the colour spacing perceptually more uniform. The chromaticity diagram is produced by mapping u' as abscissa and v' as ordinate

$$\begin{aligned} u' &= \frac{4 \cdot X}{X + 15 \cdot Y + 3 \cdot Z} \\ v' &= \frac{9 \cdot Y}{X + 15 \cdot Y + 3 \cdot Z} \\ w' &= 1 - (u' + v') \end{aligned} \tag{2.11}$$

From CIE Publication 15:2004 [28]:

> "This diagram is intended to apply to comparisons of differences between object colours of the same size and shape, viewed in identical white to middlegrey surroundings, by an observer photopically adapted to a field of chromaticity not too different from that of average daylight."

In 1976, the CIELAB was recommended [29] which is also nearly equidistant. This system is based on the Munsell colour atlas [30]. The CIELAB system is based on the following colour values: lightness (L^*), or black to white contribution ($L^* = 50$ is grey), redness, red to green (a^*) – red to green contribution, yellowness, yellow to blue (b^*) – yellow to blue contribution (Fig. 2.8)

$$\begin{aligned} L^* &= 116 \cdot \left(\frac{Y}{Y_n}\right)^{\frac{1}{3}} - 16 \\ a^* &= 500 \cdot \left[\left(\frac{X}{X_n}\right)^{\frac{1}{3}} - \left(\frac{Y}{Y_n}\right)^{\frac{1}{3}}\right] \\ b^* &= 200 \cdot \left[\left(\frac{Y}{Y_n}\right)^{\frac{1}{3}} - \left(\frac{Z}{Z_n}\right)^{\frac{1}{3}}\right] \end{aligned} \tag{2.12}$$

where $X, Y\,Z$ are the colour stimulus considered and X_n, Y_n, Z_n are a specific white object colour stimulus (usually, it is the colour cordinates of the PRD).

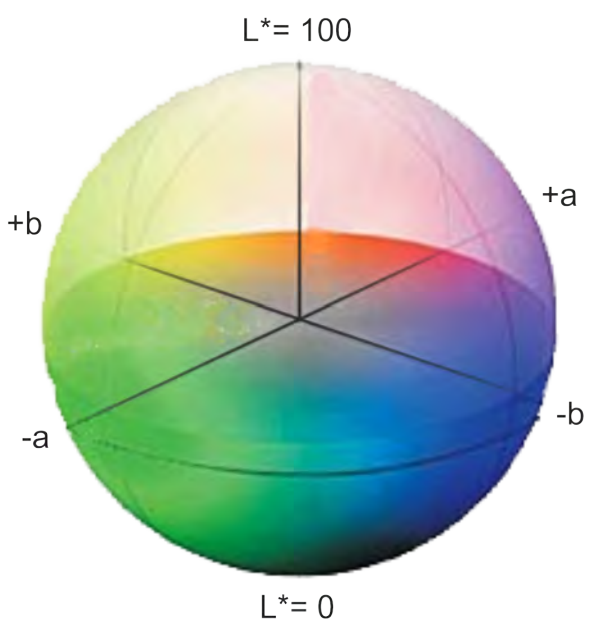

Figure 2.8: The CIELAB colour space

CIELab is a three–dimensional orthogonal coordinate system. The positive axes represents the achromatic colours with the $L^* = 0$ for ideal black and $L^* = 100$ for ideal white. a^*, b^* –colour plane of constant lightness demonstrates the chromatic contribution of the colour stimulus.

The properties of industrial products are often characterized by attributes such as lightness, chroma, hue or hue angle (Fig. 2.9). Following the CIELAB system, it is possible to visualize and quantify these attributes.

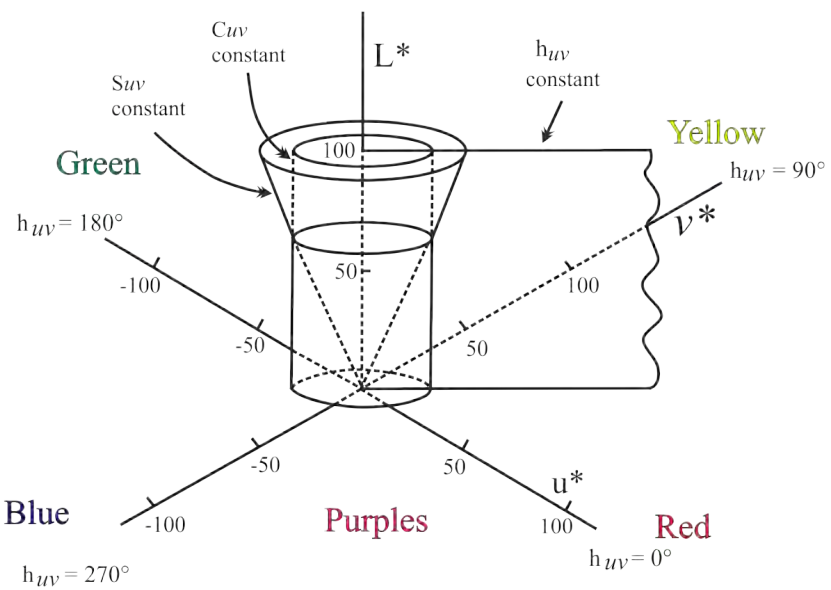

Figure 2.9: The CIELAB colour space with lightness, chroma and hue angle (with L*u*v* colour space)

$$C^*_{ab} = \sqrt{a^{*2} + b^{*2}} \qquad CIE\,1976 \quad a, b\ Chroma$$
$$h^*_{ab} = \frac{180^0}{\pi} \cdot arctan\left(\frac{b^*}{a^*}\right) \qquad CIE\,1976 \quad a, b\ Hue - angle \tag{2.13}$$

where C^*_{ab} is a radius of the cylinder or the difference between the achromatic points and h^*_{ab} is the azimuth angle or hue angle that describes the position of the colour point. The hue angle (h^*_{ab}) increases counter clockwise along the positive a^* axis.

(L^*,C^*_{ab},h^*_{ab}) is a cylindrical colour system. This system defines more colour points as in real absorption colour exist [17].
The perceptible differences in colour in the CIELAB colour diagram are nearly equidistant. The colour difference between a sample with the colour value L^*_S, a^*_S, b^*_S and the

reference colour with the value L^*_R, a^*_R, b^*_R is

$$\Delta L^* = L^*_S - L^*_R \quad = \begin{cases} > 0 : & \text{lighter} \\ < 0 : & \text{darker} \end{cases}$$

$$\Delta a^* = a^*_S - a^*_R \quad = \begin{cases} > 0 : & \text{redder} \\ < 0 : & \text{greener} \end{cases}$$

$$\Delta b^* = b^*_S - b^*_R \quad = \begin{cases} > 0 : & \text{yellower} \\ < 0 : & \text{bluer} \end{cases}$$

The colour difference (ΔE^*_{ab}) between two colour stimuli is calculated as the Euclidean distance between the points representing them in the space

$$\Delta E^*_{ab} = \sqrt{\Delta L^{*2} + \Delta a^{*2} + \Delta b^{*2}} \tag{2.14}$$

where ΔL^* is the lightness difference, Δa^* is the redness–greenness difference and Δb^* is the yellowness–blueness difference.
It is possible to express the colour difference through the lightness difference L^* and the hue difference ΔH^*_{ab}.

$$\Delta C^*_{ab} = C^*_{ab,S} + C^*_{ab,R} \tag{2.15}$$

where ΔC^*_{ab} is the chroma difference.

The chroma difference from a geometrical point of view provides the length difference of the cylinder radius between the colour value of the sample and the reference colour value. From the colorimetric point of view, this difference can be interpreted as

$$\Delta C^*_{ab} = \begin{cases} > 0 : \text{more brilliant, clearer} \\ < 0 : \text{duller, less chromatic} \end{cases}$$

The hue angle difference (Δh^*_{ab}) is

$$\Delta h^*_{ab} = h^*_{ab,S} - h^*_{ab,R} \tag{2.16}$$

as a result, the hue contribution ΔH^*_{ab} is defined by

$$\Delta H^*_{ab} = 2 \cdot \sqrt{\Delta C^*_{ab,S} \cdot C^*_{ab,R}} \tag{2.17}$$

Geometrically ΔE^*_{ab} is the chord length belonging to the chroma value of the sample from the reference chroma value. The additional colour difference equation is

$$\Delta E^*_{ab} = \sqrt{\Delta {L^*}^2 + \Delta {C^*_{ab}}^2 + \Delta {H^*_{ab}}^2} \tag{2.18}$$

3 INSTRUMENTAL SETUP

The setup of the ARGon^3 is illustrated in Figure 3.1. The facility includes three main parts: a rotation stage carrying the light source, an industrial robot is used for holding the sample under investigation and the detection system.

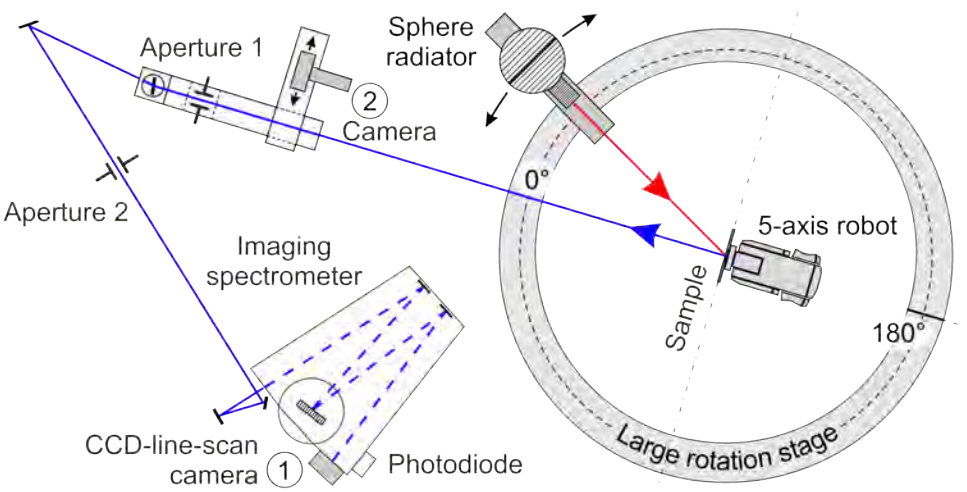

Figure 3.1: 3D Appearance Robot–based Gonioreflectometer with focusing optics: (1) is a line–scan camera module attached to the imaging spectrograph for measurements with respect to the spectral radiance factor $\beta(\lambda)$; (2) is a high–resolution video photometer system for measurements of the radiance

The basic optical layout of the ARGon^3 facility for the measurement of diffuse reflection properties of samples is the following. The unfiltered broadband radiation from a quartz halogen lamp is directed onto the sample under test. The detection system consists of the profiling optics (five mirrors and two apertures) and a half meter Czerny–Turner monochromator (CZ–monochromator) with two output slits: a photodiode can be mounted on the side exit slit, the front exit slit is equipped with a line–scan camera. In addition to the detection system, ARGon^3 has a high resolution video photometric camera which can be transferred by a transfer table to the optical path in the position before the profiling optics [31].

3.1 Light Sources of ARGon[3]

The main light source is a 400 W (11.2 A) quartz–halogen lamp placed in a water cooled spherical housing with an inner diameter of 150 mm (Fig. 3.2). The sphere itself is machined from two solid aluminium blocks on a computerized numerical control (CNC) turning lathe. The inner sphere surface is coated with pure $BaSO_4$ powder diluted in distilled water and sprayed to the inside with an air brush pistol. The thickness of the applied $BaSO_4$ layer is about 1 mm [32].

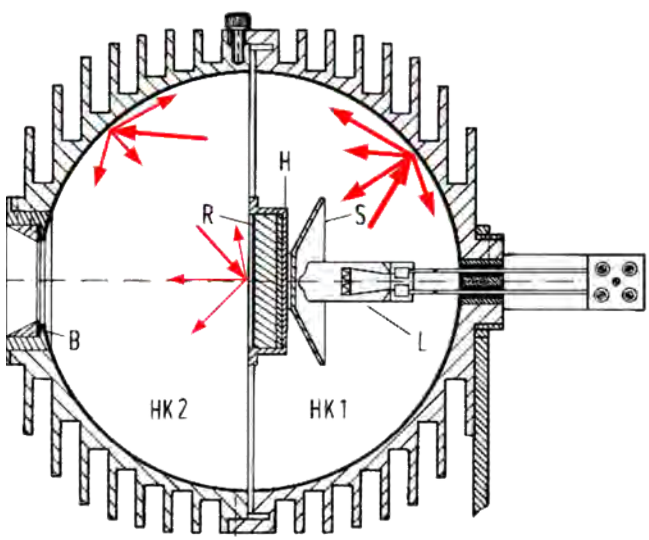

Figure 3.2: An illustration of the ARGon[3] sphere radiator [32]

The lamp (L) is placed in the first half sphere (HK1). At a distance of 1.94 mm from the equator plane of the sphere, a reflection baffle (R) is installed in a holder (H) [33]. The baffle is a flat aluminium plate coated with barium sulphate. The holder has a screen (S) which protects the exit port of the sphere from the direct irradiation by the lamp. The exit port is equipped with a precise aperture (B) with a 40.01 mm diameter.
The lamp radiation after reflection from the inner walls of the sphere reaches the reflection baffle in the equator plane of the sphere, at least the radiation emerges from the output aperture [32]. This arrangement insures a homogeneous output radiation. The radiance homogeneity of the emitted radiation, measured in the plane of the limiting aperture ($\varnothing = 40.001$ mm) at the output of the sphere radiator, is about 99.8 %, see Fig. 3.3 [33,34]. The distance from the limiting aperture at the output of the homogeneous sphere radiator to the sample is kept constant at 784.32 mm.

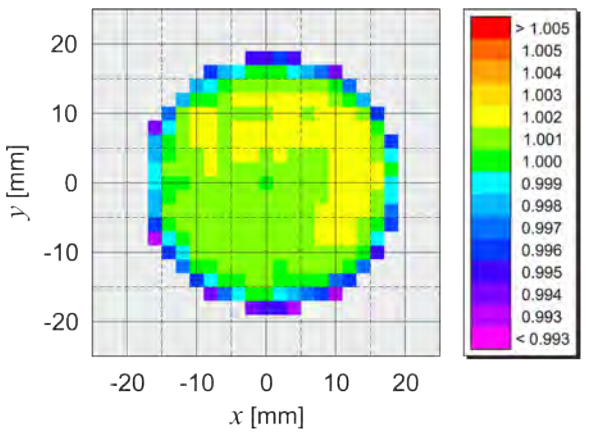

Figure 3.3: Two–dimensional homogeneity plot of the emitted radiance of the sphere radiator [32]

The second light source which can be mounted to the rotating stage is a home-made lamp composed from a 12 V, 50 W tungsten halogen lamp with a multifaceted pressed glass reflector attached to a special filter element producing a D65–like spectrum. The filter of the D65–like light source is a colour glass filter with an interference coating. This in combination with the tungsten halogen lamp represents approximatly the theoretically defined CIE illuminant D65 (colour temperature of about 6500 K) [34].

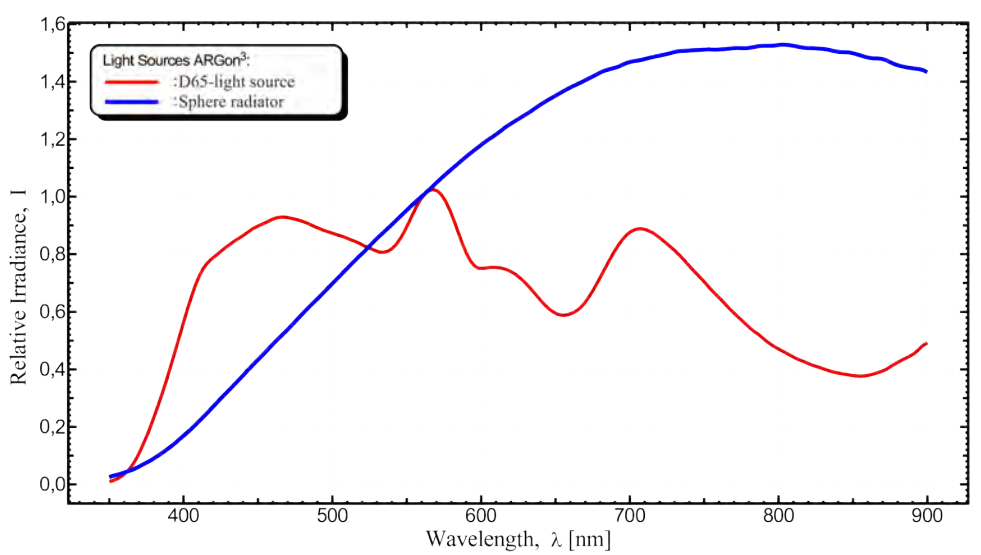

Figure 3.4: SPD of the sphere radiator (blue solid line), the D65–like light source (red solid line) of the ARGon^3 facility

In figure 3.4, the relative SPD of the sphere radiator and D65–like light source of the

ARGon^3 facility is depicted.

3.2 Sample Alignment: 5–Axis–Robot

In the center of the rotation stage, a five–axis industrial robot (Mitsubishi RV–2AJ [35] see Fig.3.5) with an acromial height of 550 mm is used as a holder of the sample under test. The robot can carry and position samples with an outer diameter of up to 500 mm and a maximum weight of up to 2 kg. The spatial position accuracy is 0.02 mm for arbitrary motions in 3D space. The rotation accuracy of the base axis of the robot is 0.002°. The flexibility of the robot system rather comes from the implemented three internal coordinate systems (world–, base– and tool–coordinate system) with the capability of direct coordinate transformations between them. Due to this, the programming of the motions, translations and rotations necessary for the 3D–alignment of the sample under test is relatively easy.

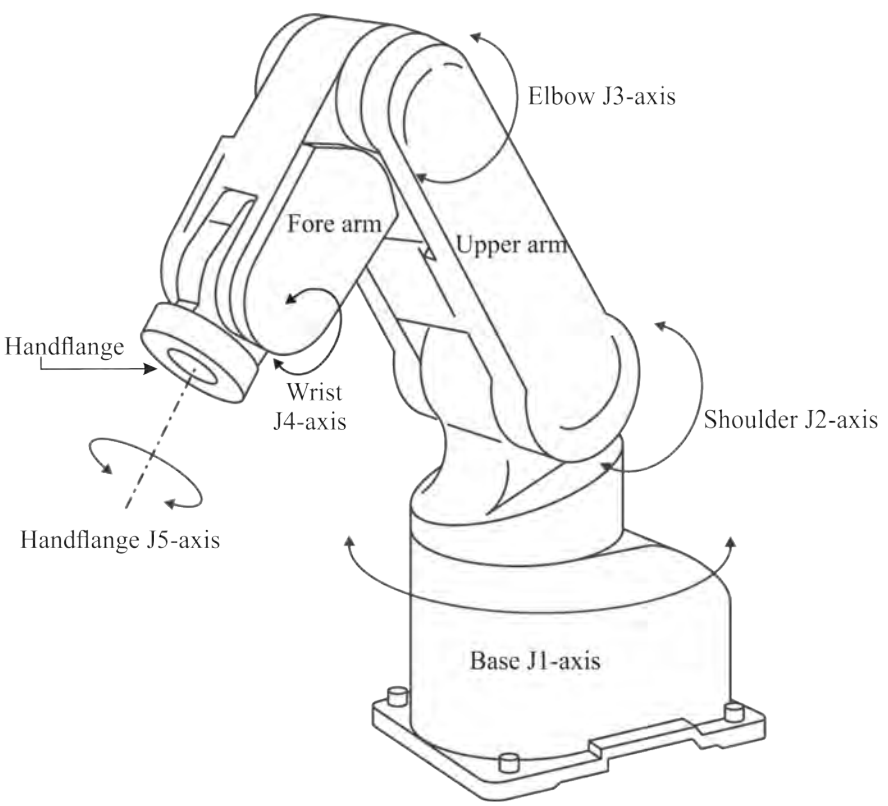

Figure 3.5: Sketch of the Mitsubishi RV–2AJ robot with the rotation axes

During the measurements the robot is operated with the hand flange above the basic platform collinear with the base axis of the system. This kind of operation is unusual for

an industrial robot. But it is the necessary position to ensure that the measured point within the surface of the sample is always located within the common rotation axis of the rotation stage and the base axis of the robot. This provides full angular control of the incident and reflected radiation within the full half space above the surface of the sample [36].

3.3 Rotation Stage

Both lamps are mounted to the rotation stage (Ø = 1300 mm) and can be turned by 360° around the robot with the sample under test. The angular range of the incident radiation is in the range from 0° to 360° (see Fig. 3.1), the light source orientation angle relative to the sample normal. The angular range of the reflected radiation is 0°–360° (see Fig. 3.5 – J1–axis of the Robot) for the sample azimuth angle and 0°–85° (see Fig. 3.5) – J5–axis of the Robot for the sample reflection angle. The minimum angle gap between incident and reflected beam is 7°; smaller angles are blocked by the light source. The definition of the incident and reflection angles connected to the sample normal are represented in Fig. 3.6. This spatial resolution gives the opportunity to realize almost any geometrical configuration of illuminating and observing the sample.

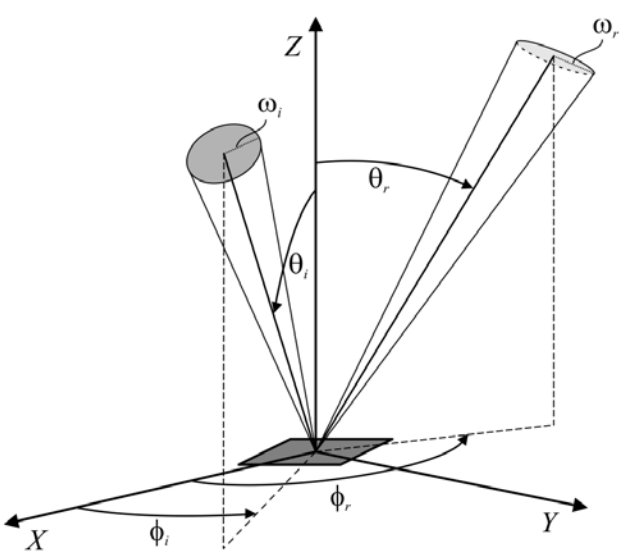

Figure 3.6: Incident and reflected beams of the gonioreflectometer within a spherical polar coordinate system

The combined adjustment of the rotation stage and the robot allows also measurement of so–called "out–of–plane" reflection, where the direction vectors of irradiation and ob-

servation and also the normal vector of the sample are not lying in a common plane (see Fig 3.6).
"Out–of–plane" geometries are currently gaining more and more interest for investigations of new so–called goniochromatic materials with strong angular dependent reflection behavior. Earlier, measurement geometries of commercial spectrophotometers were mostly limited to the standardized geometries of 45°:0° and 0°:45°. In real life the visual appearance of objects is strongly influenced by the observation conditions of the sample even for arbitrary unstandardized angles.

3.4 Detection System. Beam Profiling Optics

In the ARGon[3] system the beam is profiled by means of a mirror–based focusing optics from 20 mm on the sample surface to 2 mm on the entrance slit of the monochromator (Fig. 3.7). A circular area at the sample position (Sample) is imaged in five steps to position 8, which is the monochromator slit. The imaging system optics consists of three plane mirrors (number 2, 3 and 6) and two concave mirrors with radii of curvature of 1220 mm (mirror number 4) and 350 mm (mirror number 7).

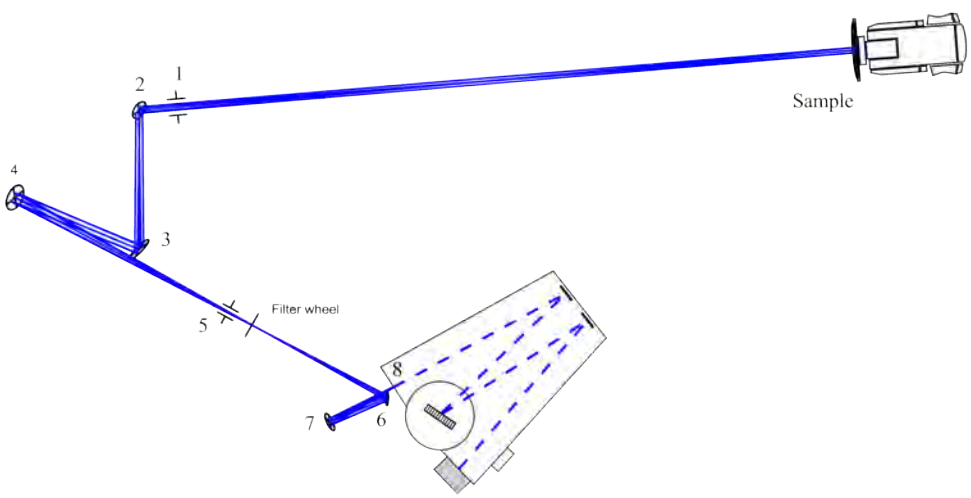

Figure 3.7: Schematic diagram of the focusing optics into the spectrometer

An aperture with a diameter of Ø = 18 mm is mounted at position 1. This aperture defines the opening detection angle with a half cone of 0.28°. The overall optical path length (the distance from Sample to point 8) of the imaging system is about 4.5 m. An intermediate image aperture (aperture 5) is defined by an aperture with the diameter of Ø = 5.6 mm. A Filter wheel is used for measurements with the CCD line–scan camera to provide the necessary dynamic range of signals, and is then mounted in the optical

path behind intermediate image aperture.

3.5 Monochromator

A half–meter Czerny–Turner monochromator (CZ–monochromator) JobinYvon iHR–550 [37] is used for the spectral selection of the reflected signal from the sample surface. The scheme of the CZ–monochromator is presented in Fig. 3.8.

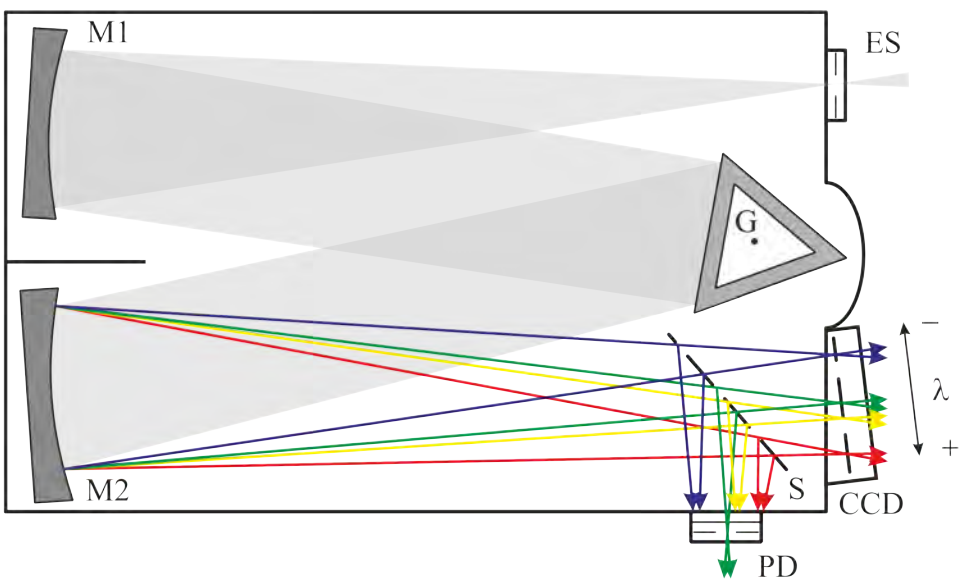

Figure 3.8: Schematic diagram of the CZ–monochromator

The CZ–monochromator has two concave mirrors and three diffraction gratings mounted on a triangular stage turret. The first mirror (M1) collimates the incoming light; the second mirror (M2) focuses the dispersed light from the grating plane (G). For the iHR–550 the output focal length is 568.72 mm; the deviation angle is 12.996°; the incline angle is 2.35°. The iHR–550 has two outputs slits: one at the front and one at the side. A swiveling mirror can direct the light beam to the side slit.The monochromator has three diffraction gratings, located on a rotation turret. The groove densities of the gratings are: 1200 l/mm (blazed at 330 nm) with a dispersion of 1.46 nm/mm; 950 l/mm (blazed at 900 nm) with a dispersion of 1.75 nm/mm and 150 l/mm (blazed at 550 nm) with a dispersion of 11.5 nm/mm. These diffraction gratings provide the required wavelength range from 350 nm to 1100 nm. The first and second grating are used for the measurements of the radiance factor in combination with a photodiode and a picoamperemeter. The efficiency of the gratings with the photodiode (Hamamatsu S1337–66BR [38]) and picoamperemeter (Keithley 6485 [39]) is shown in figure 3.9.

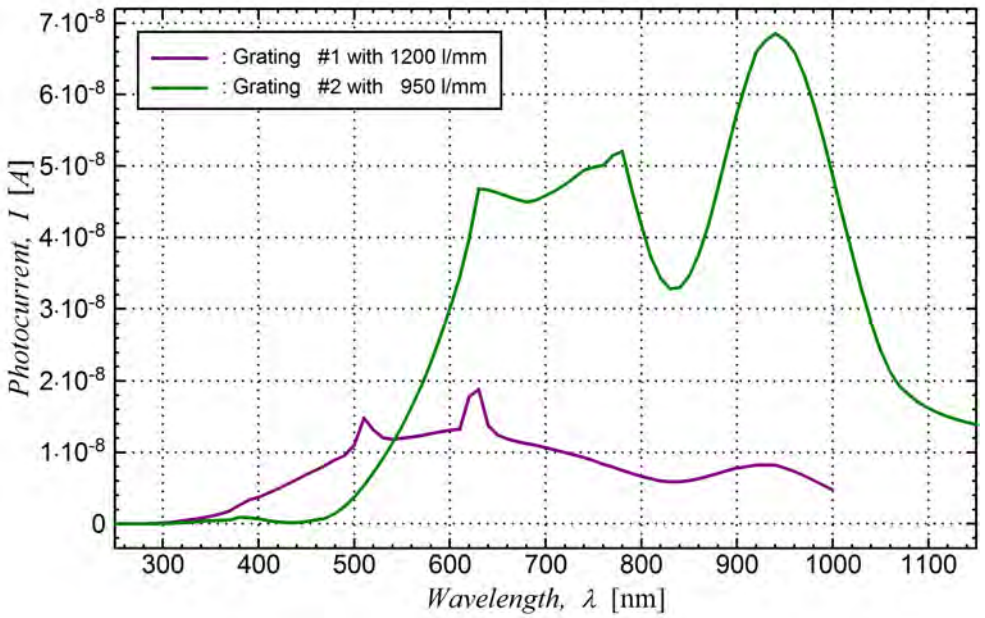

Figure 3.9: Signals from the 1st and 2nd grating

The spectral efficiency of detection in the wavelength range 350 nm — 540 nm with the first grating is almost 10% better than with the second one. In the wavelength range 540 nm — 1100 nm the use of the second grating for signal detection is rational.
The iHR–500 is equipped with a third diffraction grating used jointly with the CCD. The spectral efficiency of the 3rd grating CCD array is shown in figure 3.10 in a logarithmic scale.

3.6 CCD Line–Scan Camera

The CCD line–scan camera has a Full Frame Transfer (FFT) image sensor. The FFT–CCD consists of a vertical shift and a horizontal shift. The signal charge is generated in the semiconductor layer of the CCD when light comes through the transparent electrode into it. This charge signal accumulates into the potential electrode during the integration period, and then the charge is transferred to output section via the horizontal shift register for each frame during the closed period [10, 40]. By the way of the measuring, the packet size of minority charge in a CCD register. This CCD is a back–tuned type. Readout is realized in voltage mode with a floating gate preamplifier. Sufficient information about CCD detectors, their operation, types, field of application and the way of their characterization can be found in [40].
The CCD line–scan camera of ARGon^3 has 1036 Pixels with an effective pixel size of 24 μm × 24 μm (all image area 1036 × 122 Pixel), the dynamic range is 16 Bit (i.e.

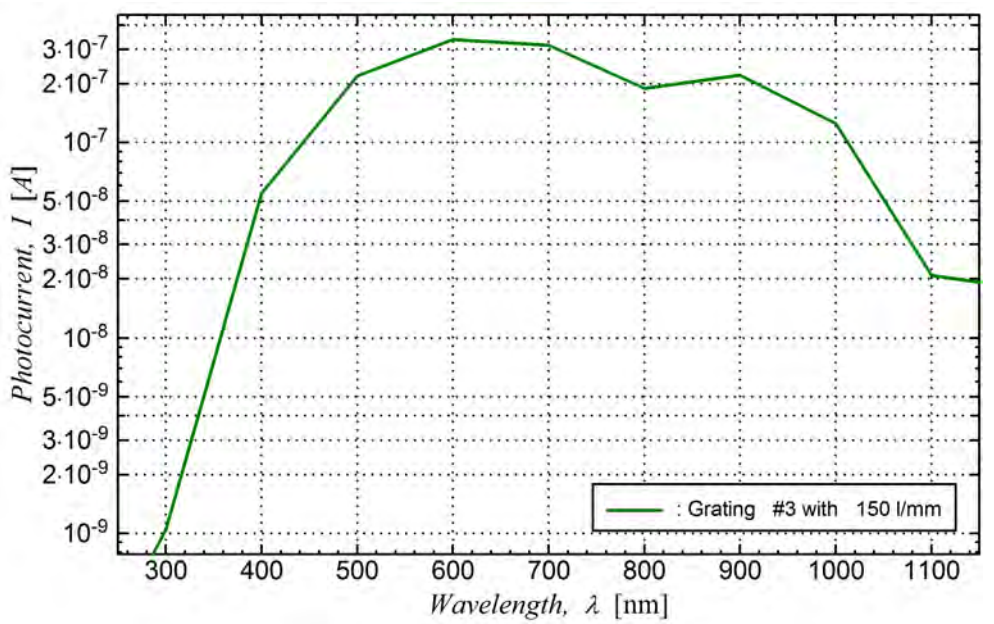

Figure 3.10: The efficiency of the 3rd grating in logarithmic scale

equivalent to $6.5536 \cdot 10^4$ assembly levels). A single–shot of the CCD in combination with the 3rd grating of the monochromator has a spectral coverage of 290 nm. That means for the full wavelength range from 380 nm to 850 nm it is necessary to adjust the diffraction grating on central wavelengths at 500 nm and at 700 nm.
The monochromator with the third diffraction grating and the CCD line–scan camera was specially wavelength calibrated for a central wavelength of 500 nm (i.e. the wavelength range for CCD array is 360 nm to 650 nm) against the spectral emission lines of Mercury and for a central wavelength of 700 nm (i.e. the the wavelength range from 560 nm to 850 nm for the CCD array) against the spectral emission lines of Krypton. The correspondence between pixel array and wavelengths was defined and calculated. The wavelength adjustments of the CCD–line scan camera with the monochromator was done. The results of these adjustments are presented in **Appendix A**.
The maximal wavelength deviation measured at ARGon[3] for the wavelength range 350 nm to 850 nm is 0.82 nm. This was expected from the calculation of the estimated multichannel resolution for iHR–550 in CCD–configuration.

3.6.1 Linearity of the CCD Line–scan Camera

During the measurement process the incident photons on each pixel are converted to electron–hole pairs. This is the conversion of the photonic input to electronic output. When an exposure is over, the electrons are captured under the gate electrons and are

transferred to the output amplifier, where the charge will be modified to the output electrical signal. The controller converts the electron charge in a binned group of pixels to digital counts (analog–to–digital units (ADU)). The transfer function of the CCD between the incident radiation signal and the digitized output is rather linear to the amount of incident light. Linearity is a measure of the deviation from the following equation

$$DS = Const. \cdot I_{light}$$

where DS is the digital signal, Const. is the conversion from electrons ADU constant and I_{light} is the amount of incident light on the CCD. The conversion electrons/ADU is constant for our CCD.

The CCD is not a perfectly linear system. The numbers of ADU counts are not precisely proportional to the number of incident photons. There are three methods of investigation for the linearity of a CCD:

1. The linearity of a detector array is possible to verify by varying of the distance between the light source and detector according to the illuminance inverse–square law described dy the equation (1.10).

2. By using neutral density filters with known spectral transmittance coefficients, it is possible to reduce the signal intensity and to check the linearity of the detector array.

3. The method of plotting the signal value versus the exposure time can also be used for verifying the linearity of the CCD. The deviation of each point from a least–squares regression of the measured data of the signal is applied.

By reason of the fixed distance between the light source and the CCD detector in ARGon[3] facility for verification of the detector array linearity was used the second and third described above methods.
A set of neutral density filters (ND filters) with known spectral transmittance was exploited for the attenuation of the light source signal and the definition of the linearity of CCD array. The graphics in figure 3.11 represent the signal versus the attenuation factor of the filter at the central wavelengths of 500 nm and 700 nm. Filters with nominal optical densities of 0.6, 0.9, 1.5, 2.5, and 3 were chosen for the linearity investigation. The exposure time in the experiment was set to 30 ms. In this way, the saturation of the pixels at 100 % of full capacity of the CCD array ($2 \cdot 10^{16}$) can be avoided. The transmission of the filters at wavelengths of 500 nm and 700 nm was measured with a spectrophotometer Cary 5000 UV. The real attenuation factor of every filter is depicted

on the abscissa axe. The measured light signal is plotted on the ordinate axe and the linearity of CCD array was calculated.

a

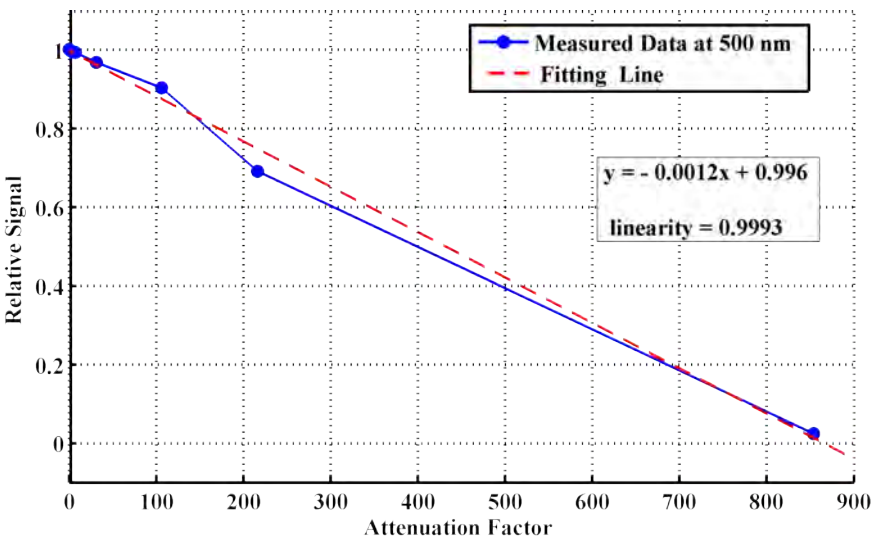

b

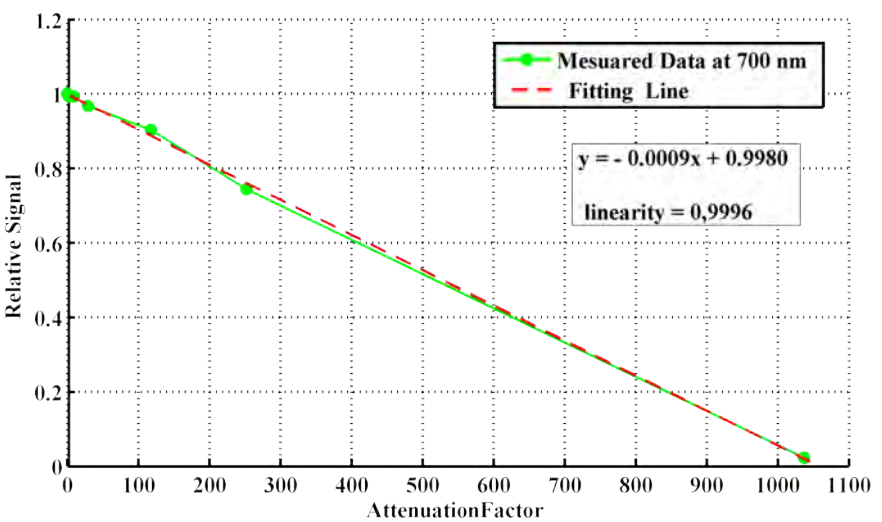

Figure 3.11: The linearity deviation of the Hamamatsu CCD at 500 nm (a) and at 700 nm (b)

The linearity of the CCD array is 99.9% at both selected wavelengths (500 nm and 700 nm).
In figure 3.12, the supplemental linearity of the CCD array is depicted, which was defined

by the method of changing the exposure time and detecting the signal from the light source (third method mentioned above).

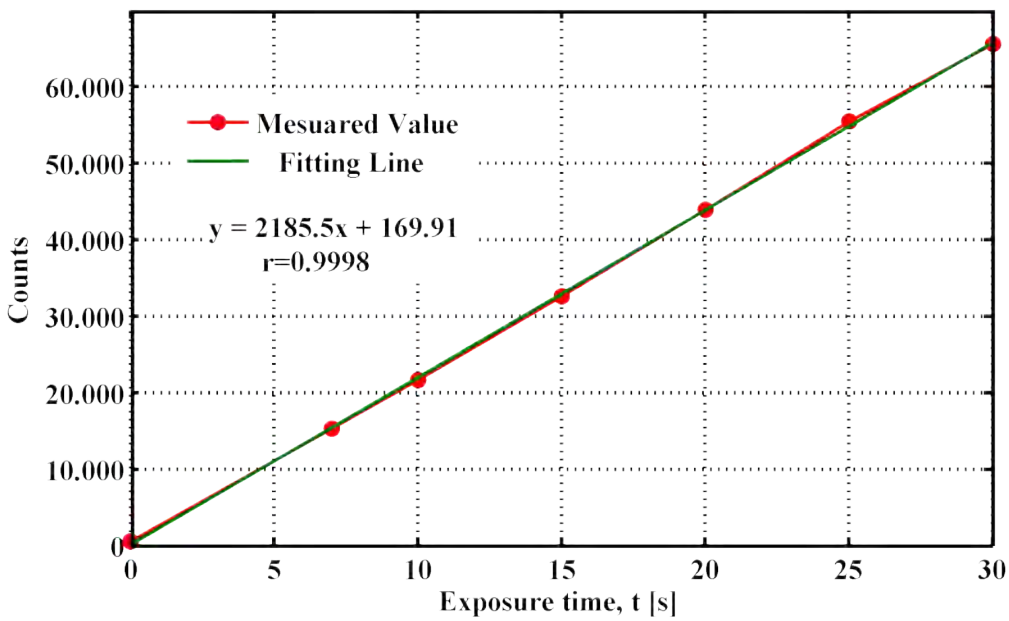

Figure 3.12: The linearity of Hamamatsu CCD defined by the method of exposure time varying

Even for the shoterst possible exposure time of 0.7 ms, the CCD array is saturated, when one directly expose it to the ARGon^3 facility sphere radiator.Therafore, it was decided to attenuate the sphere radiator light signal with the ND filter and the exposure time was kept constant (the signal from the sphere light source of ARGon^3 facility is usually higher the sample's reflection signal by 10^3). Therefore, the method of plotting the signal value versus the exposure time matches the method of absolute spectral radiance factor measurements better than the method of using neutral density filters with known spectral transmittance coefficients in order to reduce the signal intensity.

3.7 High–Resolution Video Photometer System

The photometric camera LMK 5 color is a commercial combined imaging luminance measurement device and imaging colour measurement device (relative ILMD/ICMD), produced by the TechnoTeam company. This camera system has an implemented CCD–sensor containing 1364 $\times$ 1030 Pixels.

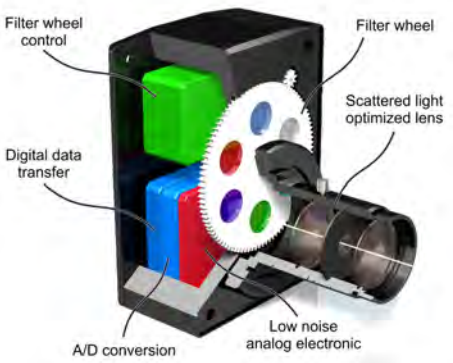

Figure 3.13: The photometric camera and its main components [41]

The lens based imaging system of the luminance camera with a focal length of 210 mm is used to achieve high resolution images. In our setup, we obtain a resolution of approximately 28 $\mu m \times 28\ \mu m$ on the sample. The field of view of the objective lens is 28 $mm \times 38\ mm$ (equivalent to an angular range of $1.15° \times 1.55°$). A schematic sketch of the main components of the camera system is presented in the figure 3.13.

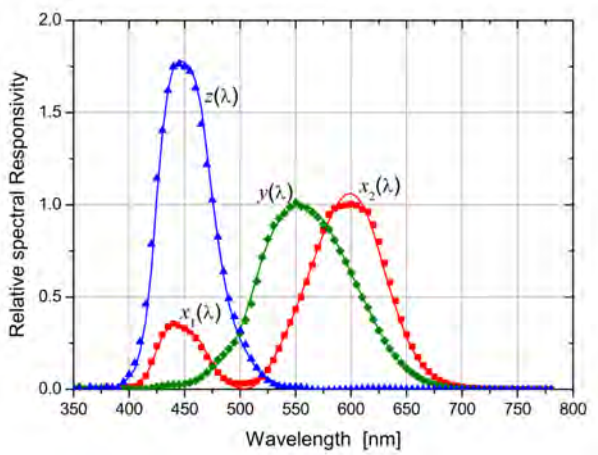

Figure 3.14: CMFs of the LMK–5 Color camera system for the CIE 2° standard observer. The spectral matching of the camera's filters is depicted by the defined values by the points lines and the theoretical values by the solid lines [41]

This photometric camera has high dynamic range (HDR) capability, enabling measurements with a dynamic range with a ratio of up to $1 : 10^7$ ($\sim 140\,dB$). The ILMD/ICMD–system is adapted to the colour matching functions of the 2° standard CIE observer (CIE 1931) through a build–in filter wheel. With the high–resolution video photometer system luminance as well as tristimulus values can be determined. This permits the imaging measurement of chromaticity coordinates, which can be given in different colour spaces. The

filter wheel has 6 optical filters, 4 filters are required for the colour matching functions simulation, (two filters for the $x(\lambda)$, $y(\lambda)$ and $z(\lambda)$) CMF simulation) see Fig. 3.14. The fifth filter is applied to simulate the photopic luminous curve of human eye $V(\lambda)$, the additional filter provide the scotopic luminance curve $V'(\lambda)$.
The photometric camera is capable to measure spatially resolved luminance distributions $L(x, y)$ with a resolution on the sample under test of approx 28 μm (Fig.3.15). The figure 3.15 shows a high resolution luminance picture in false colour presentation of an effect pigmented measured in 15°:0° "in–plane" geometry. The effect pigment is applied on two backgrounds (black and white). The lower luminance values belong to the black background. The needle–like structure, which is called ("sparkling"), ensues from semi-transparent or transparent layers applied onto metal oxide–coated aluminium or mica. The CIELAB colour coordinates can also be determined with the spatial resolution of the imaging system (28 μm) [36].

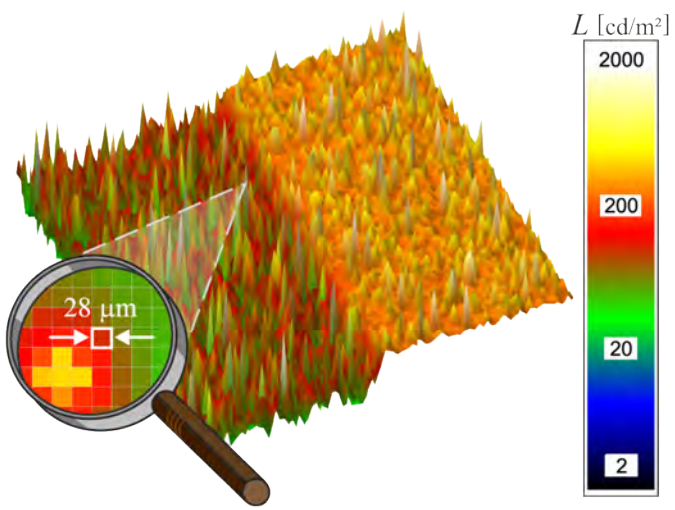

Figure 3.15: Spatially high resolved luminance distribution of an effect pigment (Xirona® Volcanic Sparks) applied on two backgrounds (black — left side and white — right side)

4 RADIANCE FACTOR $\beta(\lambda)$ AND METHOD OF ITS MEASUREMENT

4.1 Reflection Standards

Surfaces are often described by the response of the material to irradiation. The common approach is the measurement of the ratio of the light that is reflected to the incident light. This method describes a material by its reflectance ρ. A quantity associated with diffuse reflection is the spectral radiance factor $\beta(\lambda)$. A quite similar definition is the bidirectional reflectance distribution function (BRDF) $f_r(\lambda)$, except that it is defined only for directional incident light. The BRDF of a surface is a function that specifies for the incident radiation the angular reflection distribution. The spectral radiance factor $\beta(\lambda)$ is the quotient of the radiance $L(\theta_i, \phi_i, \theta_r, \phi_r, \lambda)$ reflected by the sample surface to the radiance reflected by the PRD L_r^{PRD} in the same conditions of irradiation and observation:

$$\beta(\lambda) = \frac{L_r(\theta_i, \phi_i, \theta_r, \phi_r, \lambda)}{L_r^{PRD}} \tag{4.1}$$

where θ_i is the polar incident angle, ϕ_i is the azimuth incident angle, θ_r is the polar reflection angle, ϕ_r is the azimuth reflection angle and λ is the wavelength.

The radiance coefficient $q(\theta_i, \phi_i, \theta_r, \phi_r)$ is preferred to the spectral radiance factor [42]. It is defined as the ratio of the reflected radiance $L(\theta_i, \phi_i, \theta_r, \phi_r, \lambda)$ to the incident irradiance $E(\theta_i, \phi_i, \theta_r, \phi_r, \lambda)$:

$$q = \frac{L(\theta_i, \phi_i, \theta_r, \phi_r, \lambda)}{E(\theta_i, \phi_i, \theta_r, \phi_r, \lambda)} \tag{4.2}$$

The incident irradiance is not measured directly, but it can be calculated from radiance of PRD [43]

$$L_r^{PRD} = \frac{E_i}{\pi} \tag{4.3}$$

For calculating the radiance factor by the absolute method, form previous equations (4.2) and (4.3) the following relation have to be notice

$$q(\theta_i, \phi_i, \theta_r, \phi_r, \lambda) = \frac{\beta(\theta_i, \phi_i, \theta_r, \phi_r, \lambda)}{\pi} \tag{4.4}$$

The BRDF is a function of evolution of the radiance coefficient with respect to the directions of irradiation and reflection of the surface. The BRDF and radiance factor are used for the description of diffuse reflection from a surface relative to the PRD, which reflects, by definition, the incoming radiation loss–free, completely diffuse and with a Lambertian direction characteristics (see section 1.2). The PRD is a theoretical concept only and cannot be realized materially, since there is no material with these characteristics. The measuring apparatus itself, in the context of an absolute measurement, carries out the realization. So, by definition the radiance factor and BRDF cannot be measured directly. However, absolute measurements are a laborious process and demand an amount of time. The relative measurements of the spectral radiance factor in industry are predominantly based on reflection standards. The reflection standards must be traceable to the absolute scale of a National Metrological Institute (NMI). For the reflection standards different kinds of materials are used (Fig. 4.1).

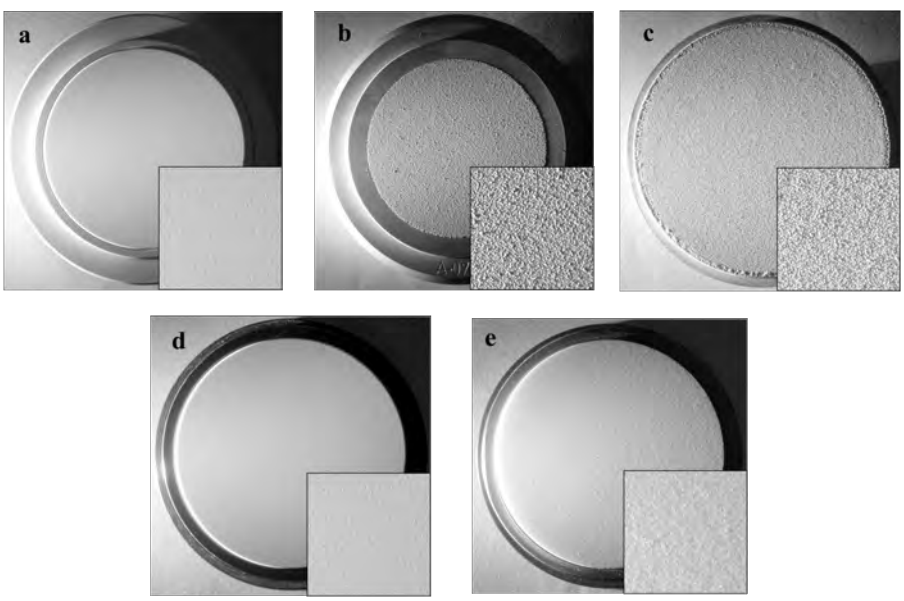

Figure 4.1: Standard reflection materials: a. — Opal Glass; b. — Pressed Barium Sulphate; c. — Primed Barium Sulphate; d. — Ceramics; e. — sintered Polytetrafluoroethylene (PTFE)

Reflection standards can be produced from white crystalline $BaSO_4$ powder. The white standards were manufactured from pressed $BaSO_4$ using a special powder press against a matted glass plate. As a result, the structure of the glass plate is molded into the powder. This kind of reflection standard is very delicate. That makes it is hard for carriage. Due to this fact, a so–called primed barium sulphate standard was developed at PTB. It has an internal grid structure made of stainless steel and the first one–third of the $BaSO_4$ is

loaded with a bonding mixture of polyvinyl alcohol as a binder. The remaining layers are made from a suspension of barium sulphate diluted in distilled water [44].
Opal glasses are used as diffuse reflection standards since the forties of the last century (so–called Vitrolite white opal glasses). The disadvantage of opal glasses is the relatively high translucency. For this reason, they were replaced by Russian opals and later by the opal glasses developed by the European Commission. A great advantage of the European Commission opal glasses is the presence of two useable surfaces—one side is glossy, the other side is matt. It is possible to choose the desired surface structure preferred by certain conditions of measurements. These opal glasses are wide–spread within Europe as a reflection standard. Due to the good purity and long–term stability.

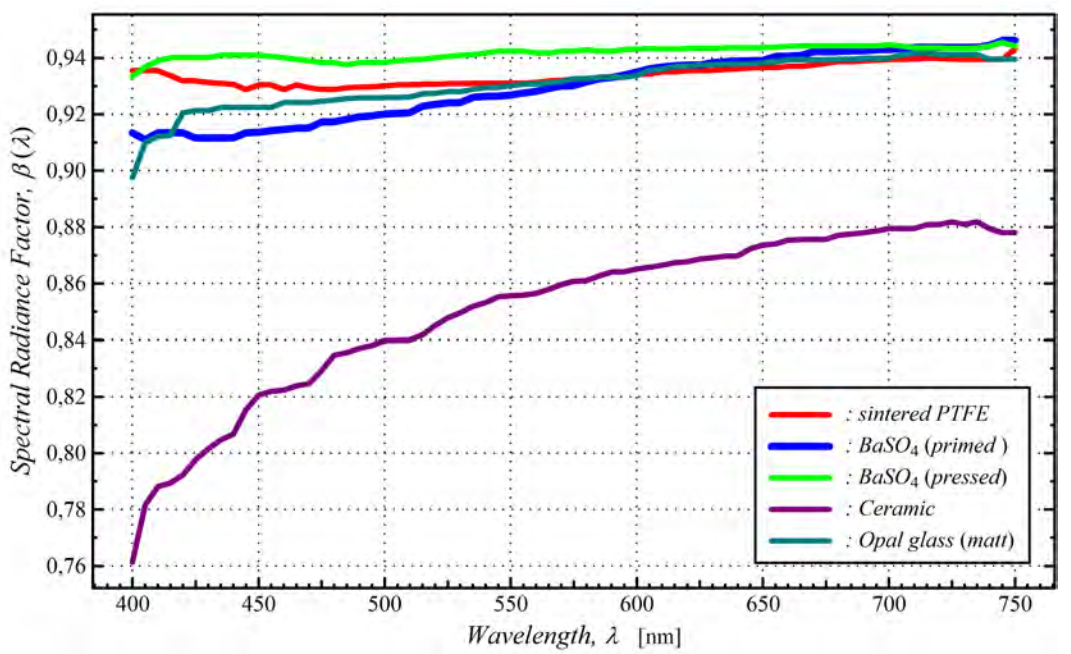

Figure 4.2: Typical Spectral radiance factor curves of different diffuse reflection standards in 45°:0° measurement geometry

Ceramic reflection standards were also developed with the intention to have a set of permanent. Uniform standards. Ceramics are inherently very robust and time–stable materials. They also could be produced with glossy and matted surface finishes. Moreover, ceramic reflection standards are easy to clean and they are available in a wide colour range. The disadvantage is their maximum reflection value of about 0.9, even for white ceramics standards. Ceramics also as opal glasses are inconvenient to use in the ultraviolet range of the light spectrum (UV–range).
There are sintered polytetrafluoroethylene (PTFE) like Spectralon and identical materials used in reflectometry as reflection standards. Sintered PTFE standards have reflection

values generally of about 0.95 in the range 250 nm to 2500 nm and values of about 0.99 in the specific range between 400 nm to 1500 nm [45]. For diffuse reflection measurement sintered PTFE standards are well–established reference materials. Moreover, they has quite good Lambertian scattering properties. The main advantage is its quite high reflectance even in the UV–range. The weak side of these standards is the degradation of the material — caused by volatile hydrocarbon impurities in the resin during the manufacturing. A second drawback is its impetuous dust contamination caused by electrostatic charging. Typical spectral radiance factor curves of reflection standards are depicted in Figure 4.2.

4.2 Method of Goniometric Measurements of the Spectral Radiance Factor $\beta(\lambda)$

The spectral radiance factor $\beta(\lambda)$ of a surface element of a non–self–radiating object, in a given direction, under specified conditions of irradiation, is the ratio of the radiance of that surface element in the given direction and the PRD which is identically irradiated [7]. By this definition, the radiance factor is valid as well for directional/directional geometries as well as for hemispherical/directional geometries (see equation(4.1)). The incident radiation is denoted with the index i and the reflected radiation with the index r. The wavelength dependence is considered by the parameter λ.
The PRD is just a theoretical concept. In order to make an absolute measurement of the spectral radiance factor, it is required to calculate the radiance of the PRD. A hemisphere with uniform radiance is able to simulate PRD as shown in [32,33]. As it was mentioned in section 3.1, the sphere light source was constructed to secure the creation of the PRD by the multiple reflections of the light from the inner walls of the sphere and the baffle. The PRD has the next peculiarities [46]:

1. For a Lambertian surface, reflectance ρ and spectral radiance factor $\beta(\lambda)$ are identical.

2. Reflectance ρ from a surface ranges between 0 and 1. The reflectance ρ and spectral radiance factor $\beta(\lambda)$ can describe the diffuse reflectance of the surface [23].

3. The spectral radiance factor $\beta(\lambda)$ is closely related to the bidirectional reflectance distribution function $f_r(\lambda)$, as the BRDF is defined in the next manner: the derivation of the radiance of a surface in the given direction to the irradiance on the medium
$$f_r(\lambda) = \frac{dL}{dE} \tag{4.5}$$

The radiance of the PRD is proportional to the irradiance of the medium.

$$L_i(\lambda) = \frac{E_i(\theta_i, \phi_i, \lambda) \cdot R^2}{A \cdot cos(\theta_i)} \tag{4.6}$$

where R is the distance between the radiator and surface, $A \cdot cos(\theta_i)$ is the projected solid angle Ω_i weighted by the cosine of the polar incident angle (θ_i) with the surface normal, A is the area of the radiator and L_i is the radiance of the radiator.

According to equations (4.1) and (4.6), the radiance factor of any reflected surface can be computed as

$$\beta(\lambda) = \frac{R^2 \cdot \pi}{cos(\theta_i) \cdot A} \cdot \frac{L_r(\theta_r, \phi_r, \theta_i, \phi_i, \lambda)}{L_i(\lambda)} \tag{4.7}$$

where the ratio $G = \frac{R^2 \cdot \pi}{cos(\theta_i) \cdot A}$ is the geometrical extent. The geometrical extend is constant for the defined geometrical condition of illumination/observation.

4.3 Uncertainty of Spectral Radiance Factor Measurements with ARGon^3. Scale Comparison

4.3.1 Uncertainty for the configuration photodiode–picoamperemeter

Absolute measurements of the spectral radiance factor of different reflection materials by ARGon^3 for the configuration with a photodiode were done. The results of the measurements were reported and the uncertainty of measurements was estimated according to [47–50].
The mathematic model of the spectral radiance factor uncertainty measurement for geometrical configuration $45° : 0°$ according to equation (4.7) is

$$\beta(\lambda) = \frac{R^2 \cdot \pi}{cos(\theta_i) \cdot A} \cdot \frac{(S_{HR} - S_{DR})}{(S_{HI} - S_{DI})} \cdot (1 + L_S) \tag{4.8}$$

where R is the distance between the radiator and surface, θ_i is the polar incident angle, A is the area of the opening apperture of the irradiating lamp, S_{HR} is the reflection signal, S_{DR} is the reflection dark signal, S_{HI} is the incident signal, S_{DI} is the incident dark signal and L_S is the linearity of the picoamperemeter.

The uncertainty budget is presented for a single measurement of a diffuse reflection standard made of primed barium sulphate ($BaSO_4$) (BS 85–15) and shown in Table 4.1. [47, 51].

Table 4.1: Uncertainty budget of ARGon^3 photodiode–picoamperemeter configuration for measurement of spectral radiance factor at 500 nm

Input parameters X_i	Estimated value x_i	Distribution type (prefactor a_i)	Standard uncertainty $u(x_i)$	Relative sensitivity coefficient $c_i = \frac{1}{\beta} \cdot \frac{\partial \beta}{\partial x_i}$	Relative uncertainty contribution $\frac{u_i(y)}{y_i} = a_i \cdot \lvert c_i \rvert \cdot \cdot u(x_i)$
Reflection signal, S_{HR}	$3.61 \cdot 10^{-12}$ A	A normal (1)	$4.72 \cdot 10^{-15}$ A	$2.77 \cdot 10^{11}$	$1.31 \cdot 10^{-3}$
Reflection dark signal, S_{DR}	$5.40 \cdot 10^{-15}$ A	A normal (1)	$1.05 \cdot 10^{-14}$ A	$-2.77 \cdot 10^{11}$	$2.91 \cdot 10^{-3}$
Incident signal, S_{HI}	$7.95 \cdot 10^{-9}$ A	A normal (1)	$3.60 \cdot 10^{-13}$ A	$1.26 \cdot 10^{8}$	$4.53 \cdot 10^{-5}$
Incident dark signal, S_{DI}	$-1.31 \cdot 10^{-14}$ A	A normal (1)	$7.36 \cdot 10^{-14}$ A	$-1.26 \cdot 10^{8}$	$9.26 \cdot 10^{-6}$
Distance from the sample to the irradiating aperture, R	784.32 mm	A normal (1)	0.15 mm	$2.55 \cdot 10^{-3}$	$3.82 \cdot 10^{-4}$
Temperature of aperture, T	44.7 °C	B rectangular ($\frac{1}{\sqrt{3}}$)	5 °C	$3.10 \cdot 10^{-5}$	$8.95 \cdot 10^{-5}$
Area of the stop aperture, A	1257.35 mm^2	B rectangular ($\frac{1}{\sqrt{3}}$)	0.0175 mm^2	$-7.95 \cdot 10^{-4}$	$8.03 \cdot 10^{-6}$
Wavelength, λ	500.0 nm	B rectangular ($\frac{1}{\sqrt{3}}$)	0.2 nm	$3.21 \cdot 10^{-5}$	$3.72 \cdot 10^{-5}$
Linearity of the picoamperemeter, L_S	$-106 \cdot 10^{-6}$	B rectangular ($\frac{1}{\sqrt{3}}$)	$3.44 \cdot 10^{-4}$	1.0001	$1.99 \cdot 10^{-4}$
Angle of incidence, θ_i	45°	B rectangular ($\frac{1}{\sqrt{3}}$)	$4.71 \cdot 10^{-5}$ rad	-1	$2.72 \cdot 10^{-5}$

continued on next page

Table 4.1 – continued from previous page

Input parameters X_i	Estimated value x_i	Distribution type (prefactor a_i)	Standard uncertainty $u(x_i)$	Relative sensitivity coefficient $c_i = \frac{1}{\beta} \cdot \frac{\partial \beta}{\partial x_i}$	Relative uncertainty contribution $\frac{u_i(y)}{y_i} = a_i \cdot \lvert c_i \rvert \cdot \cdot u(x_i)$
Angle of reflection, θ_r	0°	B rectangular $(\frac{1}{\sqrt{3}})$	$35 \cdot 10^{-6}$ rad	$-1.78 \cdot 10^{-3}$	$3.60 \cdot 10^{-8}$
Uncertainty of measurements					$3.22 \cdot 10^{-3}$
Expanded uncertainty of measurements with the coverage factor $k = 2$					0.64 %

All uncertainty components were computed according to [47, 49].

The first four uncertainty components are of type A. They were computed as a relative standard deviation of the mean of the number of independent measurements of the input parameters (light and dark signal). The light and dark signals of the sample and light source are measured with a photodiode connected to a picoamperemeter. Photo currents of the light and dark signals are directly measured and the mean values of the signals are calculated for 10 independent measurements of every signal getting the specified standard deviation.

The next uncertainty component is the distance from the sample to the aperture of the irradiating lamp. Four series of measurements of the distance was done on the up, down, left and right sides relative to the entrance aperture of the spherical light source. In every series ten independent measurements were realized with an inside micrometer device, for precise determination of the distance from the sample plane to the entrance aperture of the sphere light source. The experimental standard deviation of the mean value of the series was calculated.

The uncertainty of the geometrical constant (the uncertainty of the illumination and observation angles) includes the uncertainty of the alignment and precision of the holding sample robot, rotation stage, carrying the light source, optical axis and stop aperture area. All of the components are computed as Type B, i.e. the uncertainty values are taken from calibration certificates. The uncertainty of the lamp aperture area comes from a calibration certificate [52, 53]. The geometrical constant depends on the geometrical conditions of illumination/observation, the uncertainty components were computed for the geometrical configuration at 45° incident light and reflection light at 0°.

The uncertainty of the detector linearity comes from an internal PTB calibration at working group 4.13 “Laserradiometry".

The uncertainty of the wavelength scale of the monochromator has been achieved by the calibration against mercury emission lines [54].

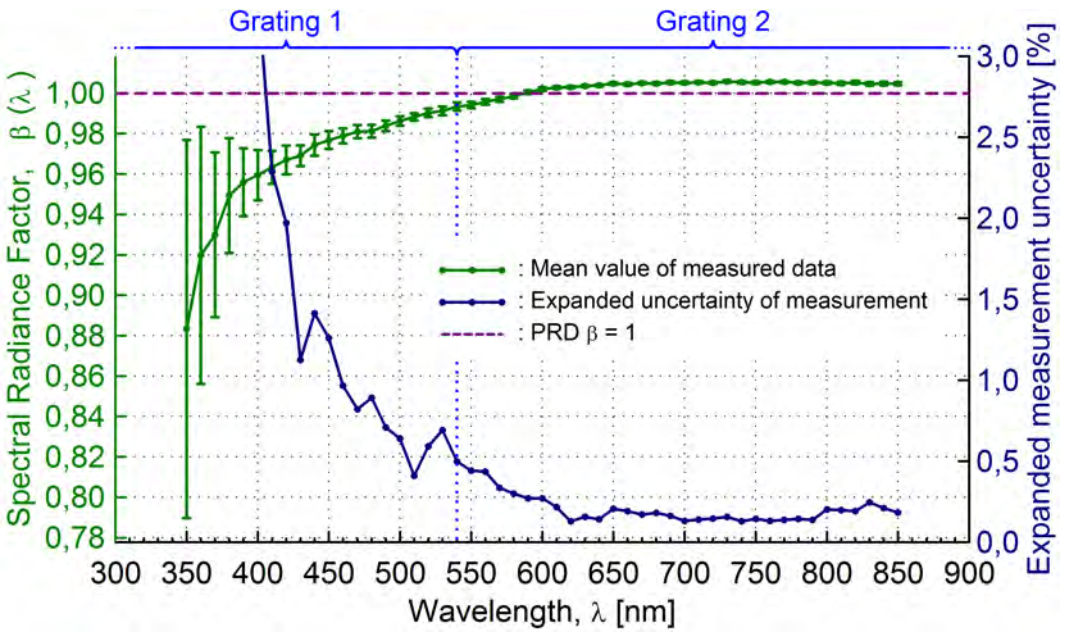

Figure 4.3: ARGon^3 in combination with photodiode–picoamperemeter measurements of the spectral radiance factor of the primed barium sulphate (BS 85–15) for the wavelength range from 380 nm to 1100 nm with measurement uncertainty

The uncertainty of each component of the spectral radiance factor has been computed according to [47]. In figure 4.3 the 7–times measured spectral radiance factor of primed barium sulphate in $V(\lambda)$–range for the 45°:0° measuring geometry is depicted by the dark–green solid line with corresponding error bars. The violet dashed line in the figure 4.3 is the spectral radiance factor of the PRD. The calculated expanded uncertainty of the 7–times measured spectral radiance factor of primed $BaSO_4$ is depicted by the dark–blue solid line. The vertical pointed blue line is the point of the switching of the monochromator gratings. The 1st grating is used in the wavelength range from 350 nm to 540 nm, the second one is applied for the measurement in the wavelength range from 540 nm to 850 nm.

The scale of the spectral radiance factor in $V(\lambda)$–range in the geometrical configuration 45°:0° has been compared with the PTB Gonioreflectometer which is used for customer calibrations (Fig. 4.4). The green solid line represents the spectral radiance factor of primed $BaSO_4$ measured with PTB Gonioreflectometer and the blue solid line is the spectral radiance factor of $BaSO_4$ measured with ARGon^3 with photodiode–picoamperemeter configuration. The blue dashed line in figure 4.4 presents the relative deviation of data measured with ARGon^3 in photodiode–picoamperemeter configuration to the spectral data measured with the PTB Gonioreflectometer. The dark–red line is the combined uncertainty of both facilities in 45°:0° geometrical configuration. The reason of the ob-

served offset in the wavelength range from 380 nm to 550 nm could be the quite low efficiency of the gratings of the ARGon^3 monochromator, which results in a very low signal from the observed sample.

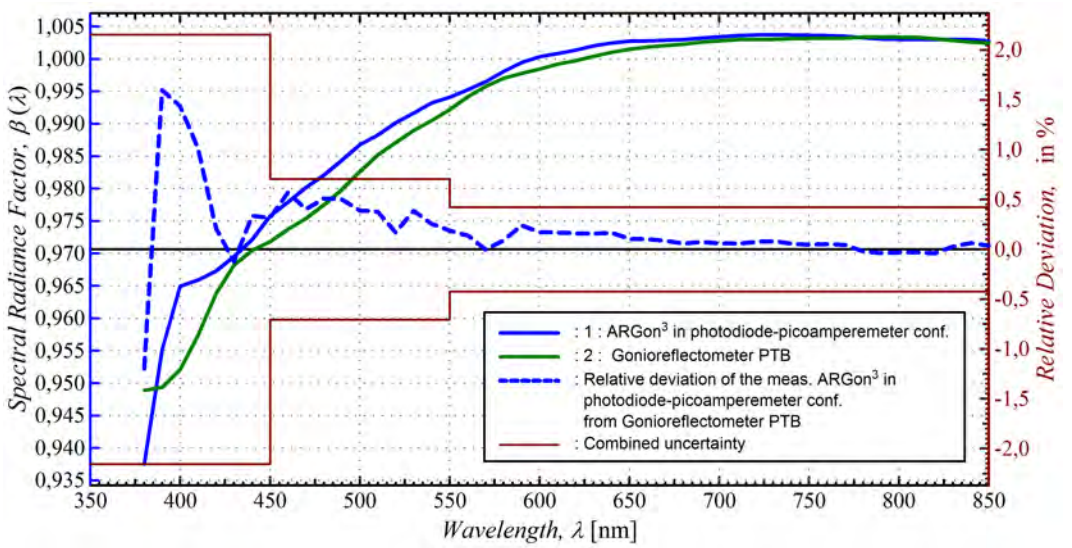

Figure 4.4: Comparison of the spectral radiance factor measurements with ARGon^3 in photodiode–picoamperemeter configuration and the Gonioreflectometer of PTB

4.3.2 Uncertainty for ARGon^3 in CCD–configuration

The uncertainty budget for ARGon^3 in CCD–configuration is presented in the Table 4.2. The measurement uncertainty was estimated according to [47–50].
The fifth to the eight component the uncertainty budget of ARGon^3 in CCD–configuration is identical to the components in Table 4.1. The mathematic model describing the spectral radiance factor measurement uncertainty for geometrical configuration 45°:0° according to equation (4.6) is

$$\beta(\lambda) = \frac{R^2 \cdot \pi}{cos(\theta_i) \cdot A} \cdot \frac{(S_{HR} - S_{DR}) \cdot T_f}{(S_{HI} - S_{HI})} \cdot (1 + L_s) \cdot (1 + SL) \tag{4.9}$$

where L_s is the linearity of the CCD array, SL is the stray–light contribution.

Table 4.2: Uncertainty budget of ARGon^3 in CCD–configuration for measurement of spectral radiance factor at 500 nm

Input parameters X_i	Estimated value x_i	Distribution type (prefactor a_i)	Standard uncertainty $u(x_i)$	Relative sensitivity coefficient $c_i = \frac{1}{\beta} \cdot \frac{\partial \beta}{\partial x_i}$	Relative uncertainty contribution $\frac{u_i(y)}{y_i} = a_i \cdot \lvert c_i \rvert \cdot \cdot u(x_i)$
Reflection signal, S_{HR}	13100 counts	B Rectangular ($\frac{1}{\sqrt{3}}$)	123 counts	$8.10 \cdot 10^{-5}$	$5.75 \cdot 10^{-3}$
Reflection dark signal, S_{DR}	750 counts	B Rectangular ($\frac{1}{\sqrt{3}}$)	7 counts	$-8.10 \cdot 10^{-5}$	$3.27 \cdot 10^{-4}$
Incident signal, S_{HI}	36300 counts	B Rectangular ($\frac{1}{\sqrt{3}}$)	221 counts	$2.81 \cdot 10^{-5}$	$3.59 \cdot 10^{-3}$
Incident dark signal, S_{DI}	750 counts	B Rectangular ($\frac{1}{\sqrt{3}}$)	7 counts	$-2.81 \cdot 10^{-5}$	$1.13 \cdot 10^{-4}$
Distance from the sample to the lamp, R	$784.32\,mm$	A Normal (1)	$0.15\,mm$	$2.55 \cdot 10^{-3}$	$3.82 \cdot 10^{-4}$
Area of the irradiating aperture, A	$1257.35\,mm^2$	B Rectangular ($\frac{1}{\sqrt{3}}$)	$0.0175\,mm^2$	$-7.95 \cdot 10^{-4}$	$8.03 \cdot 10^{-6}$
Temperature of aperture, T	44.8 °C	B Rectangular ($\frac{1}{\sqrt{3}}$)	5 °C	$3.10 \cdot 10^{-5}$	$8.95 \cdot 10^{-5}$
Angle of reflection, θ_r	0°	B Rectangular ($\frac{1}{\sqrt{3}}$)	$35 \cdot 10^{-6}$ rad	$-1.78 \cdot 10^{-3}$	$3.60 \cdot 10^{-8}$
Angle of incidence, θ_i	45°	B Rectangular ($\frac{1}{\sqrt{3}}$)	$4.71 \cdot 10^{-5}$ rad	-1	$2.72 \cdot 10^{-5}$
Wavelength detection, $\Delta\lambda$	$500\,nm$	B Rectangular ($\frac{1}{\sqrt{3}}$)	$0.28\,nm$	$2.98 \cdot 10^{-3}$	$4.82 \cdot 10^{-4}$
Linearity of the CCD, L_s	0.0002	A Normal (1)	$6 \cdot 10^{-6}$	0.9998	$6.00 \cdot 10^{-6}$

continued on next page

Table 4.2 – continued from previous page

Input parameters X_i	Estimated value x_i	Distribution type (prefactor a_i)	Standard uncertainty $u(x_i)$	Relative sensitivity coefficient $c_i = \frac{1}{\beta} \cdot \frac{\partial \beta}{\partial x_i}$	Relative uncertainty contribution $\frac{u_i(y)}{y_i} = a_i \cdot \lvert c_i \rvert \cdot \cdot u(x_i)$
Stray light, SL	0.0379	A Normal (1)	$3.60 \cdot 10^{-5}$	0.9635	$3.46 \cdot 10^{-5}$
Transmission of the neutral density filter, T_f	0.001287	B Rectangular ($\frac{1}{\sqrt{3}}$)	$7.51 \cdot 10^{-6}$	777.00	$3.37 \cdot 10^{-3}$
Uncertainty of measurements					$7.60 \cdot 10^{-3}$
Expanded uncertainty of measurements with the coverage factor $k = 2$					1.52 %

The measurements with ARGon^3 in CCD–configuration are similar to the measurements with photodiode–picoamperemeter, but the system of detection is changed. In the case of the measurements with CCD scan–line camera, the monochromator is applied like a spectrometer and the CCD line–scan camera have to be adjusted. The wavelength adjustment with uncertainty values is presented in **Appendix A**.

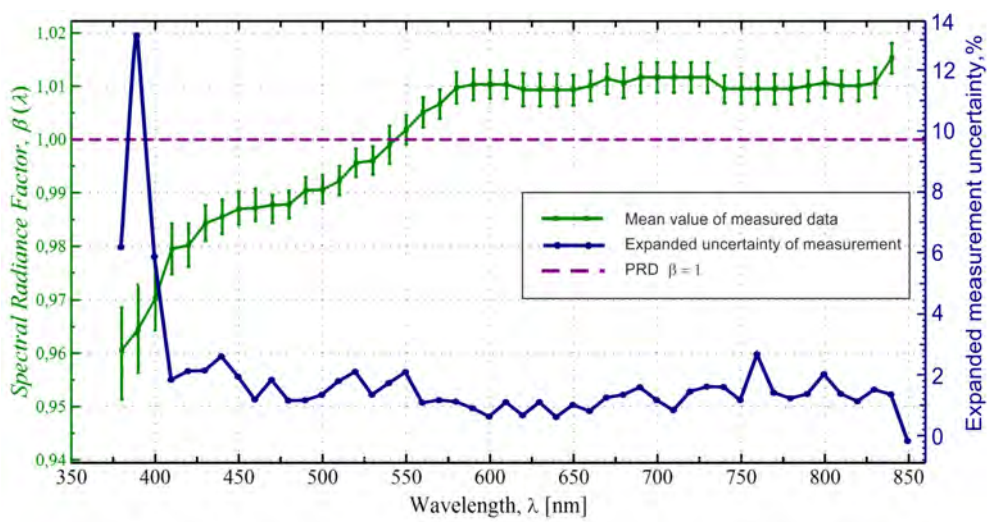

Figure 4.5: Spectral radiance factor of primed barium sulphate (BS 85–15) measurements with ARGon^3 CCD–configuration in the wavelength range from 380 nm to 850 nm with uncertainty

The first four uncertainty components are here of type B. They were evaluated from typical data of single shot measurements with the CCD line scan camera (Hamamatsu S7030–1007) [38].

In Figure 4.5, the measurement uncertainty of the spectral radiance factor for 45°:0° in the $V(\lambda)$–range for with ARGon^3 in CCD–configuration is presented. The mean value of 26 measurements of the spectral radiance factor of the primed barium sulphate sample is displayed by the dark–green solid line with errors bars for the CCD–configuration. The violet dashed line is the spectral radiance factor of the PRD ($\beta(\lambda) = 1$). The calculated measurement uncertainty is depicted by the dark–blue line. The CCD linearity investigation was presented in **Section 3.6.1**. The linearity response of the CCD array is quite high, i.e. 99.98%.
The uncertainty of the ARGon^3 facility is strongly dependent on the transmittance of the ND filter OD 3, which must be added in the optical path to provide the required dynamic range of the CCD line scan camera. The value of transmittance of the ND filter and the measurement uncertainty was taken from [55].

4.3.2.1 Stray–light Effect

The dominant source of stray light in the grating spectrometers is the scattering by the grating. Other sources of stray light for ARGon^3 include: mirror surfaces scattering, the ND filter surface scattering, scattering by inclusions in the material of the ND filter, multiple reflections between surfaces of the filter that create weak out of focus secondary image, Rayleigh and Mie scattering of dust particles in the air within the spectrometer, scattering by housing surfaces, Rayleigh scattering by the volume of glass and fused silica of the CCD array, thermal gradients distortions in the air within the spectrometer, and diffraction on the apertures. The grating ghosts (defects) and specular reflections (glints) from aperture edges and optical element mounts are strongly wavelength dependent and also bring in stray light.
The stray–light correction was realized by the method of simultaneous correction of band-pass and stray–light effects in the CCD array, fully described in [56, 57]. The spectral correction matrix was determined by using the Pulsed Laser setup for Advanced Characterization of Spectrometers (PLACOS) of PTB [58]. The measurements of stray light was done by Dr. Saulius Nevas. The measured signal X is described as

$$X = A \cdot Y \tag{4.10}$$

where A is the instrumental line–spread function (LSF) in matrices form (typically for array spectrometers with matrix is ill–conditioned), Y is the measured signal vector.

A correction for the instrument function can be computed by the inversion of equation (4.10). The solution of equation (4.10) by the matrix inversion is an unstable results with

respect to the small perturbations of the measured signals and the estimated instrument matrix. For the achievement of stable solution to the equation (4.10), the Tikhonov regularization [59] may be applied

$$\|A \cdot Y - X\|^2 + \|\Gamma Y\|^2 \tag{4.11}$$

where $\| \|$ is the Euclidian norm and Γ denotes a suitably chosen regularization matrix and $\Gamma = \alpha I$, where I is the identity matrix and α is the scalar quantity.

According the Tikhonov realization [60]

$$Y_\alpha = (A^T A + \alpha^2 I)^{-1} A^T X \tag{4.12}$$

The correction matrix (C_{Corr}) is

$$C_{Corr} = (A^T A + \alpha^2 I)^{-1} A^T \tag{4.13}$$

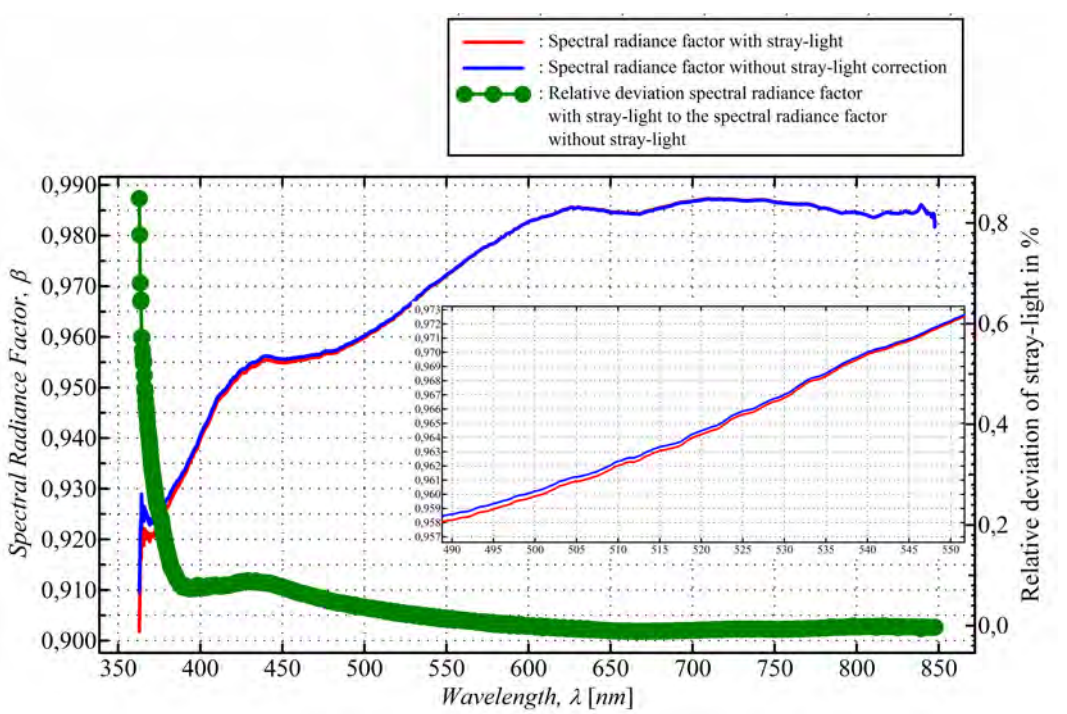

Figure 4.6: Spectral radiance factor of primed $BaSO_4$ without stray–light correction (red line), with stray light correction (blue line) and the stray light (green line)

In figure 4.6, the stray light spectrum is presented. The amplitude of the stray light is strongly dependent on the wavelength and for the spectral radiance factor measurements

these values are about 0.3% for the wavelength range from 350 nm to 400 nm, 0.07% for the wavelength range from 400 nm to 500 nm, and 0.01% for the wavelength range from 500 nm to 850 nm. In the figure 4.6 the spectral radiance factor of the primed barium sulphate without stray light correction is introduced with the blue solid line. The spectral radiance factor of the primed barium sulphate with stray light correction is introduced with the red solid line. The green line depicts the relative deviation of spectral data without stray light correction from the spectral data with stray light correction.

4.3.3 Scale Comparison

The scales of spectral radiance factor measurements for the ARGon^3 facility in CCD–configuration in $V(\lambda)$–range was compared with the Gonioreflectometer facility of PTB. The agreement between the Gonioreflectometer of PTB and the ARGon^3 in CCD–configuration is shown in Figure 4.7.

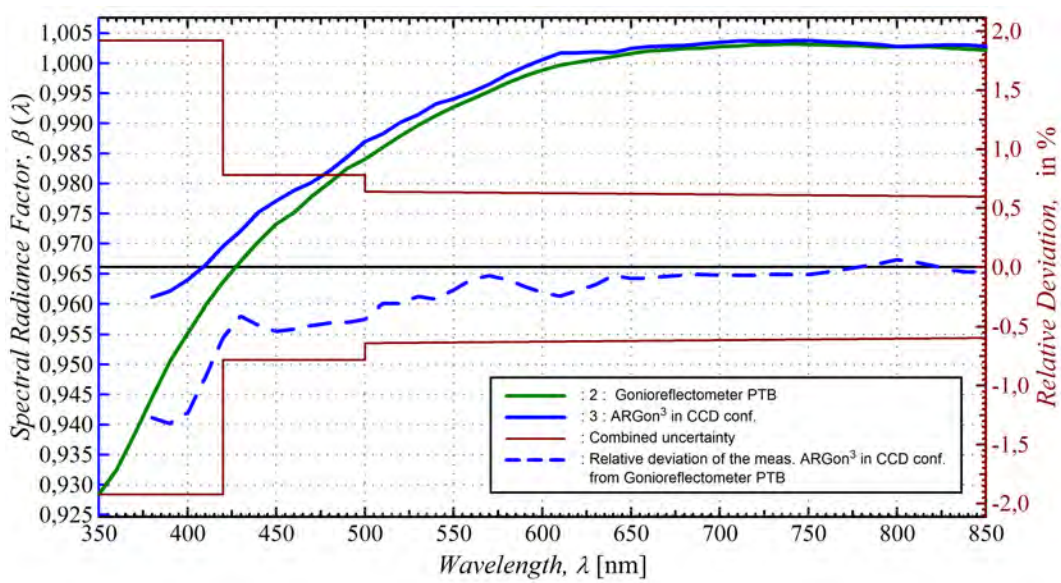

Figure 4.7: The comparison of the spectral radiance factor measurements with ARGon^3 CCD–configuration and Gonioreflectometer PTB

The blue solid line introduces the spectral radiance factor of primed $BaSO_4$ measured with ARGon^3 in CCD–configuration, the green solid line is the spectral radiance factor of the $BaSO_4$ measured with PTB Gonioreflectometer. The blue dashed line in figure 4.4 presents the relative deviation of the data measured with ARGon^3 in CCD–configuration from spectral data measured with PTB Gonioreflectometer. The agreement between the Gonioreflectometer of PTB and the ARGon^3 in CCD–configuration lies in the range of the combined uncertainties of the facilities.

The expanded measurement uncertainty of the ARGon^3 in photodiode–picoamperemeter configuration is $\pm 0.64\%$. The expanded uncertainty of the ARGon^3 in CCD–configuration is $\pm 1.52\%$ at 500 nm and geometrical configuration 45°:0°. The need to use a neutral density filter for improvement of the dynamic range of the ARGon^3 facility in CCD–configuration is the most limiting factor in the measurementuncertainty. The uncertainty of the spectral radiance factor measurement for ARGon^3 with photodiode–picoamperemeter is bigger in the wavelength range from 380 nm to 550 nm because of the low efficiency of the grating of monochromator (see fig. 3.9). The uncertainty of the spectral radiance factor measurement for both ARGon^3 facility configurations is bigger in the same wavelength range because of the lower signal from sphere radiator in this wavelength range (see fig. 3.4).

5 3D–MEASUREMENTS OF STANDARD REFLECTION MATERIALS

The spectral radiance factor of different reflection standard materials was measured with the ARGon^3 in CCD–configuration. For their full description, unique geometrical configurations were applied. At first, the spectral radiance factor of every reflection material was measured in so–called "in–plane" geometries (a configuration where the incident beam, the reflected beam and the surface normal belong to one plane). Secondly, the measurements of the spectral radiance factor of the samples were realized in "out–of–plane" geometrical configuration (an incident beam and a reflected beam that are not located in a common plane with the surface normal). To provide these geometrical configurations, a special measuring map was developed for four θ_i at 0°, 22.5°, 45° and 67.5°. The measurements of the reflected radiation were performed for polar angles θ_r ranging from 0° to 67.5° with steps of 7.5° and at azimuth angles ϕ_r ranging from 0° to 180° with a variable step size for providing nearly equal distances on the hemispherical plane above the sample surface (see Fig. 5.1). The number of recorded test points for the hemisphere measuring map is $N = 229$. For every measured point the coordinates of the robot–rotation stage system was calculated using Euler angles, as it is described in [51,61]. The measurement time was considerably decreased due to the ability to detect signals with the CCD line–scan camera (the measurement time of one test point of the sample was about 4 minutes). The full measurement time of one sample at one incident angle and all reflection angles was about 10 hours. For instance, the same measurements are demanded at least one month, if the photodiode was applied for detecting the signals. Thus, using ARGon^3 in CCD–configuration, it was possible to characterize the three–dimensional spectrally resolved reflection behavior of the standard reflection surfaces in detail.

For illustration of the measured data, the three–dimensional reflection indicatrix was transformed into a modified cylindrical coordinate system in the following way:

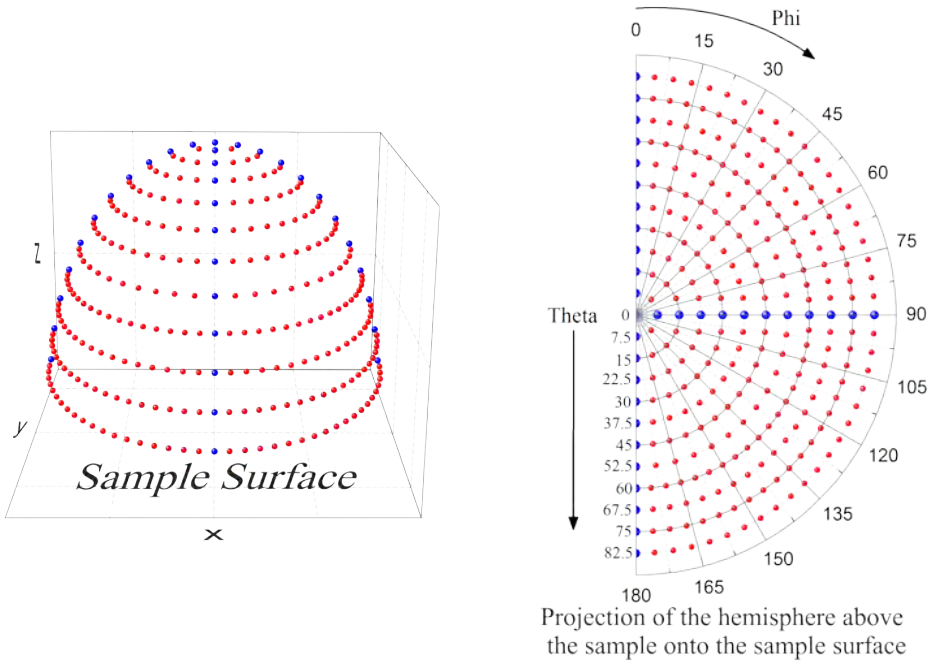

Figure 5.1: 3D–geometry configurations of the spectral radiance factor measurements of standard reflection materials

The cylindrical coordinate system (ρ,ϕ,z) is transformed to (θ_r,ϕ_r,$\beta(\theta_i, \phi_i, \theta_r, \phi_r, \lambda)$). The radial distance ρ is replaced by the polar reflection angle θ_r. The spectral radiance factor $\beta(\theta_i, \phi_i, \theta_r, \phi_r, \lambda)$ is plotted in the z–direction of this coordinate system. Which means that the common radial distance ρ is replaced by the polar reflection angle θ_r, and the spectral radiance factor $\beta(\theta_i, \phi_i, \theta_r, \phi_r, \lambda)$ is plotted in the z–direction. In this coordinate system, the PRD looks like a disk with $\beta(\theta_i, \phi_i, \theta_r, \phi_r, \lambda) = 1$, regardless of the polar incident angle θ_i, the polar reflection angle θ_r and azimuth reflection angle ϕ_r (Fig. 5.2), for all wavelengths [44].

The irradiance in the case of perfectly diffuse reflection depends on a given direction and is proportional to the cosine of the declination angle from the normal to the surface. The flux reflected from a diffuse surface does not depend on the incident direction or the azimuthal angle, in this case, the reflecting surface exhibits a radiance independent of observation angle [13].

But real surfaces show a radiance factor that varies with the wavelength of the incident light and the geometrical configuration of the observation. The appearance behavior of all standard reflection materials is quite different to the behavior of the PRD (see **Appendix B**).

The 3D–indicatrices of a primed barium sulphate sample (BS 85-15) is depicted in Fig-

ure 5.3. The spectral radiance factor of the sample was measured for four polar incident angles θ_i at 0°, 22.5°, 45° and 67.5° and all possible reflection angles θ_r, according to the map presented in figure 5.1. The spectral radiance factor of the sample surface was measured in $V(\lambda)$–range for four incident angles of irradiation and reflection angles according to the map presented in figure 5.1. From the measured data the values of the spectral radiance factor at 400 nm, 550 nm and 700 nm were selected. After that, the 3D optical surface (3D–indicatrix) of the spectral radiance factor at the wavelengths 400 nm and 700 nm was visualized with MatLab in a cylindrical coordinate system, with $\rho = \theta_r$, $\phi = \phi_r$ and $z = \beta(\theta_i, \phi_i, \theta_r, \phi_r, \lambda)$ as described in figure 5.1.

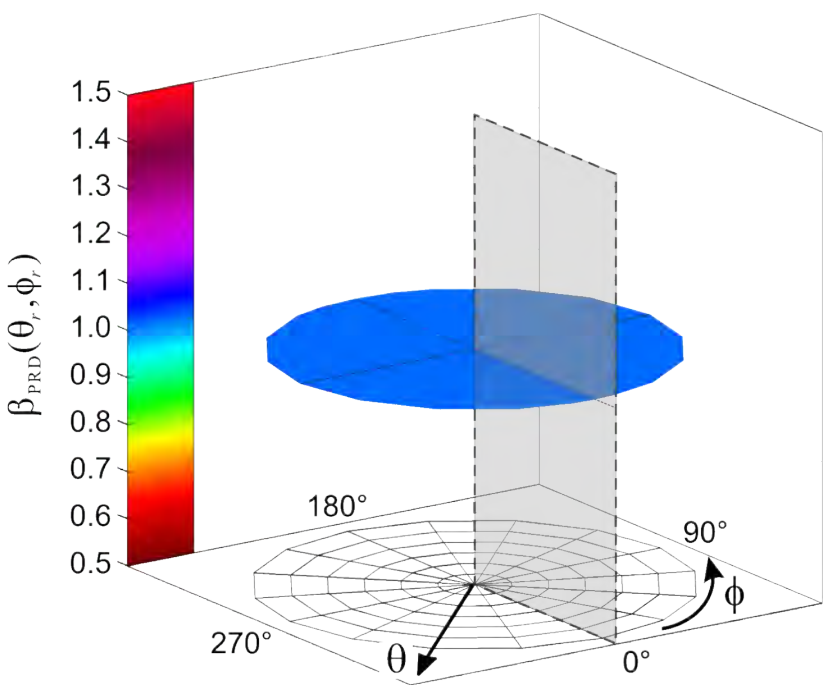

Figure 5.2: Three–dimensional reflection indicatrix of the PRD. The radiance factor is regardless of the incidence angle, the angles of reflection and the wavelength. It realizes by flat disc with a value of unity [44]

In figure 5.3 the reflection indicatrix of a standard reflection primed barium sulphate sample (BS 85–15) at 400 nm (left part of the plot) and at 700 nm (right part of the plot) is shown. Obviously, the appearance of the sample strongly depends on the incident angle as well as on the observation angle and wavelength. That means, for the calibration of commercial devices this fact should be considered and have to be taken into account by adjusting the device scale against the reference standard. For relative measurements of the spectral radiance factor using diffuse reflection standard materials, attention should

be paid to the geometrical configuration, in which the diffuse reflection standard was certified.

The hemispherical indicatrices in figure 5.3 are calculated for four different incident irradiation angles at 0°, b. at 22.5°, c. at 45° and d. at 67.5° and the reflection angle θ_r ranges from 0° to 60° with a step size of 7.5°, the azimuth reflection angle ϕ_r is 0° to 180° with a non–constant step. The hemispherical indicatrices for other standard reflection materials (pressed barium sulphate, matt opal glass, ceramic tile and sintered PTFE) are shown in **Appendix B**.

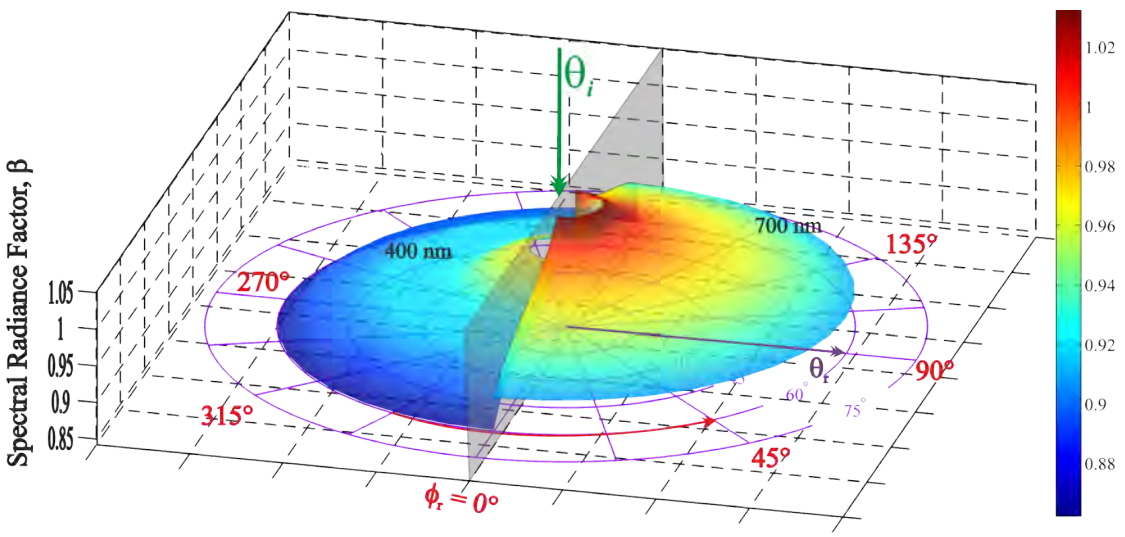

a.

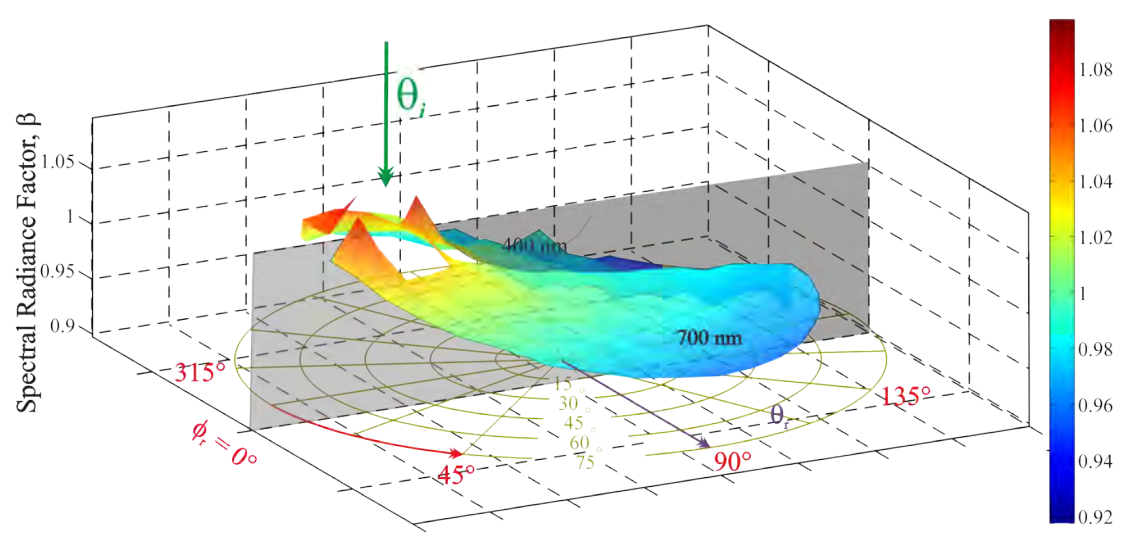

b.

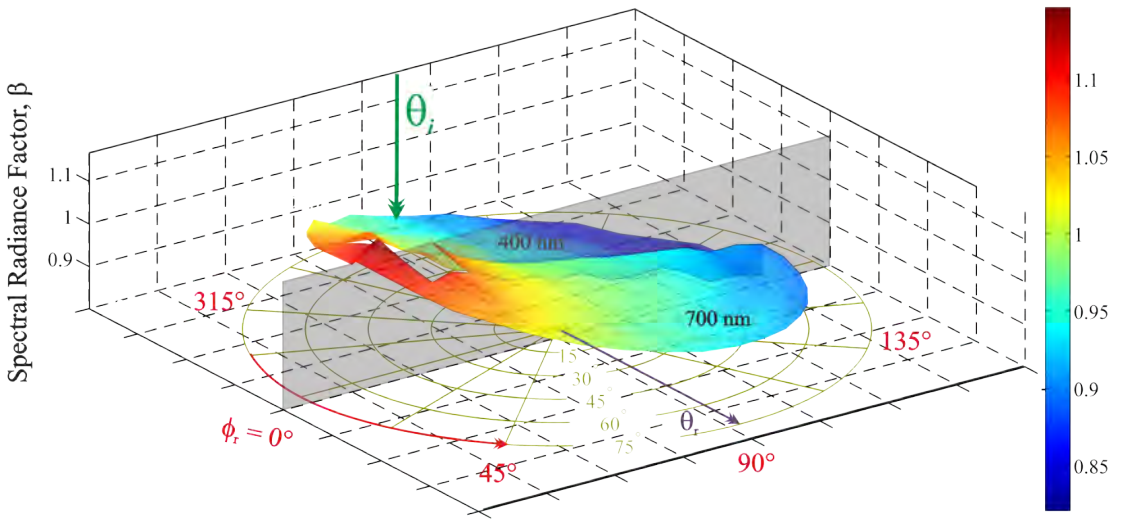

c.

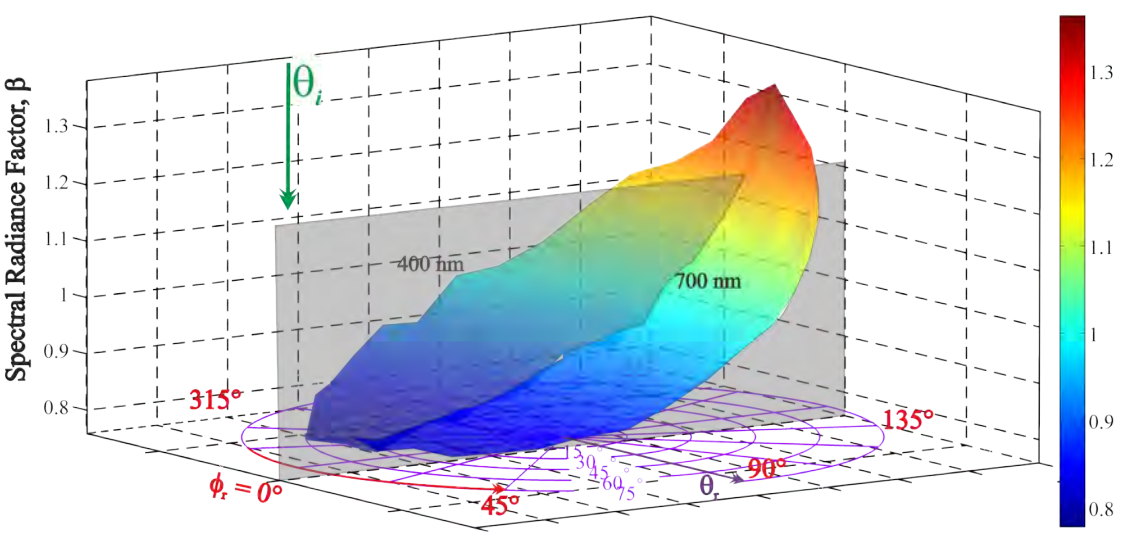

d.

Figure 5.3: Three–dimensional reflection indicatrix of the standard reflection material primed barium sulphate (BS 85–15) for the wavelengths 400 nm (left part of the surface at every plot) and 700 nm (right side of the surface in the plot) at different incident irradiation angles: a. at 0°, b. at 22.5°, c. at 45° and d. at 67.5°

The presented graphics surfaces in figure 5.3 contain an enormous quantity of information about the sample. The "in–plane" indicatrix was derived from the measured three–dimensional data. The "in–plane" indicatrix represents the cross section of the hemispherical indicatrix if the declinate azimuth reflection angle ϕ_r is equal to 0° and

180° (Fig. 5.4) and for three wavelengths at 400 nm, 550 nm and 700 nm (the blue, green and red solid line correspondingly). The cross section for every investigated standard reflection material is presented in **Appendix B**.
From the presented data of the radiance factor, it is clear to see the quite high deviation of the reflection behavior of the standard reflective material from the radiance factor of the PRD.

a.

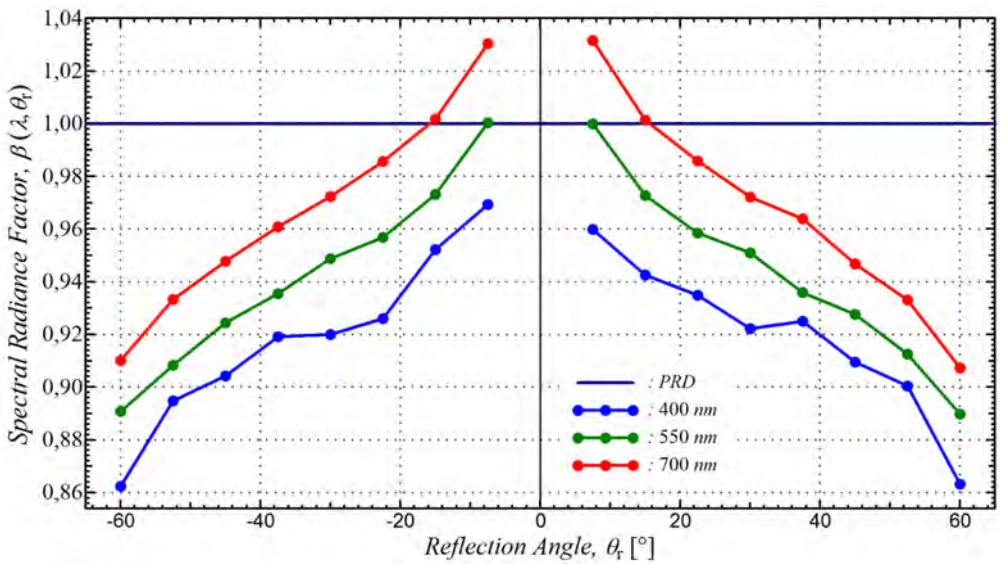

b.

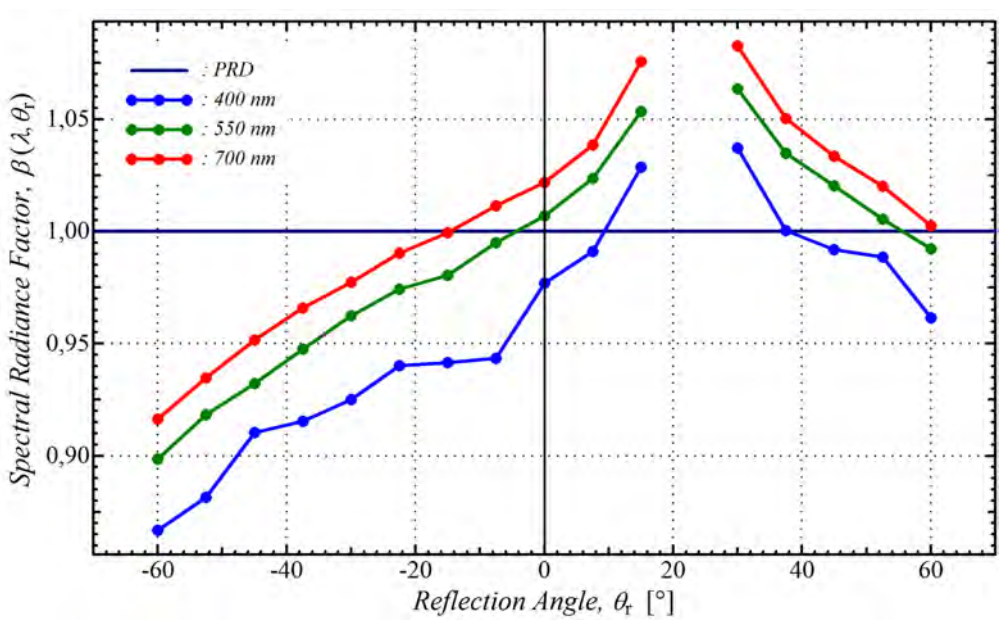

c.

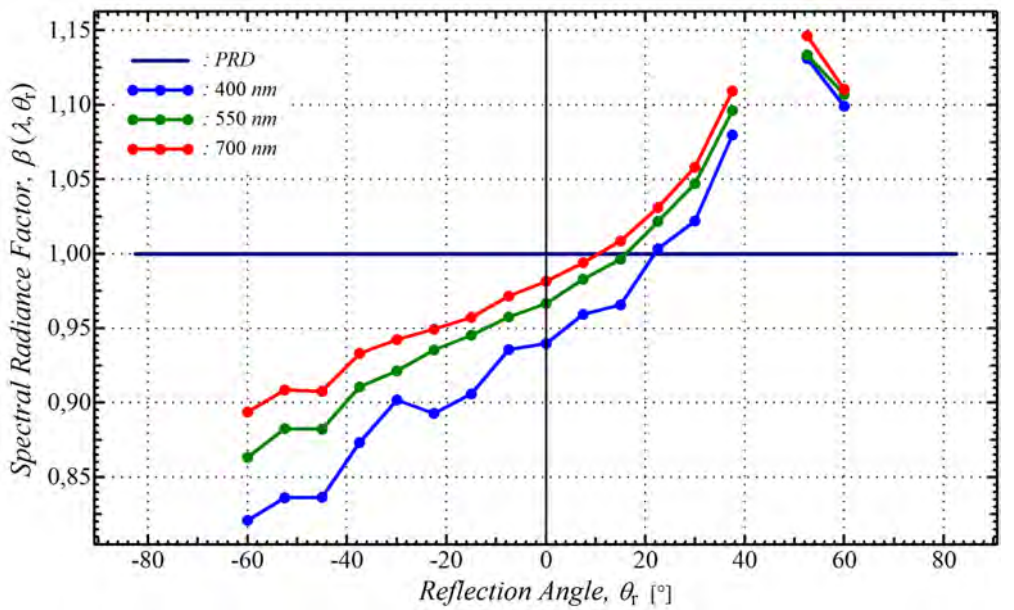

d.

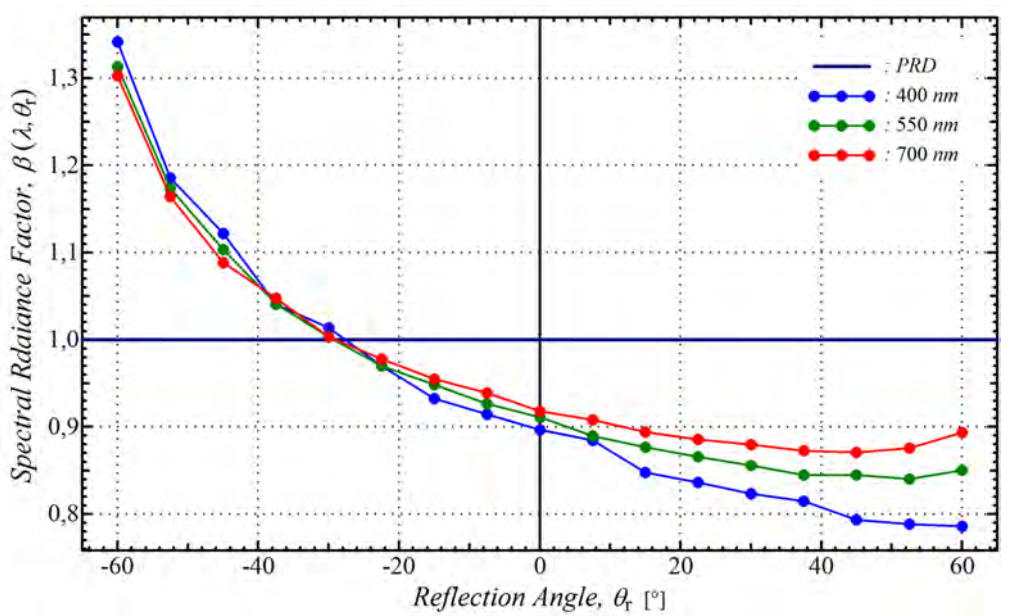

Figure 5.4: The "in–plane" reflection data of the standard reflection material primed barium sulphate (BS 85–15) for wavelengths of 400 nm, 550 nm and 700 nm at different incident irradiation angles: a. at 0°, b. at 22.5°, c. at 45° and d. at 67.5°

Angular resolved reflection data are very relevant to industry. They are an important reference for manufacturers and users of radiometric products. All commercial

instruments need traceability to standard reflection samples for adjusting their spectral radiance factor scale under the recommended standard geometries of the CIE. The full hemispherical reflection indicatrix of five different prevalent reflection materials were measured for wavelengths of 400 nm, 550 nm and 700 nm. The measurements of the spectral radiance factor were done for four incident irradiation angles θ_i of 0°, 22.5°, 45° and 67.5°. It is a widespread conclusion that the standard reflection materials have negligible deviations from the PRD. As can be seen in the figures presented above and figures in **Appendix B**, all the investigated standard reflection materials have quite strong deviations from the PRD, especially for extreme incident irradiation angles. All this leads to incorrect values of the radiance factor and chromatic coordinates of standard reflection materials. It is important to note that, all standard reflection materials reveal the non–Lambertian reflection behavior.

6 EFFECT PIGMENTS

Pigments are used mostly to provide colour to paints, coatings, printing inks, construction materials, ceramics, cosmetics [62]. Pigments are classified by the way they interact with light. The classes of pigments are exemplary presented in figure 6.1. All existing pigments can be classified into the following groups:

- White pigments: These pigments scatter the incident light independent of the wavelength in all directions
- Colored pigments: They absorb certain wavelengths of incident light and scatter other wavelengths
- Black pigments: Such pigments absorb mostly all wavelengths of the visible light
- Effect pigments: They are able to produce and change colours by the interaction with light [63]

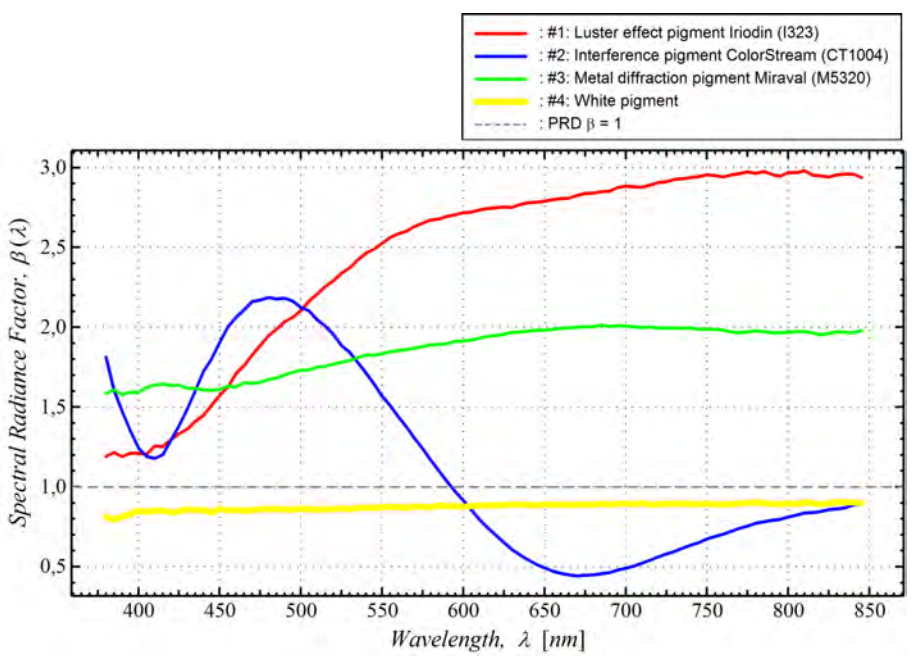

Figure 6.1: Spectral radiance factor $\beta(\lambda)$ of some effect pigments and a typical white pigment for 45°:0° geometry

The effect pigments can give the surfaces additional properties like angular dependence of colour as well as gloss or texture. The colour generation of effect pigments is mostly caused by anisotropic processes like single or multiple reflection, interference or diffraction. The colour appearance of effect pigments is highly angle dependent.
As it was shown in [64, 65], effect pigments need more detailed characterization in comparison to absorption pigments. Most effect pigments consist of flakes (particles), the size of them is between 1 μm and 1 mm and they are more than 10 — 1000 times larger than the size of typical absorption pigments. The thickness of the flakes ranges from 10 nm to 1 μm. Flakes in a layer are oriented typically parallel to the substrate. Effect pigments can have inorganic as well as organic nature. By the nature of the flakes effect pigments, they can be divided into

- Metallic pigments. Metallic pigment coatings contain a thin layer of metallic particles (mostly aluminum). They are not transparent and reflect all incident light in a single direction. In such metal pigments, the particles act as a mirror and the reflectance of these pigments is rather high [62]

- Pearl luster pigments. These pigments have two or more layers. Pearl luster effect flakes represent particles whose orientation can be regulated. The particles in pearl luster pigments have parallel orientation to the surface onto they were applied. Layers in the pigments have a high refraction index (about 1.5 — 2.9). The reflection of pearl luster pigments is quite high becaused of the smooth surface of the pigment platelets. They reflect light selectively. Mica (group of sheet silicate minerals — phyllosilicate) serves mostly as a subtract for this kind of pigments, but metal oxides are also often used. The substrate upper layer of the pearl luster pigment can be transparent for the incident light and the reflection comes partly either from the inner interface of the pigments or from the bottom of the platelets and create the interference phenomena [12].

On one hand pigments effect create additional colours depending on the condition of observation and illumination. On the other hand also, the texture of the substrate surface is able to generate a colour change.
By their optical properties, effect pigments can be classified into interference and diffraction pigments. Interference pigments have different optical layers with different layer thicknesses and refraction indexes. Due to the interaction of light with this larger structure one or more interference orders are created and a variety of colours, according to the observation angle, can be obtained. Pearl luster pigments are quite often in the literature subsumed to the interference pigments [66].
Diffraction pigments form a quite new class of the effect pigments [67]. The metal sub-

strate of diffraction pigments has a grating structure with embossed periodic grooves steps and often the substrate has an additional inorganic coating. As a result, every particle acts as a reflection grating. The structure of the diffraction pigment deflects the incident light and a colour change effect can be obtained. Detailed information about manufacturing of the metal, pearl luster, interference and diffraction effect pigments can be found in [12, 62, 68].

Pearl luster, interference and diffraction effect pigments are also called goniochromatic effect pigments, as goniochromatism (iridescence) [69, 70] is a phenomena of surface appearance to change colour as the angle of observation or the angle of illumination changes. In figure 6.2 the colour diagrams of typical absorption pigments (red, green,blue) and an effect pigment (Viola Fantasy) are shown. The spectral radiance factor of the above mention pigments are measured on the next geometrical conditions: the angle incident radiation is 45°, the reflection angle is varied from 0° to ± 60° with a step in 7.5°.

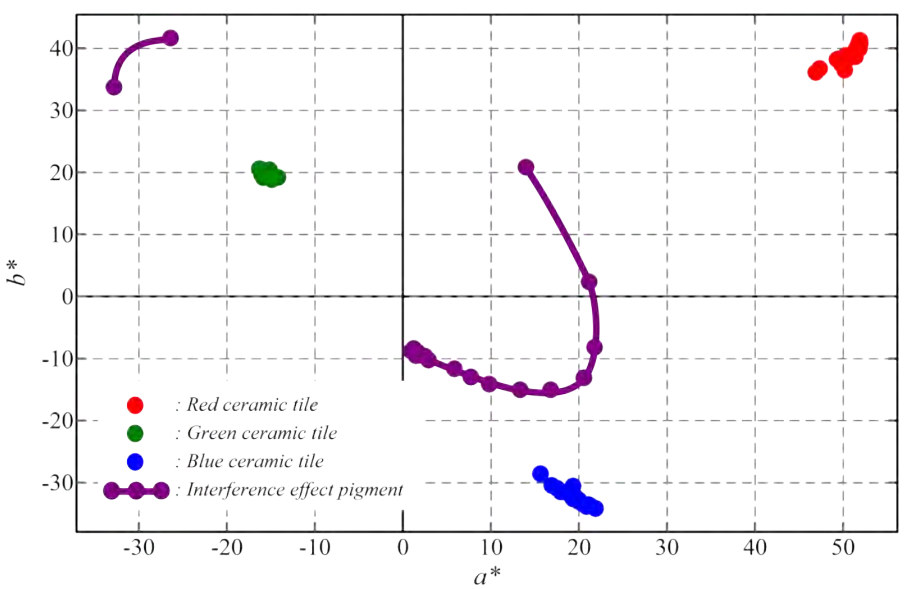

Figure 6.2: Colour diagram of typical absorption pigments (red, green and blue) and the colour changing line (aspecular line 45°:θ_r)of the effect interference pigment Viola Fantasy

The application of effect pigments in modern industry is increasing [12, 62]. The problem of the description of the colorimetric properties of the effect pigments is rather critical today. There are recommendations, norms and standards for the description of absorption pigments [6, 34], but these recommendations are not sufficiently for effect pigments, because of their complicated colour behavior (see Fig. 6.2).

6.1 Measurements of Reflection and Colour of Goniochromatic Effect Pigments

The goniochromatic effect pigments demonstrate a rather high dependence on the illumination and observation angle. For the complete color investigation of such pigments, new geometrical conditions of illumination and observation are recommended. These configurations can be found in [71–75]. Geometrical schemes recommended in standards are depicted in Figure 6.3. All geometries depicted in figure 6.3 are "in–plane" geometries. In figure 6.3 is shown two incident rays at 45° and 15°, and six reflection angles for incident angle 45°, these are so–calling aspecular angles at -15°, 15°, 25°, 45°, 75° and 110°.

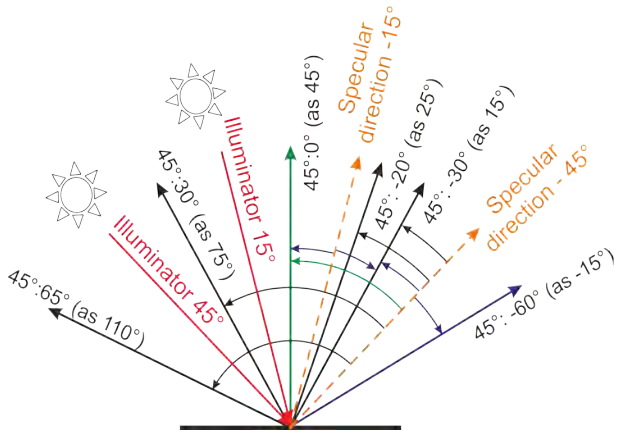

Figure 6.3: ASTM [74] and DIN [75] recommended geometries for the measurement of the spectral radiance factor of goniochromatic pigments (6 aspecular reflection geometries for incident light at 45° and 15°)

The colour changing of effect pigments in colour space is called colour traveling or colour shift. Two main colour traveling schemes are recognized for interference pigments. The aspecular and interference color traveling. The terms aspect and interference line are introduced and are described in [62, 76, 77].
The aspecular colour traveling (aspecular shift) is obtained when the illumination angle is kept constant and the reflection angle is detected for all possible reflection directions as shown in figure 6.4a [78].
The second colour traveling (interference shift) is measured in the following geometrical configuration: the illumination angle is varied from 0° to 85°, the reflection angle is detected at a constant interval (difference between specular angle and detected reflection angle is kept constant) from the direction of specular reflection (Fig. 6.4b). For instance, the illumination angle θ_i is 45°, the specular reflection angle is $\theta_{rS} = 45°$, the aspecular

reflection angle (θ_r) is defined in the displacement at $\pm 15°$ from θ_{rS} [78] (15°–interference line). The displacement between specular angle and detected reflection angle is negative, if the direction is kept off the direction of the light source. This is the so–called trans–interference shift. The interval between incident angle and detected reflection angle is positive, if the direction is counted towards the direction of the light source. This is cis–interference shift.

a.

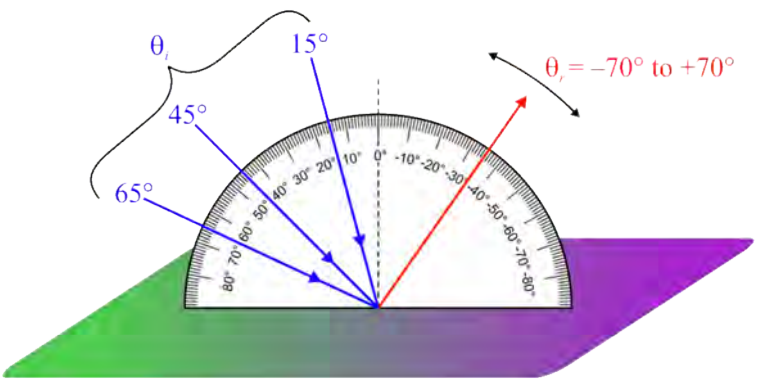

b.

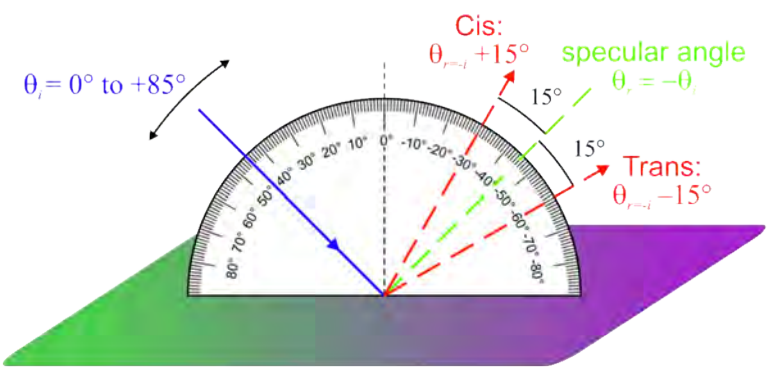

Figure 6.4: Geometrical configurations for the measurement of colour traveling of goniochromatic effect pigments: a. aspecular shift sheme for three incident angles at 15°, 45° and 65°, b. the interference shift with so–called 15° cis–trans–interference shift

The colour traveling was investigated for the goniochromatic effect pigment Viola Fantasy, which is from the Colorstream® interference family of pigments of MERCK, because it shows a manifold goniochromatic behavior. The aspecular shift was investigated for three incident angles of 15°, 45° and 65° and reflection angles from $-70°$ to $+70°$ in 5° step size (26 measurement points for every incident angle). From the spectral radiance factor measured in $V(\lambda)$–range for every geometrical condition the colour coordinates for

colour space $L^*a^*b^*$ for the 10° standard observer and illuminant D65 was calculated and presented in figure 6.5b.

a

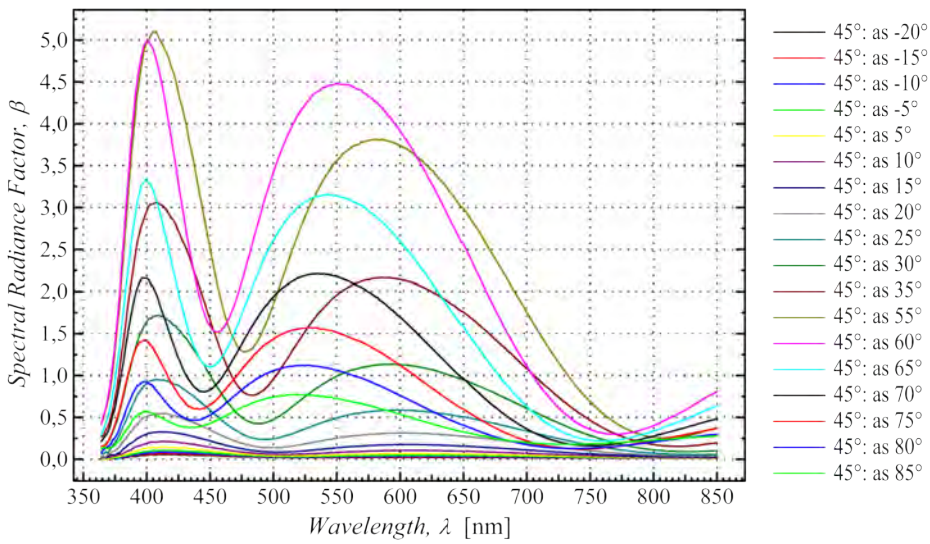

b

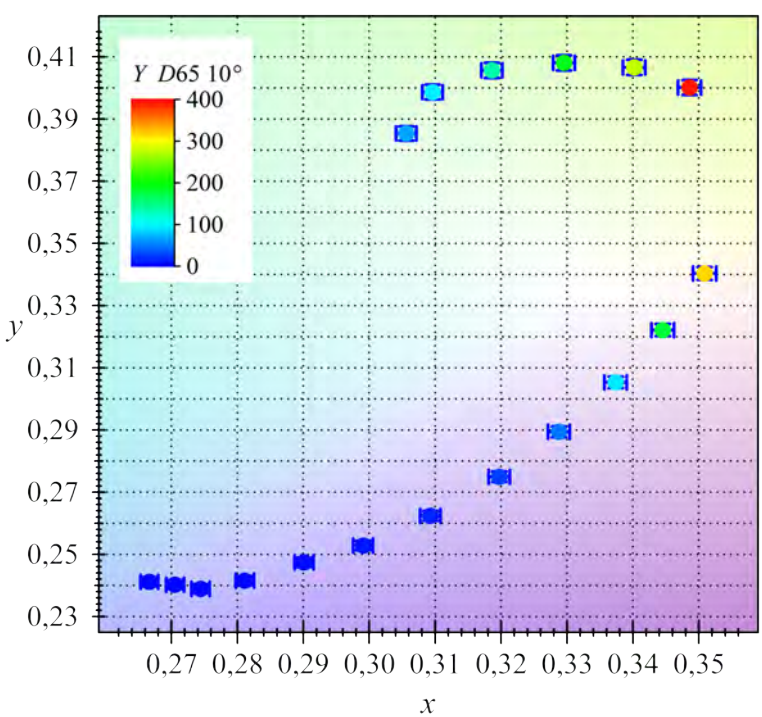

Figure 6.5: Aspecular colour shift of the Viola Fantasy goniochromatic effect pigment at an incident angle of 45° and aspect angles in the range as 85° to as -20°: a. measured spectral radiance factor curves of the pigment, b. chromaticity coordinates

The interference shift scheme for an angular difference of ±15° was also investigated for the same effect pigment. In this case the incident light directions (θ) were varied from 0° to 85° (26 measurement geometries).

a

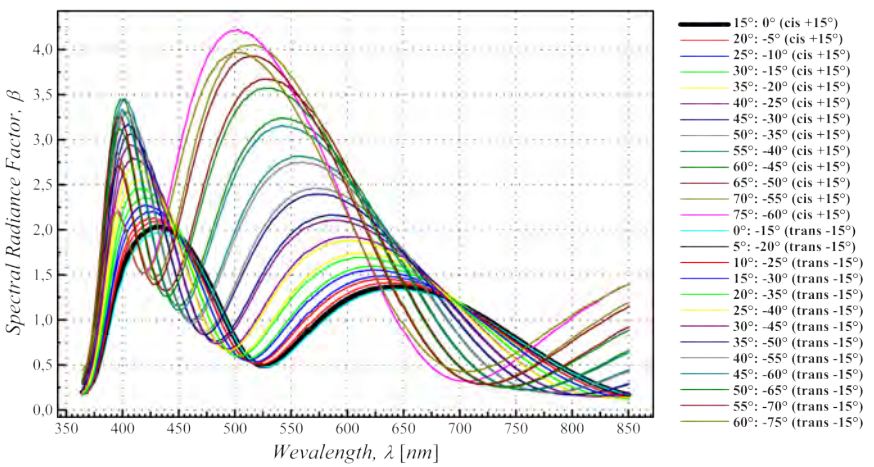

b

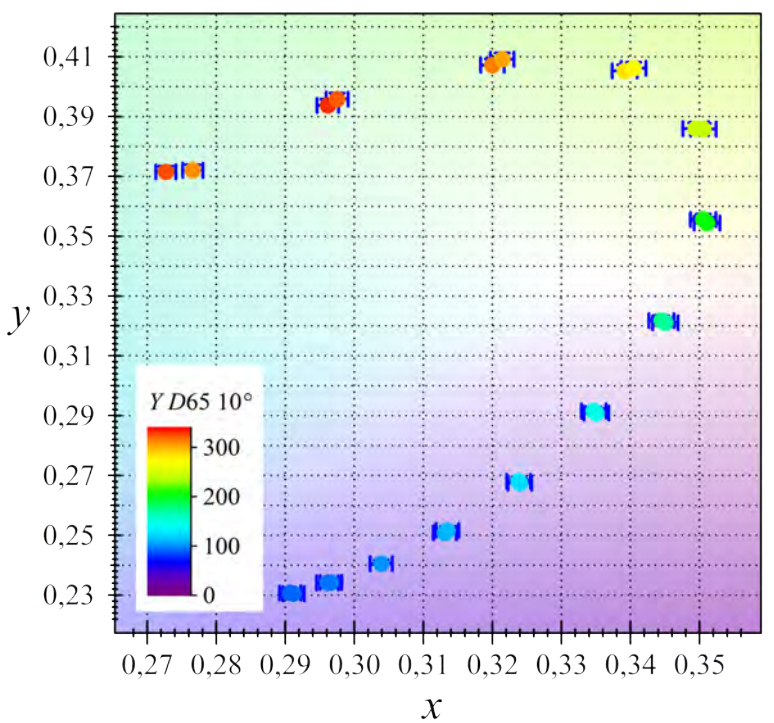

Figure 6.6: Interference colour shift of the Viola Fantasy goniochromatic effect pigment for cis– (+15° from specular reflective direction) and trans–configuration (−15° from specular reflective direction): a. measured spectral radiance factor curves of the pigment, b. chromaticity coordinates.

The spectral radiance factor for every geometrical configuration was measured and calculated. After that, the colour coordinates $L^*a^*b^*$ were computed. The data can be visualized in figure 6.6.
All color data were measured with the ARGon^3 facility in CCD–configuration for the goniochromatic effect pigment Viola Fantasy. The results are shown in one map (see Fig. 6.7). In black circles are depicted the recommended ASTM E 2194–03 [72] and DIN 175–2:200–03 [75] geometries for such kind of effect pigments. In green circles are the color data for the additional illumination at an angle of 15°.

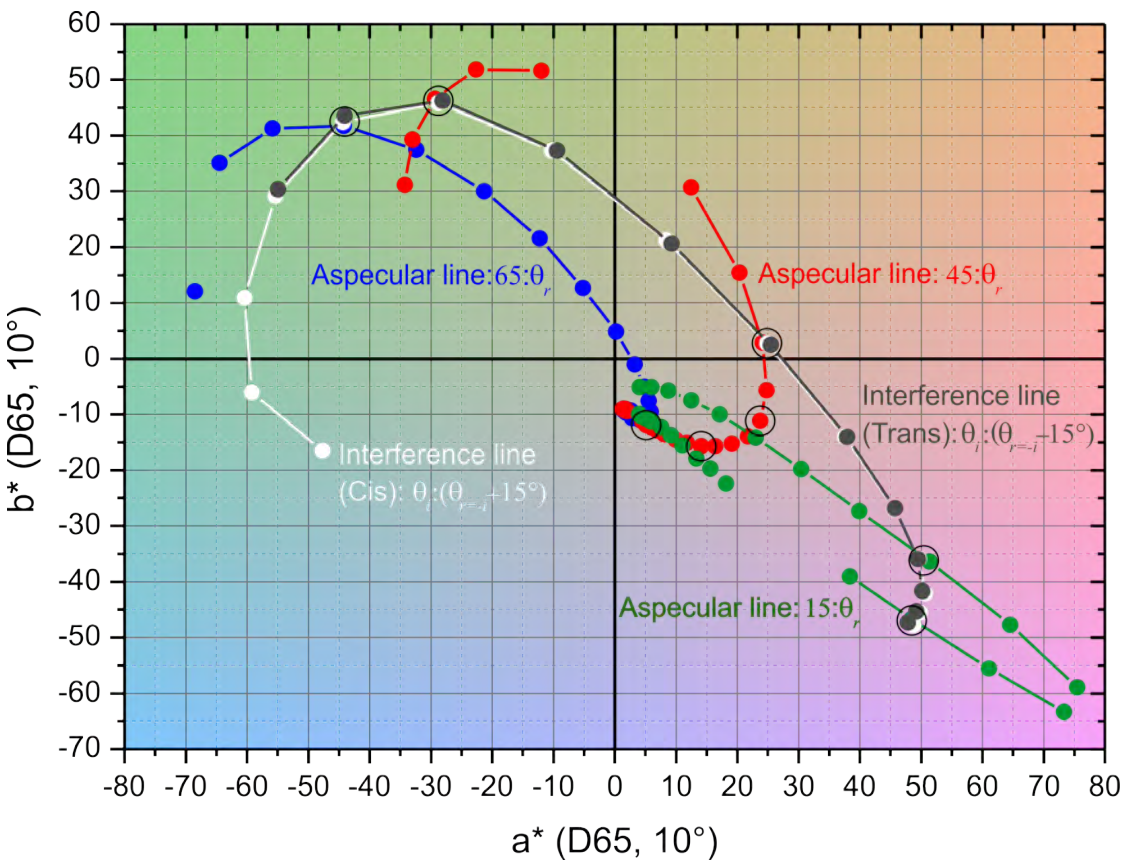

Figure 6.7: ASTM [74] and DIN [75] recommended geometries for the measurement of the spectral radiance factor of goniochromatic pigments (8 aspecular reflection geometries: 6 for incident light at 45° in black circles and 2 for 15° in green circles). The coloured background of the map is a visualization of the observed colours of the effect pigment.

The white line in figure 6.7 is the interference cis–colour travel of the goniochromatic effect pigment Viola Fantasy; the black line is the interference trans–colour travel. The green line is the 15°–aspecular color travel; the blue line is 65°–aspecular colour travel and the red line is 45°–aspecular colour travel of the goniochromatic effect pigment Viola

Fantasy.
45°:0° and 0°:45° illumination/observation geometries for colour characterization of reflection surfaces are traditional recommended. These geometries definitely do not give us full knowledge about the colorimetric behavior of complex goniochromatic effect pigments, as it can be conclude from the colour travel depicted in figure 6.7 the using of described in figure 6.4 geometries is necessary, in order to get full colour information about the goniochromatic effect pigments.

6.2 Polarization Effects in the Measurement of Reflection Properties of Effect Pigments

Considering that effect pigments contain metal particles, a polarization effect can be obtained by the reflection of the incident light from the surface of the pigment. Especially, this effect occurs for extreme angles of illumination and observation. The polarization behavior was measured for the interference effect pigment Viola Fantasy at θ_i=45° and θ_r=-30° for wavelengths from 380 nm to 780 nm.
For the measurements of the polarization effect of the sample, a Rochon Prism polarizer was added to the optical path of the ARGon^3 facility in the position nearby the second aperture. The optic axis of the first calcite prism section of the Rochon prism expands in the direction of the incident ray (Fig. 6.8). There is no distinction between the o–ray (ordinary) and the e–ray (extraordinary) in this first section.

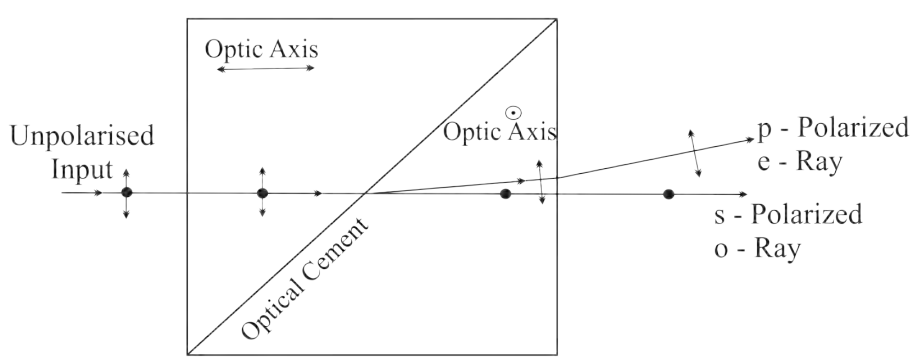

Figure 6.8: Principle sketch of a Rochon Prism Polarizer

The split at the second section interface produces no deviation of the s–polarized (electric field vector perpendicular to the plane of incidence) o–ray, while the p–polarized (electric field vector parallel to the plane of incidence) e–ray is deviated from the interface normal [79–81].

a.

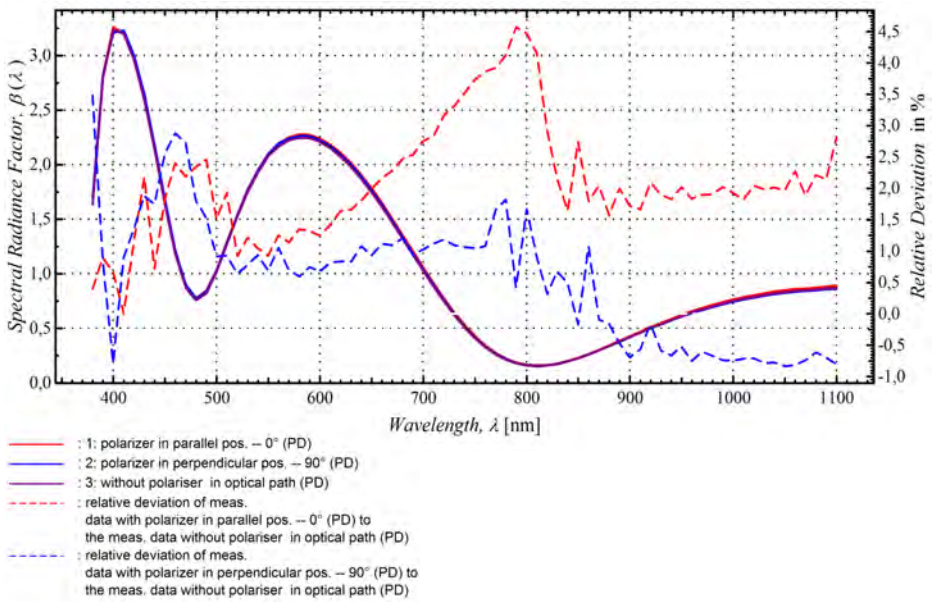

b.

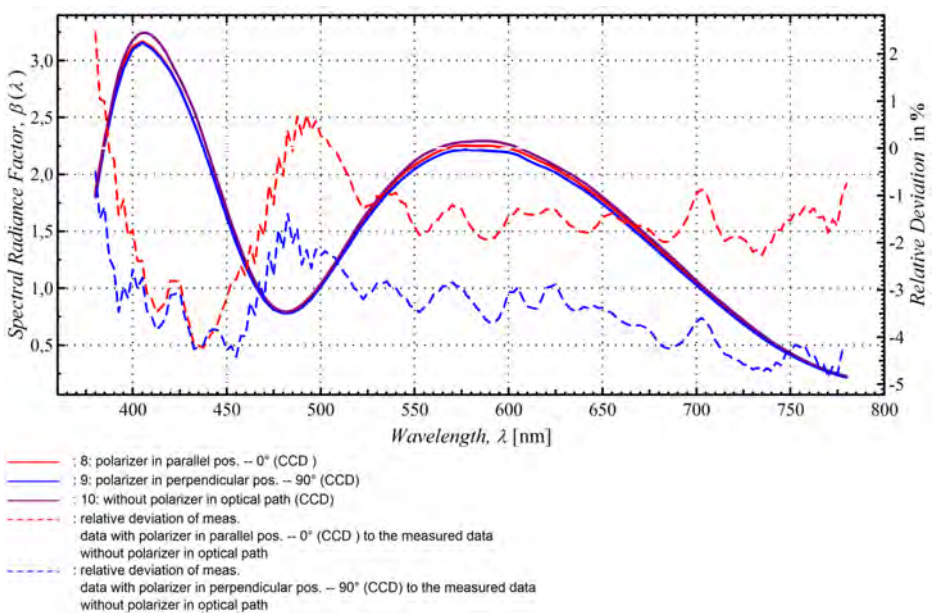

Figure 6.9: The influence of the polarization effect on the measurements of the spectral radiance factor of interference effect pigment Viola Fantasy with : a. ARGon^3 in photodiode–picoamperemeter configuration , b. ARGon^3 in CCD–configuration

The spectral radiance factor of the interference effect pigment Viola Fantasy with the Rochon prism polarizer in the optical path for ARGon^3 in photodiode–picoamperemeter configuration is presented in figure 6.9a, the same measurements for ARGon^3 facility in

CCD–configuration are presented in figure 6.9b. The red solid line depicts the spectral radiance factor measured with polarizer at 0°–position (parallel). Blue solid line presents the specular radiance factor of the Viola Fantasy with the polarizer at the perpendicular position at 90°. Violet solid line is the spectral radiance factor of the Viola Fantasy without polarizer in the optical path. The relative deviation between the measurements is also presented in the figure 6.9 with dashed lines. The red dashed line represents the relative deviation between p–polarized (parallel) signal and signal without the polarizer in the optical path. The blue dashed line presents the relative deviation between the s–polarized (90°–position) signal and signal without the polarizer.
The deviation of the radiance factor for both configurations is quite high. A strong dependence of the reflective signal from the polarization was detected; more than 2% for measurements with ARGon^3 photodiode–picoamperemeter configuration (Fig. 6.9a) and more then 4% for measurements with ARGon^3 in CCD–configuration (Fig. 6.9b).
Moreover, the intensity of the unpolarized signal was calculated. If a perfect polarizer (a perfect polarizer would transmit only 50 percent of an incident unpolarized light signal) is placed in a plane–polarized light beam and rotated about an axis parallel to the beam direction, the transmitted light signal S will vary between a maximum value S_1 and a minimum value S_2 according follow equation [82, 83]

$$S = (S_1 - S_2) \cdot cos^2(\theta) + S_2 \tag{6.1}$$

Although the quantities S_1 and S_2 are called the principal transmitted signal, θ is the angle between the plane of the transmitted signal and the plane of oscillation of the electric vector of the incident light. Transmitted signal for unpolarized light is

$$S = \frac{S_1 + S_2}{2} \tag{6.2}$$

The light produced by the sphere radiator of ARGon^3 facility is unpolarized, while the light from lamp suffers a number of reflection from the inner walls of the sphere before it comes out of the sphere radiator. The polarization effect is probably caused by the glossy surface of the goniochromatic effect pigment and high reflection of the metal particles contained (Fresnel polarization). The $L^*a^*b^*$ colour coordinates calculated from the spectral radiance factor with and without the polarizer in the optical path, however, have a quite negligible deviation, as it can be seen in Table 6.1 and in figure 6.10. A more detailed investigation of the polarization effects by the reflection from the effect pigment surface should be carried out.

Table 6.1: L*a*b* colour coordinates of the interference effect pigment Viola Fantasy dependency on polarization

Colour coordinate	Polarizer at the parallel position, $S_{\parallel}$	Polarizer at the perpendicular position, $S_{\perp}$	Without Polarizer at the optical path, $S_{without}$	Calculated unpolarized value $S = \frac{S_{\parallel}+S_{\perp}}{2}$
ARGon^3 in photodiode–picoamperemeter configuration				
L*	126.6	126.7	126.2	126.7
a*	22.1	22.1	21.8	22.1
b*	5.65	6.31	6.44	5.98
ARGon^3 in CCD–configuration				
L*	124.8	126.8	125.4	127.1
a*	21.5	21.2	21.3	21.6
b*	5.85	6.76	6.31	5.74

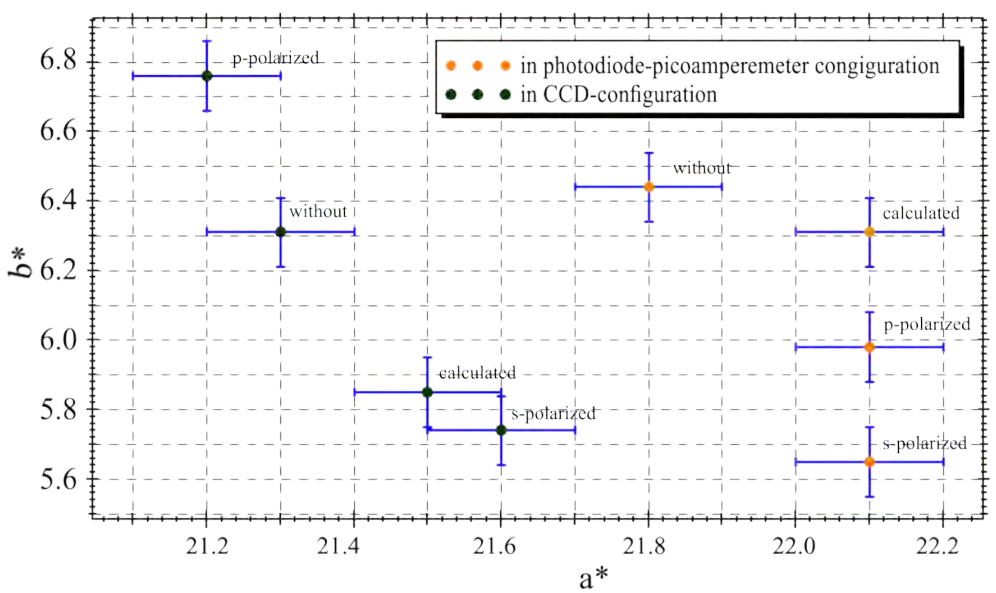

Figure 6.10: a*b* colour data of the Viola Fantasy effect pigment with and without polarizer in the optical path (blue points – ARGon^3 in CCD–configuration, orange points – ARGon^3 in photodiode–picoamperemeter configuration)

6.3 3D Colour Measurements

10 water–based inks containing different effect pigments samples of the product series Iriodin®, Colorstream® and Miraval® were provided by MERCK KGaA. The samples were printed by the Institute of Printing Science and Technology of the Technische Universität Darmstadt (IDD). The table 6.2 itemizes the kinds of selected effect pigments and their flake diameter. The classification of investigated effect pigments were performed according to the MERCK classification

- silver white (SW)
- gold (G)
- iron oxide (IO)
- interference effect (IE)
- multi-color (MC)
- sparkle (S)

Presented in table 6.2 are the effect pigments measured with the ARGon^3 in CCD–configuration. The measured geometrical configurations applied for detecting the spectral radiance factor are the same as in **Chapter 5**. The geometrical configuration map is presented in figure 5.1. From the spectral data the colour coordinates for the $L^*a^*b^*$ colour space are computed. The color data are presented in figures 6.11.

Table 6.2: Special effect MERCK pigments

Code	Name	Class	Diameter	Concentration
I123	Iriodin Bright Luster Satin	SW	5 μm – 25 μm	25 %
I323	Iriodin Royal Gold Satin	G	5 μm – 25 μm	25 %
I4504	Iriodin Lava Red	IO	5 μm – 50 μm	25 %
I211	Iriodin Rutil Fine Red	IE	5 μm – 25 μm	25 %
I231	Iriodin Rutil Fine Green	IE	5 μm – 25 μm	25 %

Continued on next page

Table 6.2 – continued from previous page				
Code	Name	Class	Diameter	Concentration
CF1000	Colorstream Autumn Mystery	MC	5 μm – 50 μm	20 %
CT1002	Colorstream Arctic Fire	MC	5 μm – 50 μm	20 %
CT1003	Colorstream Tropic Sunrise	MC	5 μm – 50 μm	20 %
CT1004	Colorstream Lapis Sunlight	MC	5 μm – 50 μm	20 %
M5320	Miraval Scenic Gold	S	10 μm – 100 μm	15 %

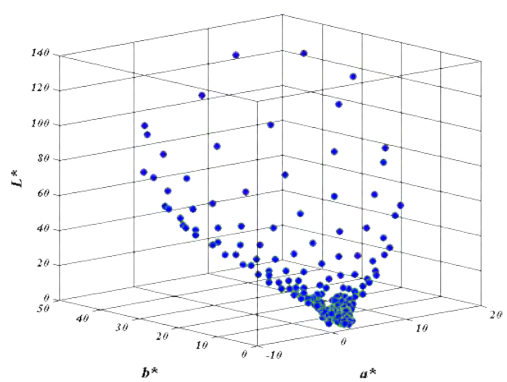

a.

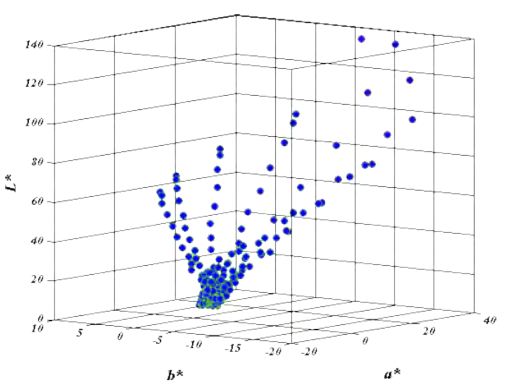

b.

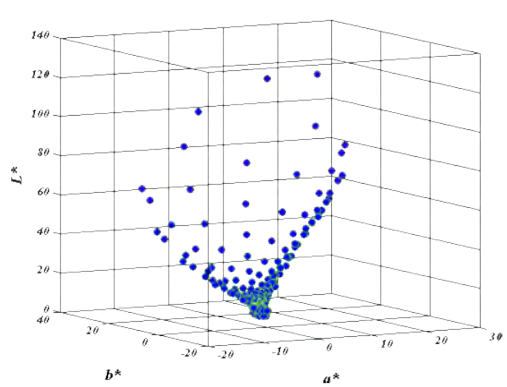

c.

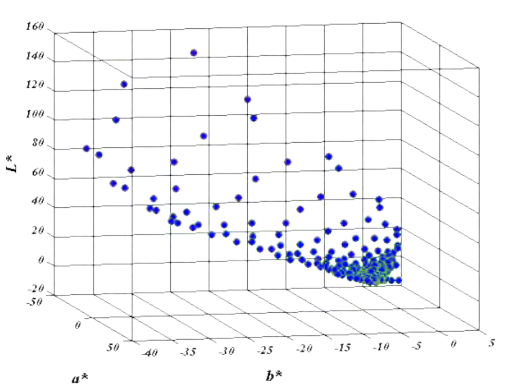

d.

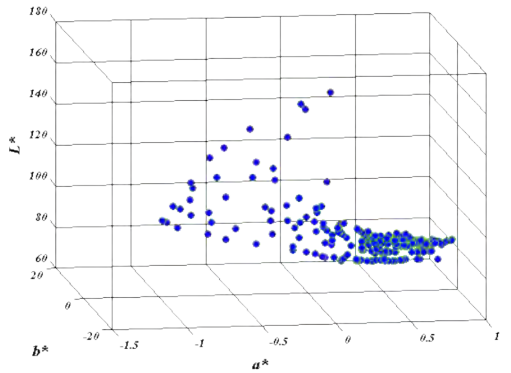

e.

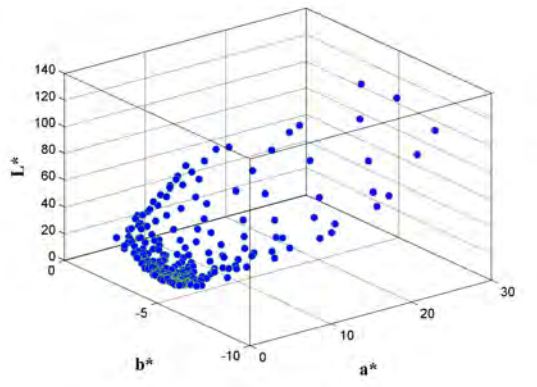

f.

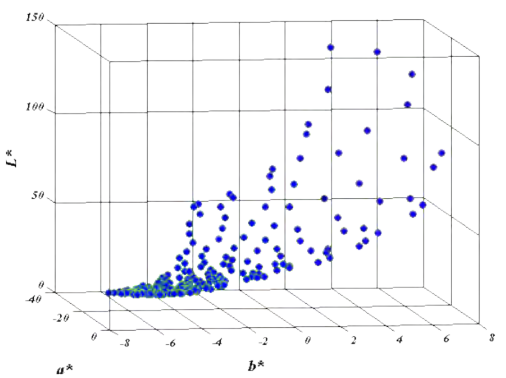

g.

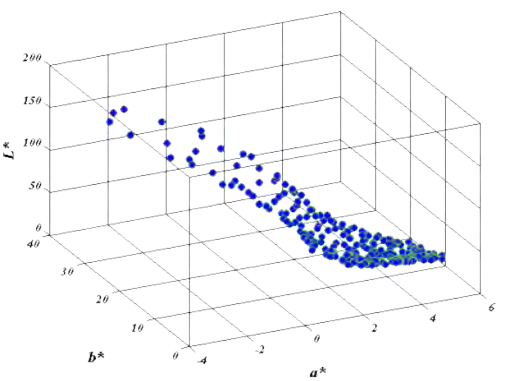

h.

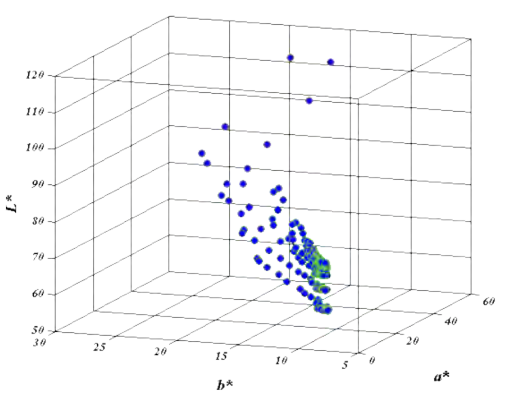

i.

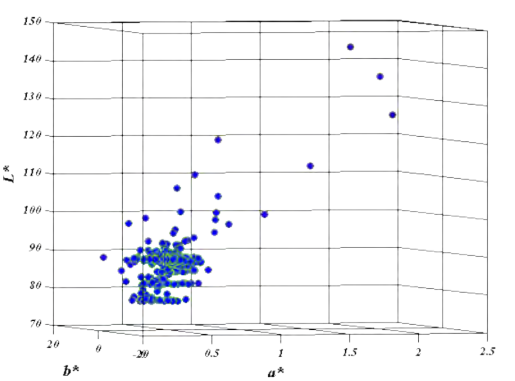

j.

Figure 6.11: L*a*b* colour data of effect pigments: a. Colorsteram Autumn Mystery, b. Colorsteram Arctic Fire, c. Colorsteram Tropic Sunrise, d. Colorsteram Lapis Sunlight, e. Iriodin Bright Luster Satin, f. Iriodin Rutil Fine Red, g. Iriodin Rutil Fine Green, h. Iriodin Royal Gold Satin, i. Iriodin Lava Red, j. Miraval Scenic Gold

The colour coordinates can be calculated from the radiance factor and represented in three–dimensional CIELAB [28, 84]. This computation is performed for every measured surface. 3D geometries show the full colour behaviour, which effect pigments are create. The plots in figure 6.11 display the unique form of colour point for every every class of effect pigments. Actually, it could be useful to make 3D measurements of the effect pigments, but otherwise, the multi–angle commercial devices that employ either a fixed angle of irradiation and several angles of reflection, or vice–versa. The using of absolute measurements equipment is quite expensive and take a considerable time.
As it can be seen from plots in figure 6.11, the lightness of the colour (L^* value) is large than 100, that is accurately irrational. The problem is that, the classification of colour data is well adapted for diffuse reflection surfaces whose colour is almost independent of the condition of illumination and observation. But for glossy and varnished surfaces the colour is quite difficult to describe due to the high dependance on the viewing direction. The CIELAB color space was developed with the respect to the PRD, but in the case of glossy surfaces the L^* value (lightness of the colour) can easily reach values higher than 100.
By the angular colorimetric variations, two kinds of reflective surfaces have special importance: Lambertian (diffuse) and the specular reflective surfaces [42]

- Lambertian reflective surfaces (model is PRD) are defined by a spectral radiance factor $\beta(\theta_i, \phi_i, \theta_r, \phi_r, \lambda)$ and independent of the incident angle of illumination and observation direction. Its radiance factor is constant and equal to 1. The Lambertian reflective surface is a "perfect white" for CIELAB colour space, PRD absorbs no light and CIELAB coordinates are $(L^*_{PRD}, a^*_{PRD}, b^*_{PRD}) = (100, 0, 0)$.

- Specular reflective surfaces are "perfectly specular" when they reflect a collimated incident light into a certain direction. Its reflectance ρ is a function of the irradiation angle θ_i. Light is reflected at the angle θ_r and the azimuth angle ϕ_r according to Snell's laws (light is reflected at the angle θ_r and the azimuth angle $(\phi_r+\pi)$ and in the other directions, light is not reflected).

The radiance coefficient by the definition is quite close of the spectral radiance factor $(\beta(\lambda))$ and it is the ratio of the radiance $(L(\theta_i, \phi_i, \theta_r, \phi_r))$ to the irradiance (E_i).

$$L^{PRD} = \frac{E_i}{\pi} \tag{6.3}$$

The relation between radiance coefficient and spectral radiance factor follows from equation (6.3)

$$q(\theta_i, \phi_i, \theta_r, \phi_r) = \frac{\beta(\theta_i, \phi_i, \theta_r, \phi_r)}{\pi} \tag{6.4}$$

The BRDF is the ratio of the differential radiance of a ray reflected in a given direction (θ_r, ϕ_r) to the differential irradiance incident from a given direction of incidence, (θ_i, ϕ_i), that produces it, as it was described in **Chapter 4**. The BRDF describes the evolution of radiance coefficient $q(\theta_i, \phi_i, \theta_r, \phi_r)$ according to the direction of irradiation and observation (reflection).The BRDF can be calculated through the viewing angle α of the irradiator, its reflectance ρ and the irradiation angle θ_i as it shown in figure 6.12 [42].

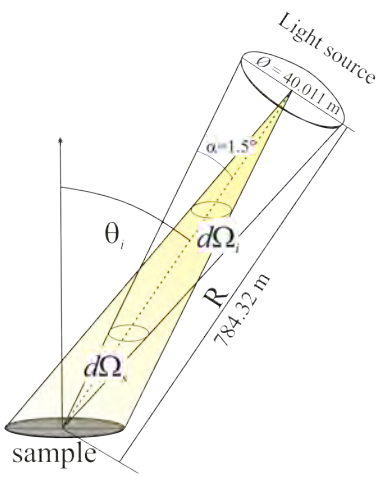

Figure 6.12: Viewing angle of ARGon^3 facility spherical light source

For the ARGon^3 facility the distance to the point light source is equal 784.32 mm. The aperture area of the surface element of the spherical light source is 1257.35 mm^2 with the diameter d 40.011 mm. From these data, the viewing angle of the light source can be calculate as

$$tan(\alpha) \approx sin(\alpha) = \frac{2R}{d} \approx 1.5^\circ \tag{6.5}$$

The the radiance coefficient $q(\theta_i, \phi_i, \theta_r, \phi_r)$ can be expressed by the bidimensional Dirac Delta function as specular reflection is obtained [42]

$$q(\theta_i, \phi_i, \theta_r, \phi_r) = \rho(\theta_i) \cdot \frac{\delta(\theta_r - \theta_i) \cdot \delta(\phi_i + \pi - \phi_r)}{cos(\theta_r) \cdot sin(\theta_r)} \tag{6.6}$$

The solution of equation (6.4) for reflectance according to the viewing angle of the radiator, reflectance factor and reflection angle (θ_r) (see [42]), and according to the assumption

of specular reflection is

$$R(\theta_r, \phi_r) = \begin{cases} \frac{\rho(\theta_i)}{sin^2(\alpha) \cdot cos(\theta_r)}, & (\theta_i, \phi_i + \pi) \in \Delta\Omega_r \\ 0 & \text{otherwise} \end{cases} \tag{6.7}$$

When $\rho(\theta_i) = 1$, the incident light is reflected without attenuation. This is the case of the so–called "perfect mirror". Its reflectance factor depends only on the geometry of the measurement. This is the first case of the equation (6.6), so $R(\theta_i) = 1$ and $\theta_i = \theta_r$ for the specular direction. The spectral radiance factor of a “perfect mirror” (γ) can be expressed as

$$\gamma = \frac{1}{sin^2(\alpha) \cdot cos(\theta_i)} \tag{6.8}$$

For the perfect mirror, the colour coordinates in the specular direction in CIELAB color space with respect to the PRD is $L^*_M = (\gamma^{\frac{1}{3}} \cdot 116 - 16)$ and $(a^*_M, b^*_M) = (0, 0)$. The colour coordinates of a perfect mirror is located on the achromatic axis of the CIELAB colour space. The perfect mirror has brighter color than the PRD [42], because its γ is much larger than 1, thus the lightness coordinate of the perfect mirror is larger than the lightness coordinate of the PRD, $L^*_M > L^*_{PRD}$. All this might mean that, for glossy surfaces other method of normalizing of the CIELAB colour space should be applied. In [42] the method of the normalization of CIELAB colour space against the "perfect mirror" (perfect specular surface) was performed and described.

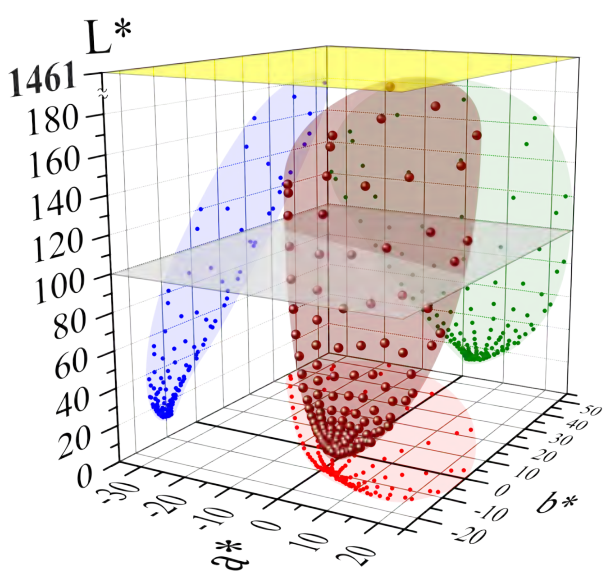

Figure 6.13: L*a*b* colour coordinates of the glossy Viola Fantasy effect pigment. The transparent grey surface shows the L* colour coordinate of the PRD, the yellow transparent surface image the lightness of the perfect mirror

For instance, we illuminate a perfect mirror surface at an angle of θ_i at 45°, so the specular reflection angle (θ_{rS}) is at $-45°$. The colour coordinates calculation of CIELAB colour space was calculated for the viewing solid angle of the detector at 10°. The spectral radiance factor of a "perfect mirror" (γ) for this geometry illumination and viewing angle from the equation 6.5 is

$$\gamma = \frac{1}{sin^2(1.5°) \cdot cos(45°)} \approx 2064 \quad and \quad L^*_M \quad thus \quad (L^*_M) = (2064^{\frac{1}{3}} \cdot 116 - 16) \approx 1461$$

Becaused the varnished surface and high reflective particles of the goniochromatic effect pigments have gloss. In the result, the lightness value L^* of the glossy goniochromatic effect pigments (such for instance Viola Fantasy is) in colour space CIELAB is larger than 100 (Fig. 6.13) and their colour could not be defined in classic CIELAB colour space as the colours with the lightness value over 100 are not exist. The classical CIELAB colour space was established for classic absorption colour surfaces and pigments. As a result, the colour space was normalized on the perfect reflective diffuser with the colour coordinates (100,0,0), while the behavior of classic absorption colour surfaces and pigments are mostly defined in terms of diffuse reflection. For glossy and high reflective surfaces with the specular reflection component, the classical normalizing CIELAB colour space is unsuitable. Modern varnished surfaces and goniochromatic effect pigments show the lightness values large than 100 for specular and near–specular reflection direction. The other way have to be applied for the normalization of CIELAB color space in order to describe the colours of glossy goniochromatic effect pigments. The approach model for such normalization can be the perfect mirror as shown in [42]. After normalizing of colour space on the perfect mirror, the colour value (L^*) of the perfect mirror for the above described geometry is 1461. The colour data of effect pigment Viola Fantasy make sense in such normalizing CIELAB color space. The method described by L. Simonot is quite suitable to apply and to use for all vanished effect pigments and glossy surfaces in order to describe their complicated colour behavior.
From one side, the normalization of the lightness value L^* of CIELAB color space helps to avoid the problem of nonexistence of the colours with the lightness value up to 100. From the other side, this is the over–normalization of CIELAB. That can caused an inconvenience to characterization of colour of glossy surfaces.

7 UNCERTAINTY OF COLOUR MEASUREMENTS

7.1 Propagation of the Uncertainty

The full description of uncertainty propagation can be found in ISO Guide to the Expression of Uncertainty in Measurements (GUM) [47] and also in [85–90]. The variance of the uncertainty is formed by combining the measured uncertainty of every component through their relationship

$$u^2(X) = \sum_{i=1}^{N} \left(\frac{\partial f}{\partial x_i} \right)^2 \cdot u^2(x_i) + 2 \cdot \sum_{i=1}^{N-1} \sum_{j=i+1}^{N} \frac{\partial f}{\partial x_i} \cdot \frac{\partial f}{\partial x_j} \cdot u(x_i, x_j) \tag{7.1}$$

where f is a function of the measured values of the quantity X with $X = f(x_1, x_2, \ldots x_N)$; N is the number of independent variables; $u(x_i)$ is the uncertainty of the variable x_i x_i; $u(x_i, x_j)$ is the covariance of component x_i and x_j. $\frac{\partial f}{\partial x_i}$ and $\frac{\partial f}{\partial x_j}$ are the weigthing coefficients (sensitivity coefficients) for the dependence of X on various measured quantities x_i and x_j.

For the determination of colour, the spectral radiance factor is measured, which are similar variables x_i. These variables were described in **Chapter 4**. The uncertainties of the input values compose of random and systematic components. The random components are usually independent. These components are combined into a total uncertainty for the variable x_i. But the values are partly correlated at different wavelengths. These values can be described in terms of the correlation coefficient (r)

$$u(x_i, x_j) = r \cdot u(x_i) u(x_j) \tag{7.2}$$

where r ranges from -1 to +1. $u(x_i)$ and $u(x_j)$ are the uncertainties of variables x_i and x_j.

If r is equal to zero, the variables are uncorrelated. If $|r| = 1$ the variables are fully

correlated. Equation (7.1) can be written as follows

$$u^2(X) = \sum_{i=1}^{N} \left(\frac{\partial f}{\partial x_i} \right)^2 \cdot u^2(x_i) + 2 \cdot \sum_{i=1}^{N-1} \sum_{j=i+1}^{N} \frac{\partial f}{\partial x_i} \cdot \frac{\partial f}{\partial x_j} \cdot r(x_i, x_j) \cdot u(x_i) u(x_j) \qquad (7.3)$$

If we have two quantities X and Y, the covariance between two combinations $(u(X, Y))$ of the same quantities is presented as follows

$$u(X, Y) = \sum_{i=1}^{N} \sum_{j=1}^{N} \frac{\partial f}{\partial x_i} \cdot \frac{\partial f}{\partial x_j} \cdot u(x_i, x_j) \qquad (7.4)$$

The variance of the quantity is its covariance with itself $u^2(x_i) \equiv u(x_i, x_i)$. The equation (7.1) can be presented in the following form

$$u^2(X) = f_x U_x f_x^T \qquad (7.5)$$

where the f_x is the vector of sensitivity coefficients of every components in the quantity X and $f_x = \left(\frac{\partial f}{\partial x_1} \frac{\partial f}{\partial x_2} \cdots \frac{\partial f}{\partial x_n} \right)$; f_x^T is the transposed vector of sensitively coefficients; $U_x = (u(x_i, x_j))$ is the variance–covariance matrix of square–of–uncertainty with the size $N \times N$. The diagonal elements of this matrix is the variance of the quantity.
For two combinations X and Y

$$u(X, Y) = f_x U_x g_x^T \qquad (7.6)$$

where g_x is:

$$g_x = \left(\frac{\partial g}{\partial x_1} \frac{\partial g}{\partial x_2} \cdots \frac{\partial g}{\partial x_n} \right) \qquad (7.7)$$

Here a set of input values X is combined with output values Y. The variance–covariance matrix for output quantities U_y is coming from input quantities U_x. The matrix form of equation (7.3) is

$$U_y = Q U_x Q^T \qquad (7.8)$$

where Q is the row sensitivity coefficient matrix for the output quantities in terms of each of the input quantities.

7.2 Variance and Covariance Tristimulus Value

The variance of the tristimulus value X is described by equation 7.1. If we suppose that the reflectance has uncorrelated uncertainty components, the second part of equation 7.1

is equal to 0. So equation (7.1) can be rewritten in the following form

$$\sum_{i=1}^{N-1} \sum_{j=i+1}^{N} \frac{\partial f}{\partial x_i} \cdot \frac{\partial f}{\partial x_j} \cdot u(x_i, x_j) = 0$$

In this case the variance of the uncertainty of values X is

$$u^2(X) = \sum_{i=1}^{N} \left(\Delta_i S_i \overline{x}_i\right)^2 \cdot u^2(R_i)) \tag{7.9}$$

The same equations can be scripted for Y and Z.
The covariance between X and Y tristimulus value $u(X, Y)$ follows from equation (7.4)

$$u(X, Y) = \sum_{i=1}^{N} \Delta_i^2 S_i^2 \overline{x}_i \overline{y}_i \cdot u^2(R_i) \tag{7.10}$$

The equations for the covariances $u(X, Y)$ and $u(Y, Z)$ are similar. Tristimulus values are fully correlated for fully correlated components of the spectral measurements. The other colour values are calculated from the tristimulus values.

7.2.1 Matrix for the Variation and Covariation of Colour Values

The uncertainty of colour data is directly propagated from the uncertainty of the reflectance measurements [91–94]. The variance–covariance matrix U_{XYZ} for tristimulus values X, Y and Z is

$$U_{XYZ} = \begin{bmatrix} u^2(X) & u(X,Y) & u(X,Z) \\ u(X,Y) & u^2(Y) & u(Y,Z) \\ u(X,Z) & u(Y,Z) & u^2(Z) \end{bmatrix} \tag{7.11}$$

For any three colour values (a, b, c) the variance–covariance matrix is computed as

$$U_{XYZ} = Q_{abc} U_{XYZ} Q_{abc}^T \tag{7.12}$$

where Q_{abc} is the sensitivity coefficient matrix, which is calculated as

$$Q_{abc} = \begin{bmatrix} \frac{\partial a}{\partial X} & \frac{\partial a}{\partial Y} & \frac{\partial a}{\partial Z} \\ \frac{\partial b}{\partial X} & \frac{\partial b}{\partial Y} & \frac{\partial b}{\partial Z} \\ \frac{\partial a}{\partial X} & \frac{\partial c}{\partial Y} & \frac{\partial c}{\partial Z} \end{bmatrix} \tag{7.13}$$

7.3 Sensitivity Coefficient of Tristimulus Value

The calculation of tristimulus values are presented in **Section 2.4**. Integrals in equation 2.8 and 2.9 can be replaced by sums, while the colour–matching function was also measured at the discrete wavelengths in the $V(\lambda)$–range (from 360 nm to 780 nm). The integrals in equation 2.8 can be replaced by the sums

$$X = \sum_{i=1}^{N} \Delta_i S_i R_i \overline{x}_i$$

$$Y = \sum_{i=1}^{N} \Delta_i S_i R_i \overline{y}_i \tag{7.14}$$

$$Z = \sum_{i=1}^{N} \Delta_i S_i R_i \overline{z}_i$$

where the subscript i denotes the wavelength. For instance, the data are measured at equally spaced interval ($\Delta\lambda$), $\Delta\lambda$ is the weight term of the ith integral contribution, $\Delta_i = \Delta\lambda$ and is constant. Δ_i varies through the spectrum.

$$\begin{aligned} \Delta_1 &= \frac{(\lambda_2 - \lambda_1)}{2} \\ \Delta_N &= \frac{(\lambda_N - \lambda_{N-1})}{2} \\ \Delta_i &= \frac{(\lambda_{i+1} - \lambda_{i-1})}{2} \qquad i \neq 1 \, or \, N \end{aligned} \tag{7.15}$$

The colour–matching functions are tabulated values. They do not carry uncertainty. The sensitivity coefficients are depended on the spectral reflective values. They can be derived

from the equation 7.14

$$\frac{\partial X}{\partial R_i} = \Delta_i S_i \overline{x}_i$$

$$\frac{\partial Y}{\partial R_i} = \Delta_i S_i \overline{y}_i \tag{7.16}$$

$$\frac{\partial Z}{\partial R_i} = \Delta_i S_i \overline{z}_i$$

7.3.1 Sensitivity Matrix for (x, y, Y) Colour Coordinates

x,y are the chromaticity values (see equation 2.10). The sensitivity coefficients matrix for (x,y,Y) colour coordinates can be computed as

$$Q_{xyY} = \begin{bmatrix} \frac{Y+Z}{(X+Y+Z)^2} & \frac{-X}{(X+Y+Z)^2} & \frac{-X}{(X+Y+Z)^2} \\ \frac{-Y}{(X+Y+Z)^2} & \frac{X+Z}{(X+Y+Z)^2} & \frac{-Y}{(X+Y+Z)^2} \\ 0 & 1 & 0 \end{bmatrix} \tag{7.17}$$

7.3.2 Sensitivity Matrix for CIELAB

(L^*,a^*,b^*) colour coordinates are computed from equation 2.12. Since X_n, Y_n, Z_n are the white object colour stimulus of the PRD (see **Section 2.5**), they do not carry uncertainty. The sensitivities coefficient matrix is

$$Q_{L^*a^*b^*} = \begin{bmatrix} 0 & \frac{116}{3} \cdot Y_n^{(\frac{-1}{3})} \cdot Y^{(\frac{-2}{3})} & 0 \\ \frac{500}{3} \cdot X_n^{(\frac{-1}{3})} \cdot X^{(\frac{-2}{3})} & \frac{-500}{3} \cdot Y_n^{(\frac{-1}{3})} \cdot Y^{(\frac{-2}{3})} & 0 \\ 0 & \frac{200}{3} \cdot Y_n^{(\frac{-1}{3})} \cdot Y^{(\frac{-2}{3})} & \frac{-200}{3} \cdot Z_n^{(\frac{-1}{3})} \cdot Z^{(\frac{-2}{3})} \end{bmatrix} \tag{7.18}$$

7.4 Uncertainty of Colour Coordinates of Ceramic Matt Tiles

The spectral radiance factor was measured in a geometry of 45°:0°. The measurement was realized by the absolute method, described in **Chapter 4**. Uncertainties of the spectral radiance factor value are also presented in **Section 4.3**. The colour values are

computed from the spectral radiance factor measurements. The measurements of the colour data were realized with the ARGon^3 in CCD–configuration. Using the example of radiance factor measurement uncertainty presented in **Section 4.3**, the complements of colour value uncertainty of red, green and blue ceramic tiles are presented in Table 7.1. Uncertainties in surface colour quantities can be defined by a definition of the propagation of every uncertainty components of its spectral radiance factor. At first, one has to be assigned random and systematic components to the spectral radiance factor uncertainty. After, it is possible to calculate the variances and covariances of tristimulus values.

Table 7.1: The components of surface colour value uncertainty

Name	Description of uncertainty component
Surface components	They propagated to each measured spectral radiance factor value and holds the contribution of each component to the X, Y, Z tristimulus uncertainties and to their covariance.
CIE	The uncertainty components of the CIE colour–matching functions and illuminants, on a 1 nm grid.
Sensitivity coefficients	Sensitivity coefficients for the tristimulus values versus spectral radiance factor. These are a convolution of the illuminant and colour–matching function distributions.
Sensitivity Matrices	3×3 matrices of the sensitivity coefficients of the colour values versus tristimulus values, the intermediate matrix products and the total variance-covariance matrices for the various colour triplets.
xyY components, L*a*b* components	These calculate the uncertainties in the colour values for each uncertainty component.

Uncertainty components of Table 7.1 were propagated to the measurements of red, green and blue ceramic tiles. The calculations of colour data triplets and colour uncertainties are presented for D65 Illuminant, 10° colour–matching functions and for the illumination/observation geometry at 45°:0°. The results of the colour values calculation and uncertainty of colour value measurements are shown in Table 7.2. The calculation of uncertainties of colour coordinates was done with MatLab for two colour spaces (x,y,Y) and CIELAB. The uncertainty of colour coordinates was done according to the above description of the uncertainty propagation.

Table 7.2: Colour value of ceramic tile with uncertainty

	Ceram18 (red)	Ceram21 (green)	Ceram24 (blue)
x	0.4554	0.2728	0.2600
$u(x)$	0.00032	0.0004	0.00018
y	0.3261	0.3919	0.2476
$u(y)$	0.00001	0.00025	0.00033
Y	17.93	25.92	7.13
$u(Y)$	0.02	0.01	0.02
L^*	49.40	57.92	32.11
$u(L^*)$	0.04	0.03	0.05
a^*	38.59	-24.34	7.17
$u(a^*)$	0.07	0.010	0.08
b^*	16.85	11.69	-18.92
$u(b^*)$	0.02	0.023	0.021

Because the tristimulus values is the integrals, the calculation of their uncertainties are simple to express. Results of integrating many systematic effects are described like a single parameter. The uncertainty of each tristimulus value is a sum of the spectral uncertainty, which are weighted to the appropriate CMF function. Moreover, the tristimulus values are fully correlated and their covariances are products of the uncertainty sums. The surface colour uncertainties can vary strongly with colour of the sample under the test.

The measurement accuracy of colour coordinates are not presented for mostly commercial devices. The manufacturer prefers to show the accuracy of colour measurement of the divices in terms of lightness difference. lightness difference does not really describe the uncertainty of colour measurements (see **Chapter 2**). The measured with ARGon^3 facility uncertainty of colour coordinates (x,y,Y) are persented in the Table 7.2. By the reason of the lack of uniformity of the colour spaces, it is not possible to present accurate colour uncertainties as values applicable over the colour space [30, 95, 96].

CONCLUSION

A new facility named 3D Appearance Robot–based Gonioreflectometer for measurements of the spectral radiance factor and bidirectional reflectance–distribution function was developed and described in this thesis. The ARGon^3 enables high precision goniometric measurements of diffuse reflecting materials within the whole hemispheric range above the surface of the sample, due to its off–axis capabilities, by using a five–axis robot. The ARGon^3 realizes an absolute method for measurements of the spectral radiance factor. The wavelength range of measurement is 350 nm to 1100 nm in the photodiode–picoamperemeter configuration and 350 nm to 780 nm in the CCD–configuration. Both facility measurement configurations were compared with the Gonioreflectometer of PTB which is used for calibration of diffuse reference reflection materials. The method of absolute goniometric measurements was also presented in this thesis.

The new measurement facility was established with the opportunity of measurements of the spectral radiance factor with a photodiode and with a CCD line–scan camera. The CCD line–scan camera allows to make the measurements in reasonably short time. Mirror optics with apertures were used to prepare the beam to reach the entrance slit of the monochromator at the required beam size. The measurements were carried out in $V(\lambda)$–range (the spectral range between 350 nm and 780 nm).

The calculation of the measurement uncertainty of the spectral radiance factor on the example of primed $BaSO_4$ sample for both configurations of the ARGon^3 facility was calculated and presented in **Chapter 4**. The expanded uncertainty of the single measurement of spectral radiance factor is 0.64% for ARGon^3 with photodiode–picoamperemeter configuration. The expanded uncertainty of single measurement of spectral radiance factor is 1.52% for ARGon^3 in CCD–configuration. Both uncertainty values were calculated for the geometry of the measurement 45°:0° and at the wavelength of 500 nm, with the coverage factor $k = 2$. The major uncertainty component by the measurements with photodiode is associated to the measurement of the reflection signal and dark from the sample. The major uncertainty component by the measurements with CCD scan–line camera is associated to optical transmission of the neutral density filter (OD3) mounted to the optical path for carrying out the dynamic range of CCD array.

The next goal of the presented work was the investigation of the non–Lambertian reflection behavior of diffuse standard reflection material. The reflection behavior of five

different materials has been studied. The investigation of the samples is presented for three wavelengths of 400 nm, 550 nm and 700 nm in the whole hemispheric range above the surface of the sample for four incident irradiation angles. That means, the every sample was measured at 0°, 22.5°, 45° and 67.5° incident angle, the reflections angle was varied from 0° to 67.5° with a step size of 7.5° and azimuth reflection angle from 0° to 180°. The step size of the azimuth angle was modified in order to provide roughly equidistance between reflection angles over quadrant of the sphere above the sample surface and in this way to realize the uniform measurement of the spectral radiance factor. The 3D–indicatrices for every reflection sample are presented.
In this thesis also the spectral radiance factor and colour coordinates of different effect pigments was investigated. It was shown that, there is a necessity for multiangular ivestigation of the effect pigments.
The uncertainty of colour coordinates measurements are presented by the example of coloured ceramic tiles for different color spaces.
The measurement uncertainties and models for the spectral radiance factor presented in this work may be still improved. Some suggestions for future work are listed in the following:

- The measurement uncertainty of the spectral radiance factor with ARGon^3 in CCD–configuration calculated here can be improved significantly by reducing the measurement uncertainty of the transmittance of the neutral density filter. Another possibility is to applied a CCD– detector with wide dynamic range and the cooling stages and shorter exposure time [10, 40]. In this way, the use of neutral density filter in the optical path could be eliminated.

- The measurement uncertainty of the spectral radiance factor measured with the ARGon^3 in both configurations can be improved by using other light source [11].

APPENDIX:

APPENDIX A: Wavelength adjustment of the line–scan camera CCD array

Table A.1: Wavelength adjustment of the CCD array with the 3rd grating of the iHR–550 monochromator

Reference wavelength, λ_r nm	Measured wavelength, λ_m nm	FWHM[1], nm	Absolute deviation, Δ_λ nm
Mercury spectrum, 3rd grating targeted at 500 nm			
365.0153	365.2121	1.143389	-0.19677
404.5563	404.6981	0.979166	-0.14177
407.627	407.8315	1.061519	-0.20447
435.8328	435.8666	1.053802	-0.03385
546.0735	546.1445	1.18897	-0.07097
576.9598	577.0582	1.36249	-0.09836
Krypton spectrum, 3rd grating of iHR–550 targeted at 700 nm			
768.5246	769.0164	2.388871	-0.49185
785.4823	785.5226	2.272003	-0.0403
805.9505	806.208	3.109667	-0.25754
810.4366	811.2632	2.092733	-0.82668
819.0057	819.1352	2.254474	-0.1295
829.8693	829.8475	2.293399	0.0218

[1]full width at half maximum

a

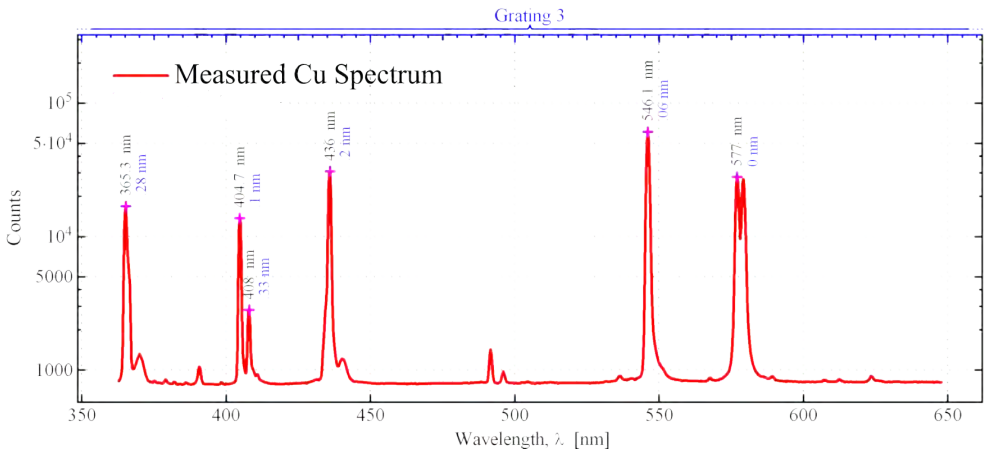

b

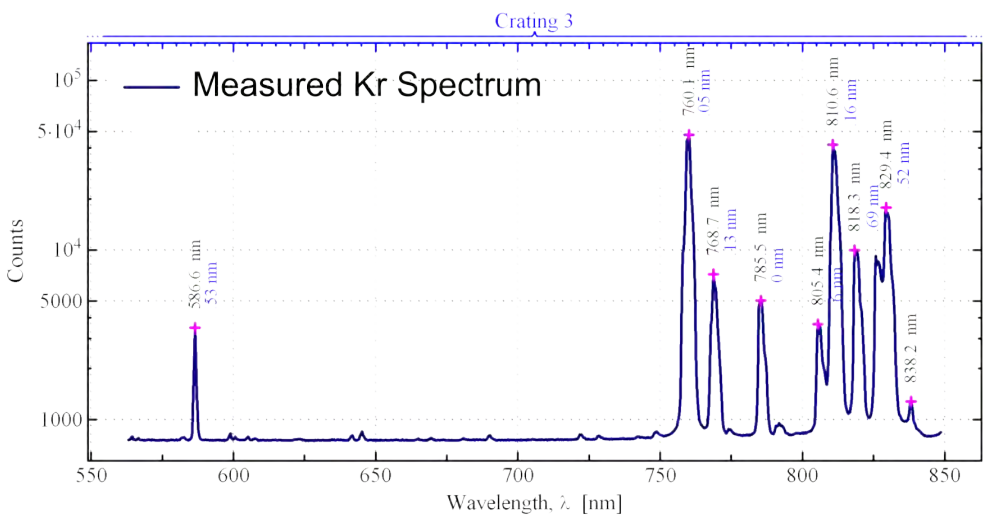

Figure A.1: Wavelength adjustment of the iHR–550 with CCD line–scan camera Hamamatsu (central targeted wavelength for 3rd grating is at: a. 500 nm and b. 700 nm)

APPENDIX B: 3D–Indikatix of Standard Reflection Materials

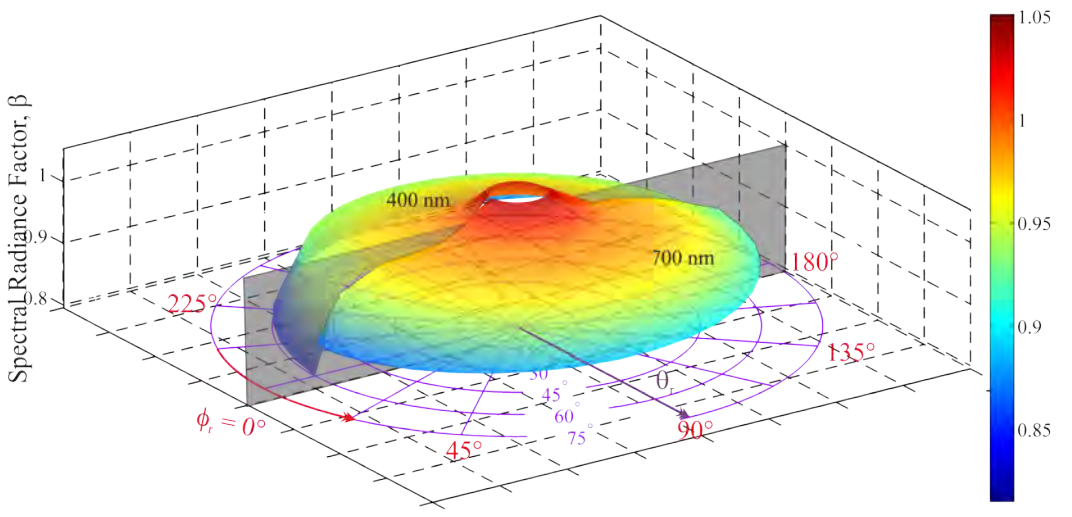

a.

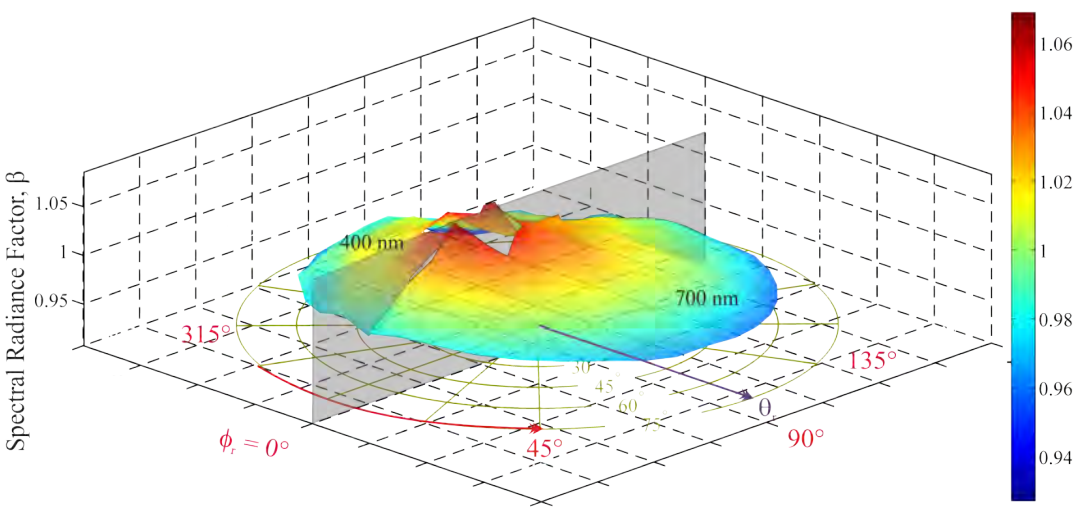

b.

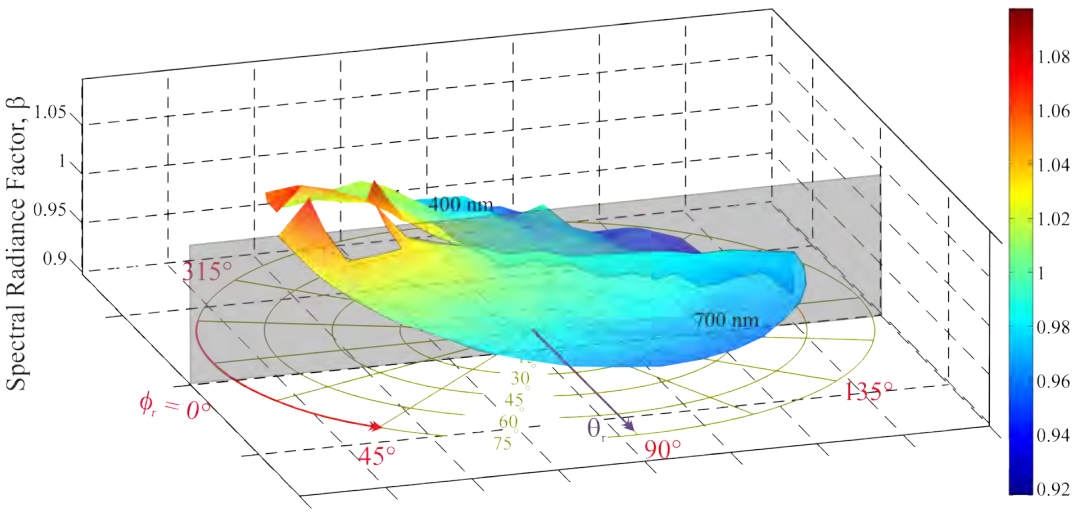

c.

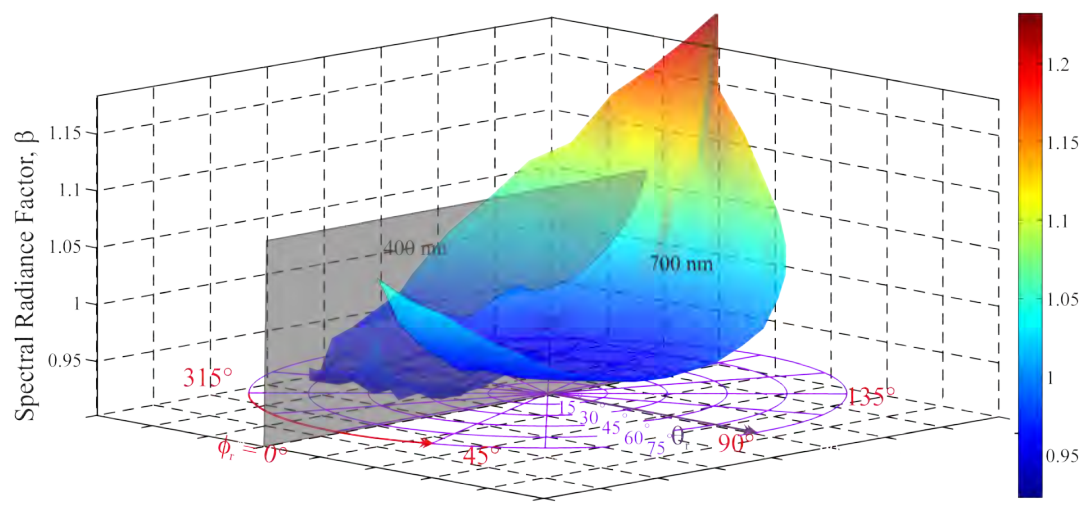

d.

Figure B.1: Three–dimensional reflection indicatrix of the standard reflection material pressed barium sulphate (A 07) for wavelengths 400 nm (left part of the surface at every plot) and 700 nm (right side of the surface at the plot) at different incident irradiation angles: a. at 0° b. at 22.5° c. at 45° and d. at 67.5°

a.

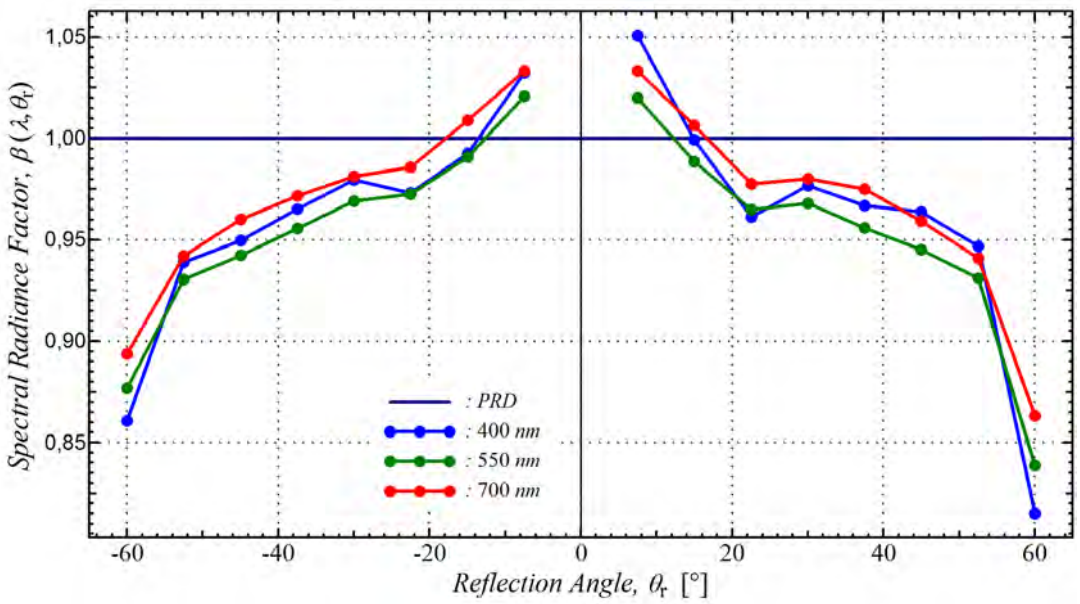
Spectral Radiance Factor, $\beta(\lambda, \theta_r)$
1,05
1,00
0,95
0,90
0,85
: PRD
: 400 nm
: 550 nm
: 700 nm
-60
-40
-20
0
20
40
60
Reflection Angle, θ_r [°]

b.

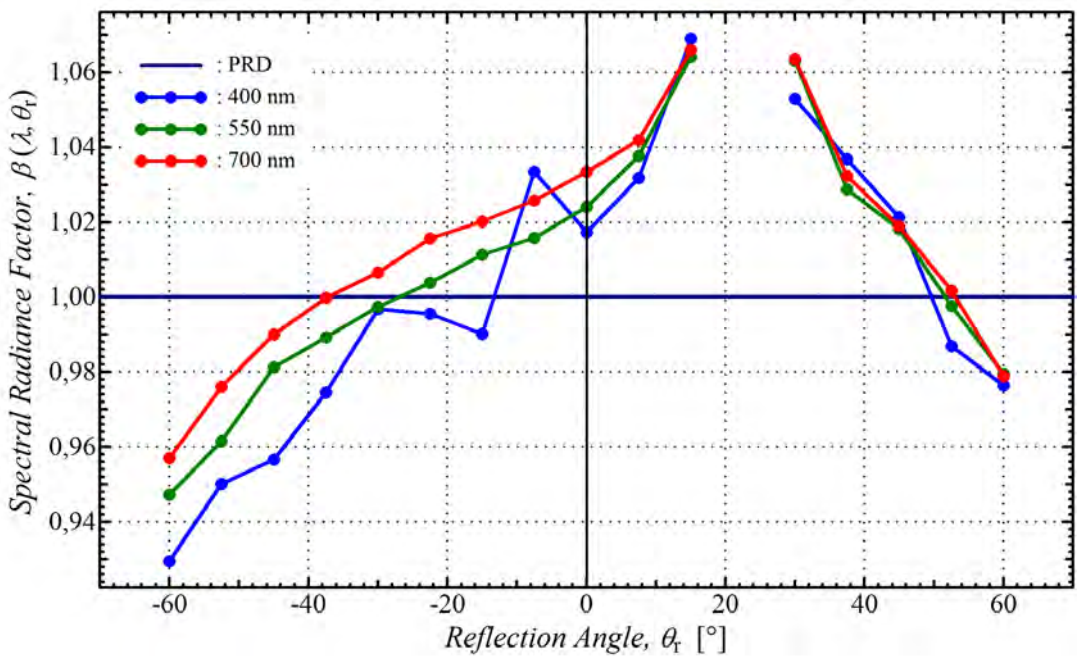
Spectral Radiance Factor, $\beta(\lambda, \theta_r)$
1,06
1,04
1,02
1,00
0,98
0,96
0,94
: PRD
: 400 nm
: 550 nm
: 700 nm
-60
-40
-20
0
20
40
60
Reflection Angle, θ_r [°]

c.

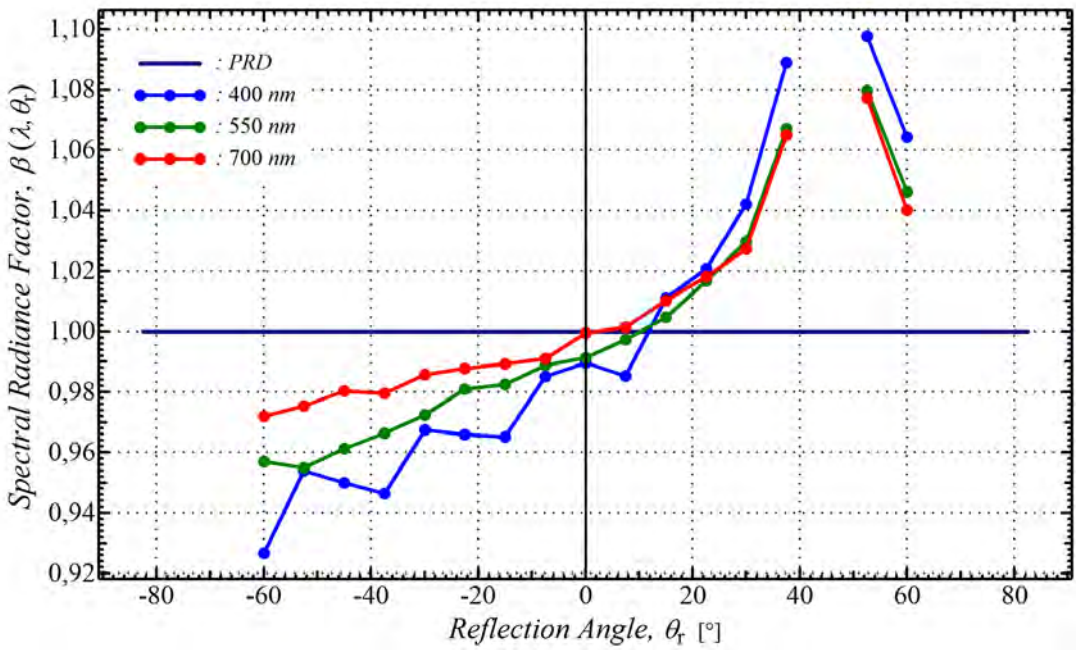

d.

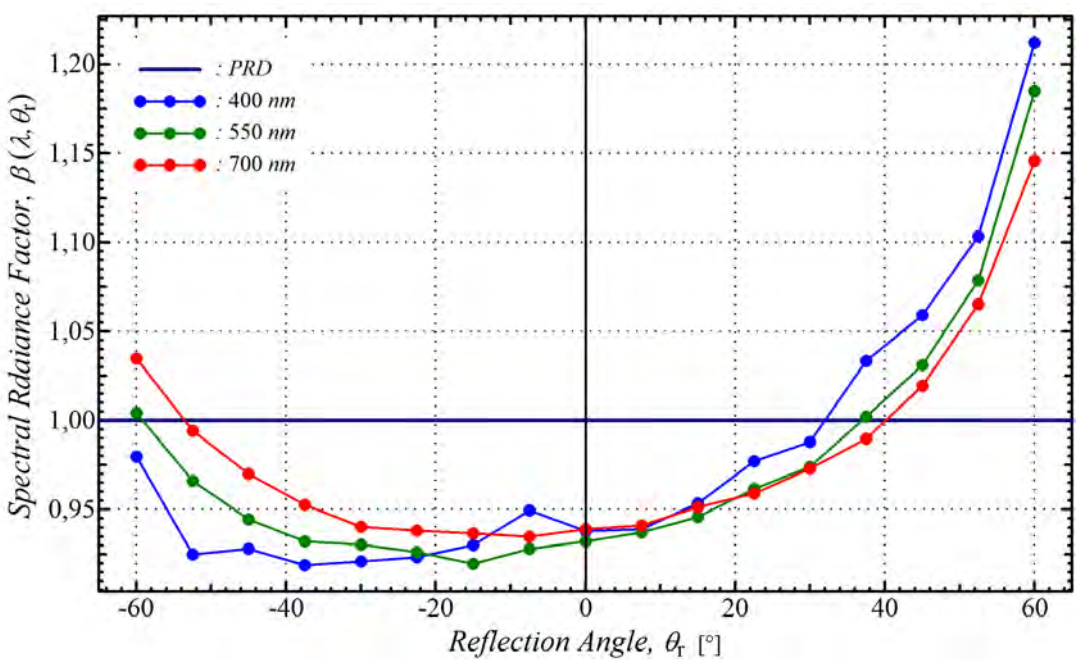

Figure B.2: The "in–plane" reflection indicatrix of the standard reflection material pressed barium sulphate (A 07) for wavelengths 400 nm, 550 nm and 700 nm at different incident irradiation angles: a. at 0° b. at 22.5° c. at 45° and d. at 67.5°

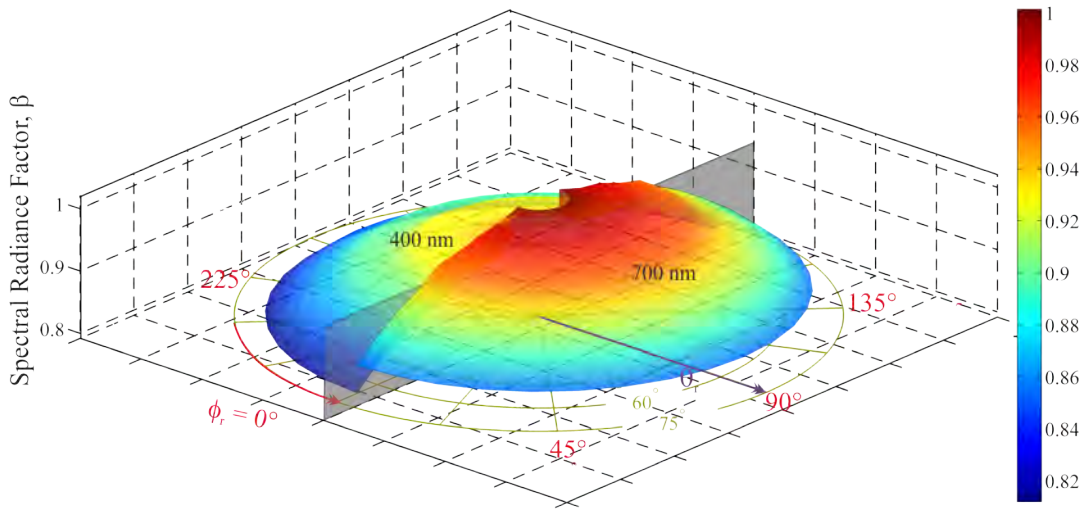
Spectral Radiance Factor, β
1
0.9
0.8
400 nm
700 nm
225°
135°
90°
45°
$\phi_r = 0°$
θ_r
60°
75°
1
0.98
0.96
0.94
0.92
0.9
0.88
0.86
0.84
0.82

a.

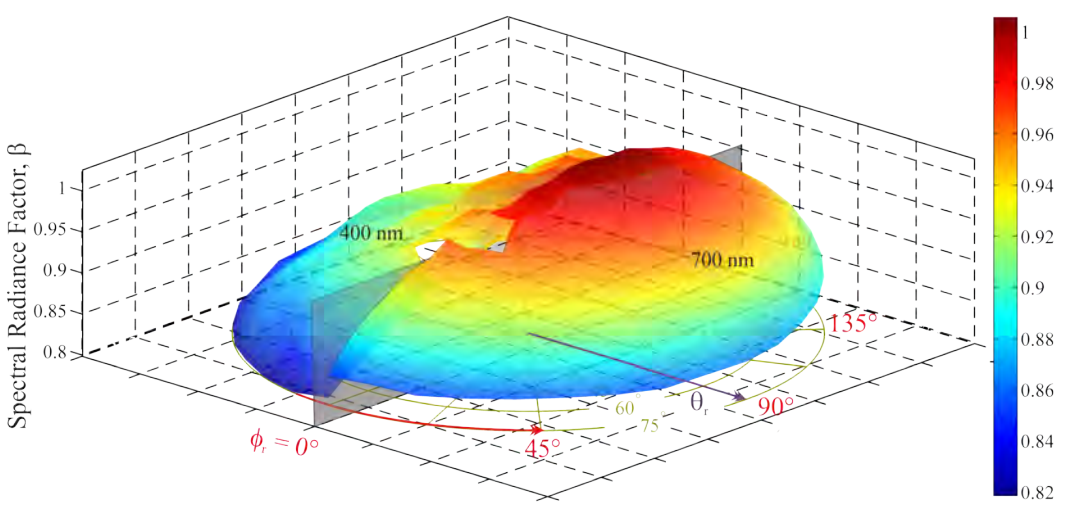
Spectral Radiance Factor, β
1
0.95
0.9
0.85
0.8
400 nm
700 nm
135°
90°
45°
$\phi_r = 0°$
θ_r
60°
75°
1
0.98
0.96
0.94
0.92
0.9
0.88
0.86
0.84
0.82

b.

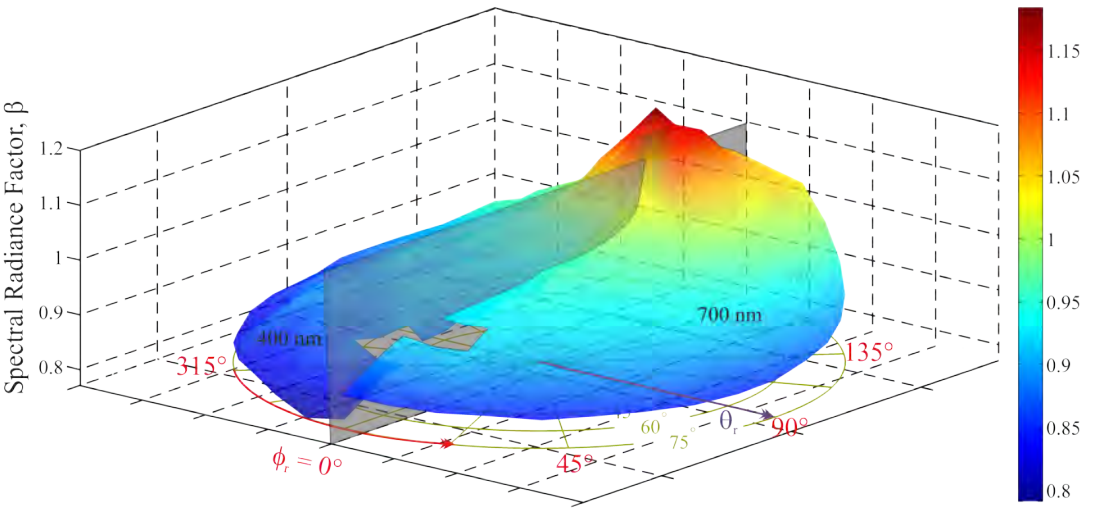

c.

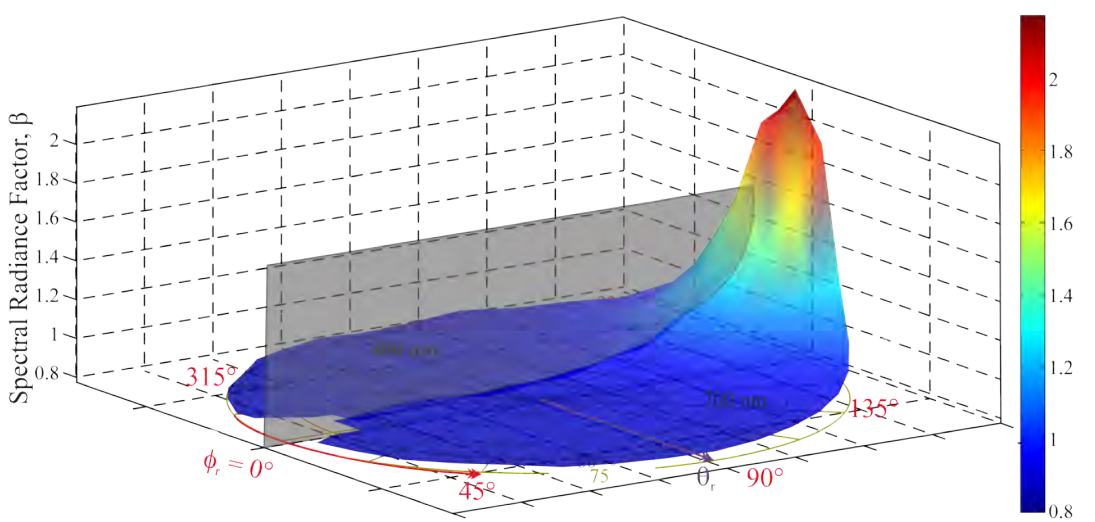

d.

Figure B.3: Three–dimensional reflection indicatrix of the standard reflection material matt opal glass (OG A 5–14–01) for wavelengths 400 nm (left part of the surface at every plot) and 700 nm (right side of the surface at the plot) at different incident irradiation angles: a. at 0° b. at 22.5° c. at 45° and d. at 67.5°

a.

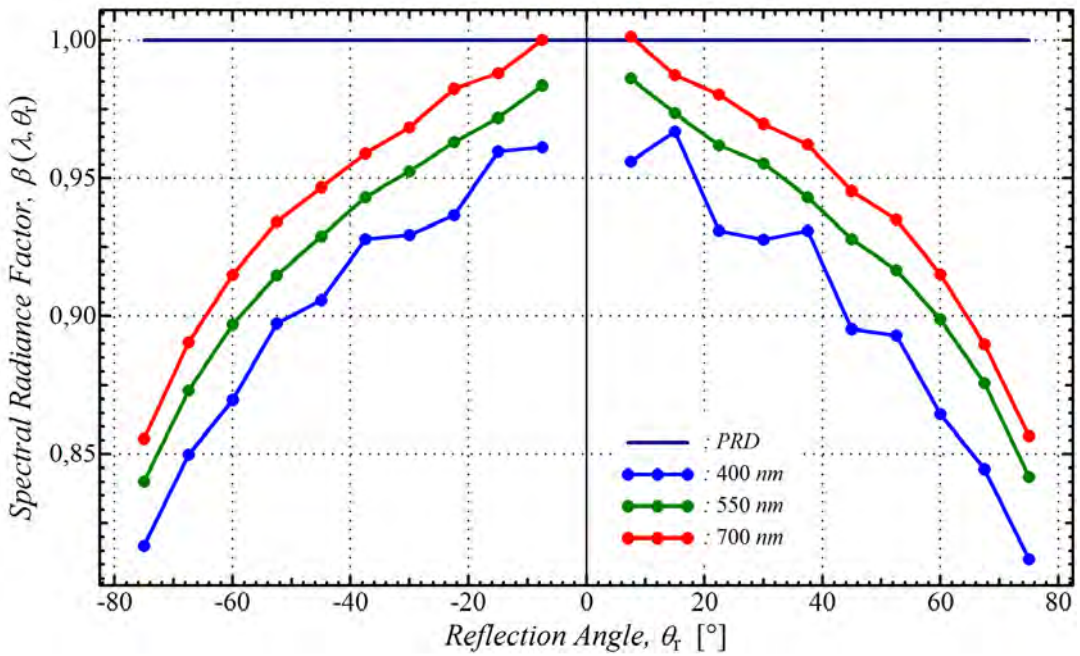
1,00
0,95
0,90
0,85
Spectral Radiance Factor, $\beta(\lambda, \theta_r)$
-80
-60
-40
-20
0
20
40
60
80
Reflection Angle, θ_r [°]
: PRD
: 400 nm
: 550 nm
: 700 nm

b.

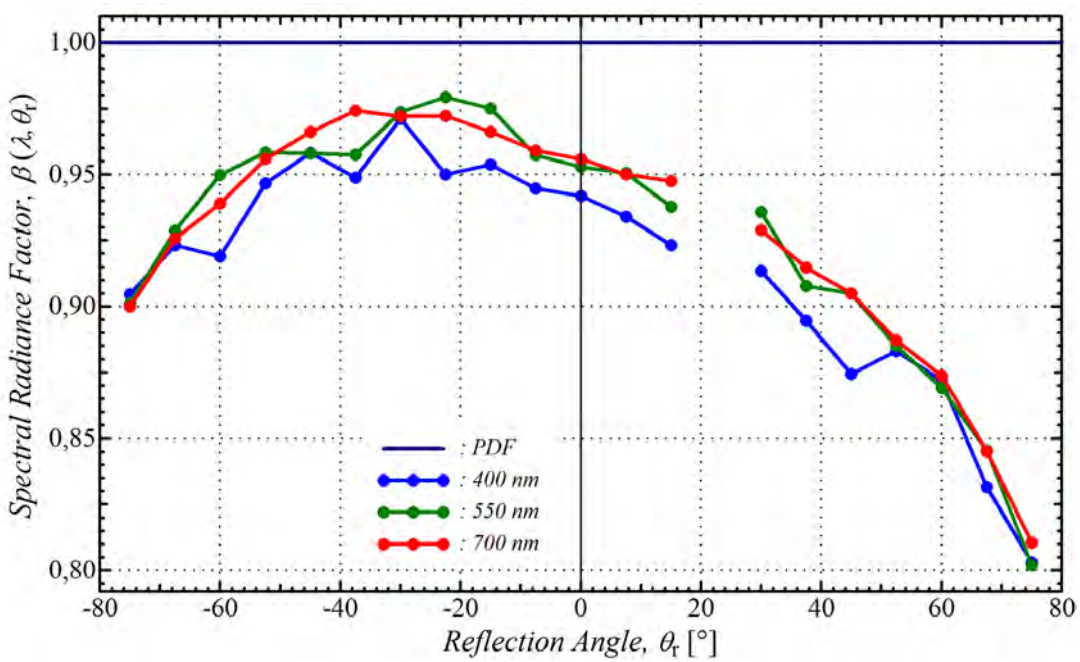
1,00
0,95
0,90
0,85
0,80
Spectral Radiance Factor, $\beta(\lambda, \theta_r)$
-80
-60
-40
-20
0
20
40
60
80
Reflection Angle, θ_r [°]
: PDF
: 400 nm
: 550 nm
: 700 nm

c.

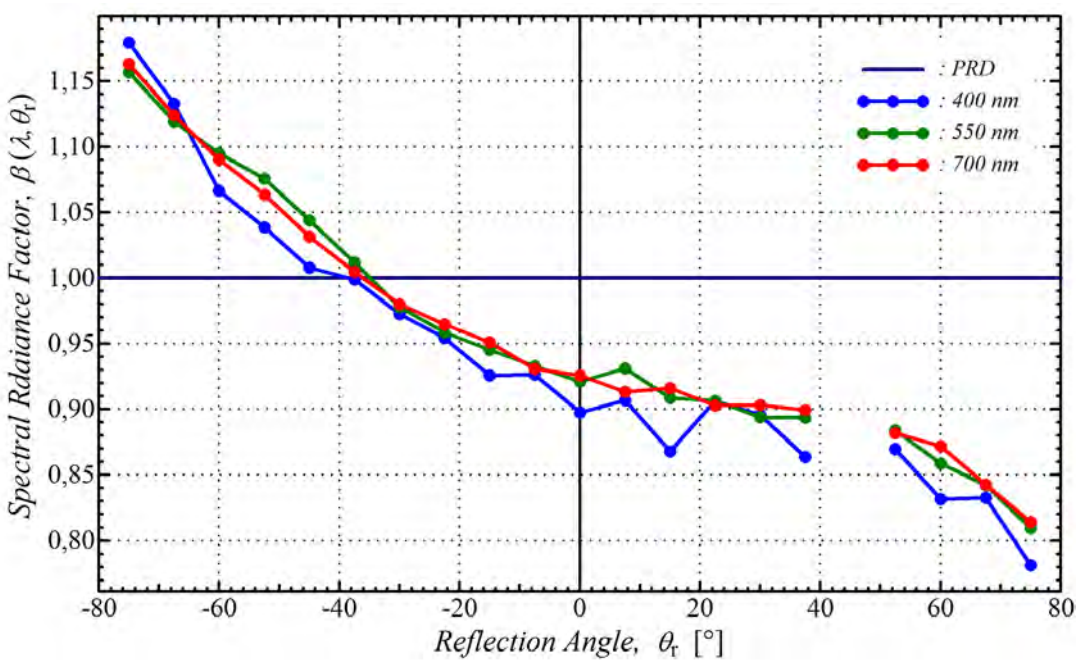

d.

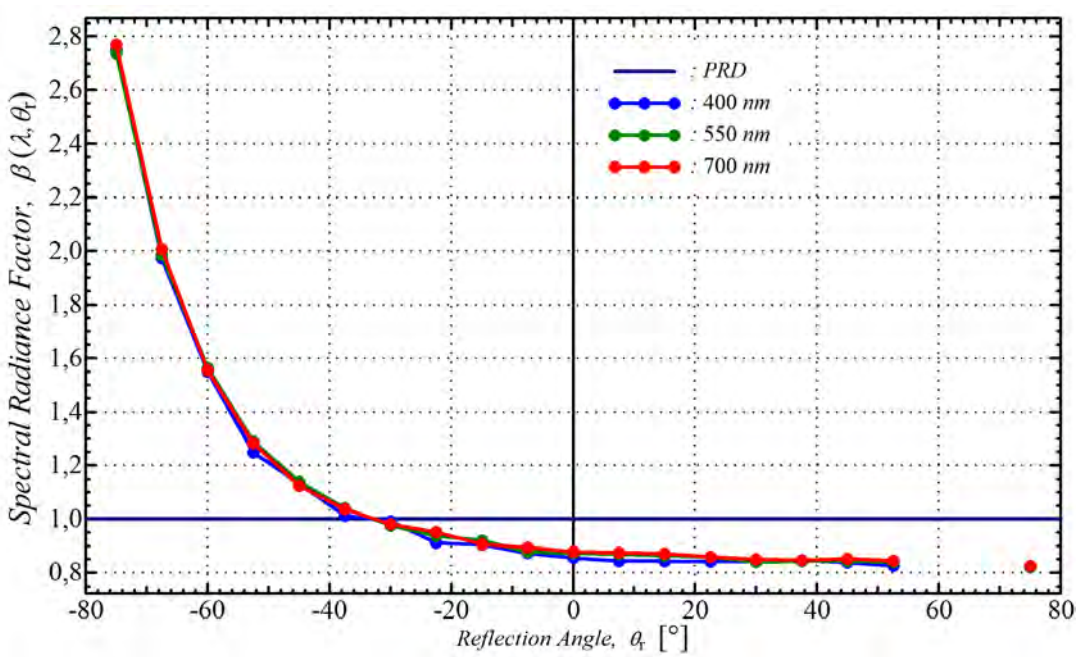

Figure B.4: The "in–plane" reflection indicatrix of the standard reflection material matt opal glass (OG A 5–14–01) for wavelengths 400 nm, 550 nm and 700 nm at different incident irradiation angles: a. at 0° b. at 22.5° c. at 45° and d. at 67.5°

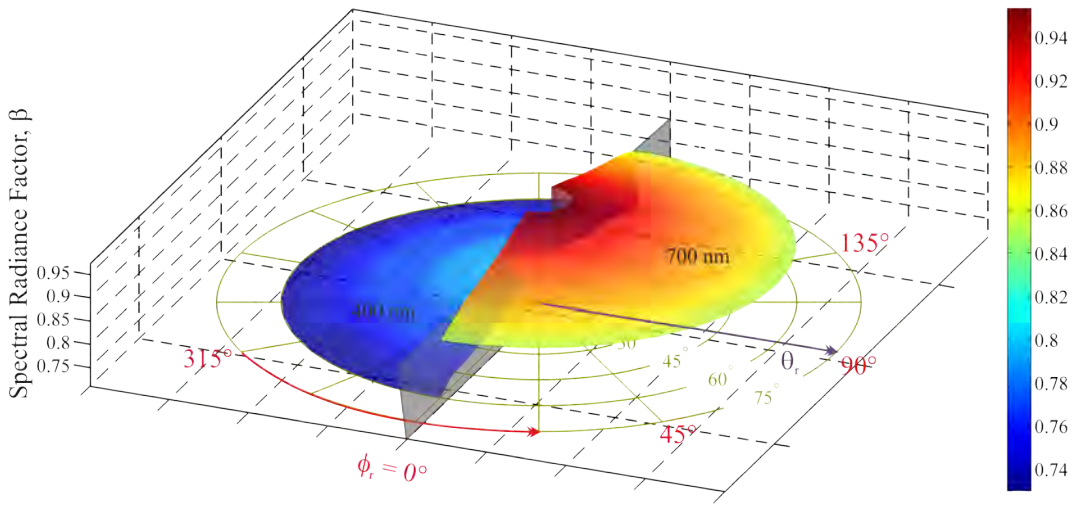
Spectral Radiance Factor, β
0.95
0.9
0.85
0.8
0.75
700 nm
400 nm
135°
315°
90°
45°
θ_r
$\phi_r = 0°$
30°
45°
60°
75°
0.94
0.92
0.9
0.88
0.86
0.84
0.82
0.8
0.78
0.76
0.74

a.

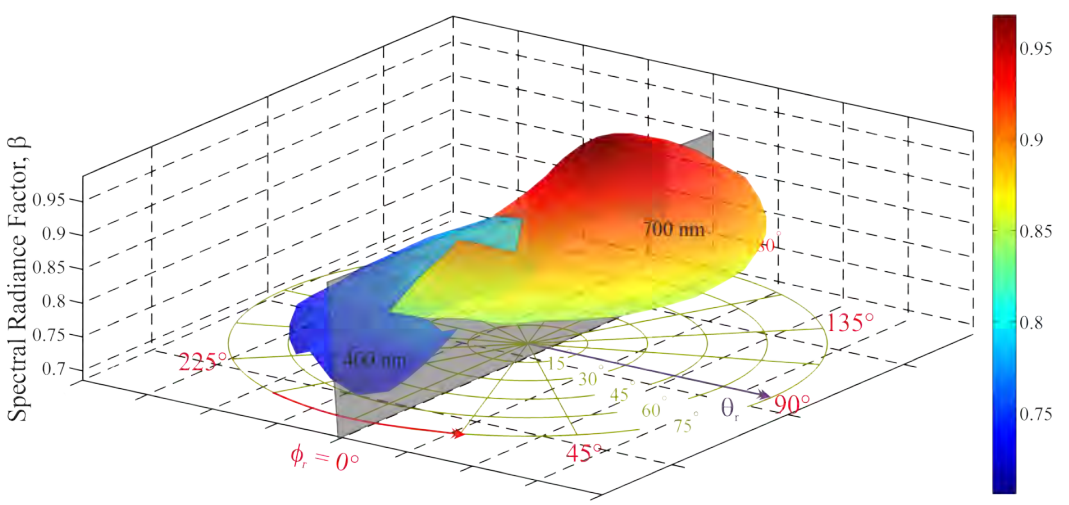
Spectral Radiance Factor, β
0.95
0.9
0.85
0.8
0.75
0.7
700 nm
400 nm
135°
225°
90°
45°
θ_r
$\phi_r = 0°$
15°
30°
45°
60°
75°
0.95
0.9
0.85
0.8
0.75

b.

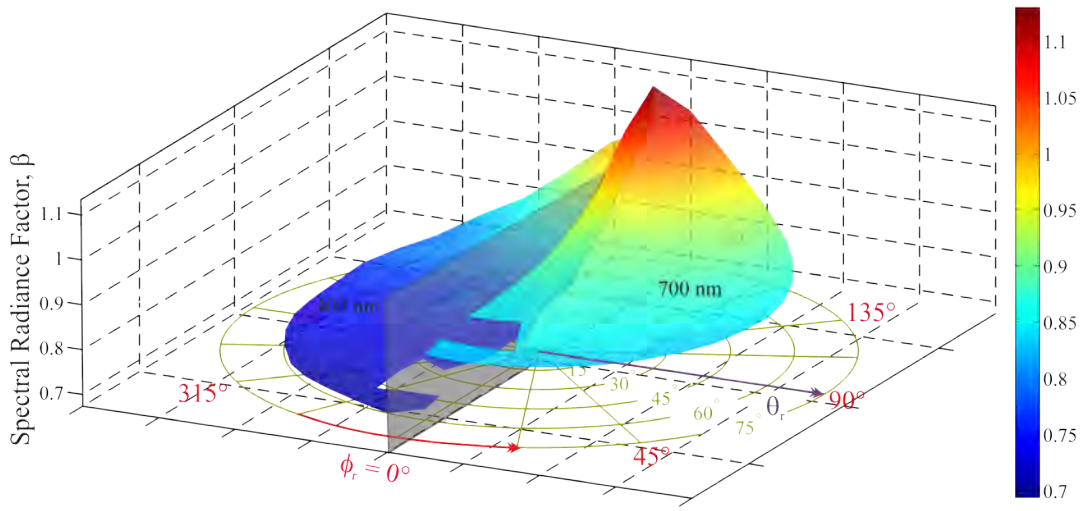

c.

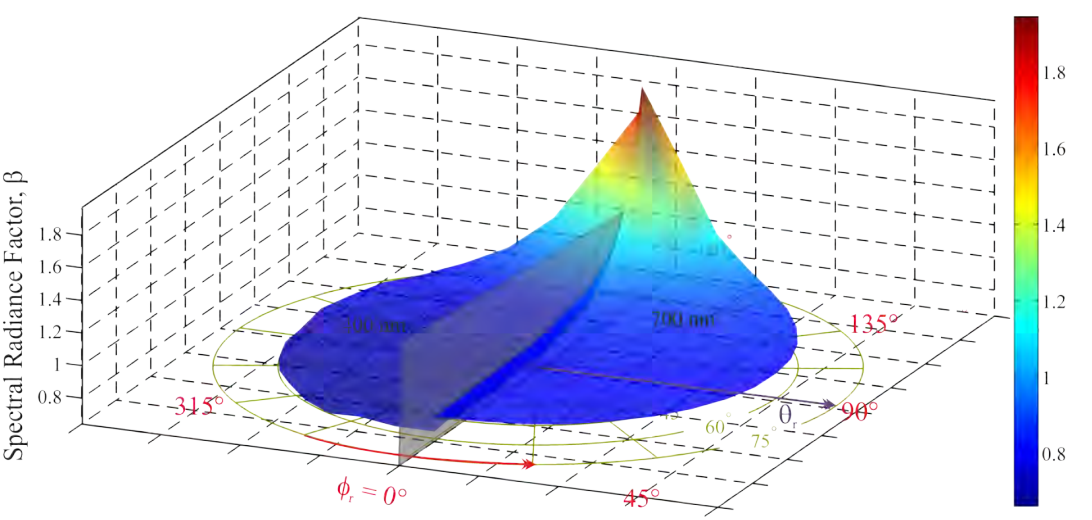

d.

Figure B.5: Three–dimensional reflection indicatrix of the standard reflection material matt ceramic title (Ceram#35) for wavelengths 400 nm (left part of the surface at every plot) and 700 nm (right side of the surface at the plot) at different incident irradiation angles: a. at 0° b. at 22.5° c. at 45° and d. at 67.5°

a.

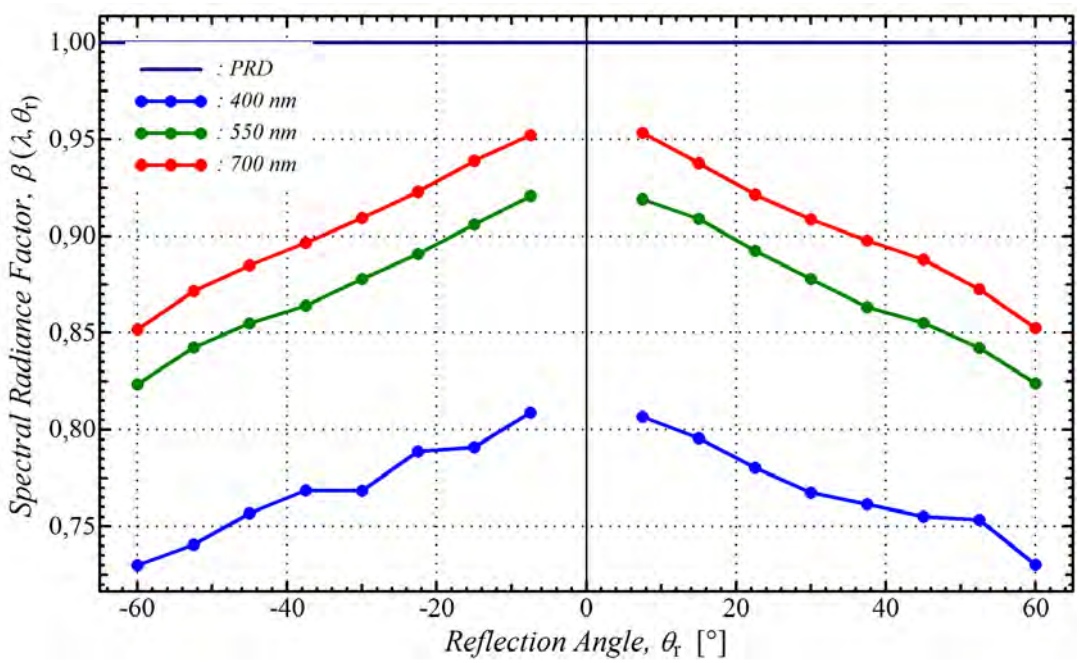
1,00
0,95
0,90
0,85
0,80
0,75
: PRD
: 400 nm
: 550 nm
: 700 nm
Spectral Radiance Factor, $\beta(\lambda, \theta_r)$
-60
-40
-20
0
20
40
60
Reflection Angle, θ_r [°]

b.

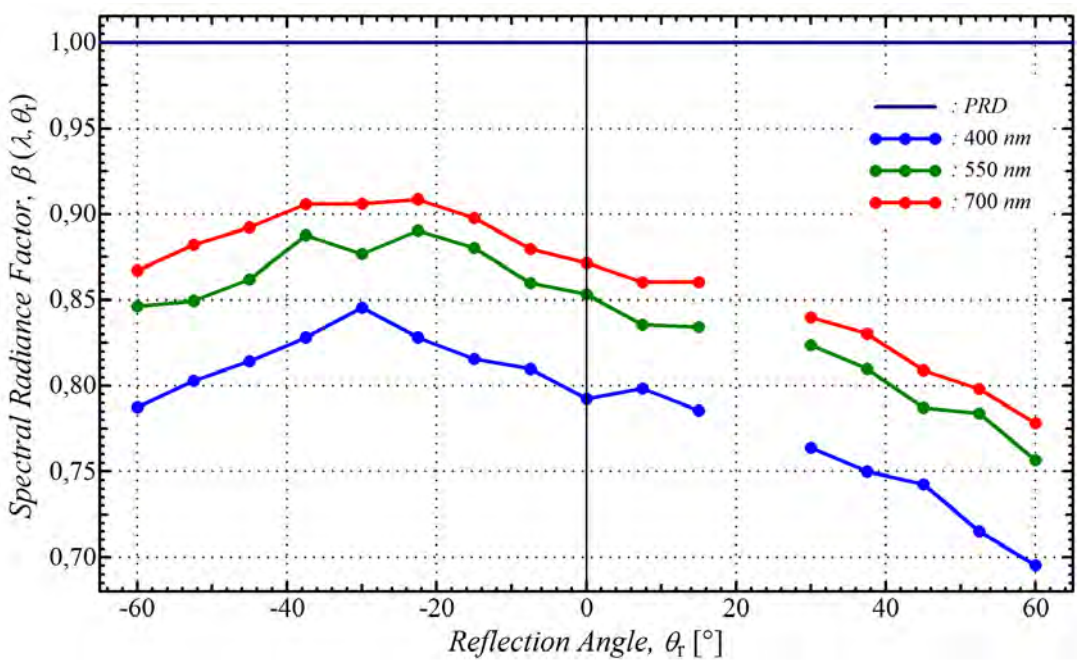
1,00
0,95
0,90
0,85
0,80
0,75
0,70
: PRD
: 400 nm
: 550 nm
: 700 nm
Spectral Radiance Factor, $\beta(\lambda, \theta_r)$
-60
-40
-20
0
20
40
60
Reflection Angle, θ_r [°]

c.

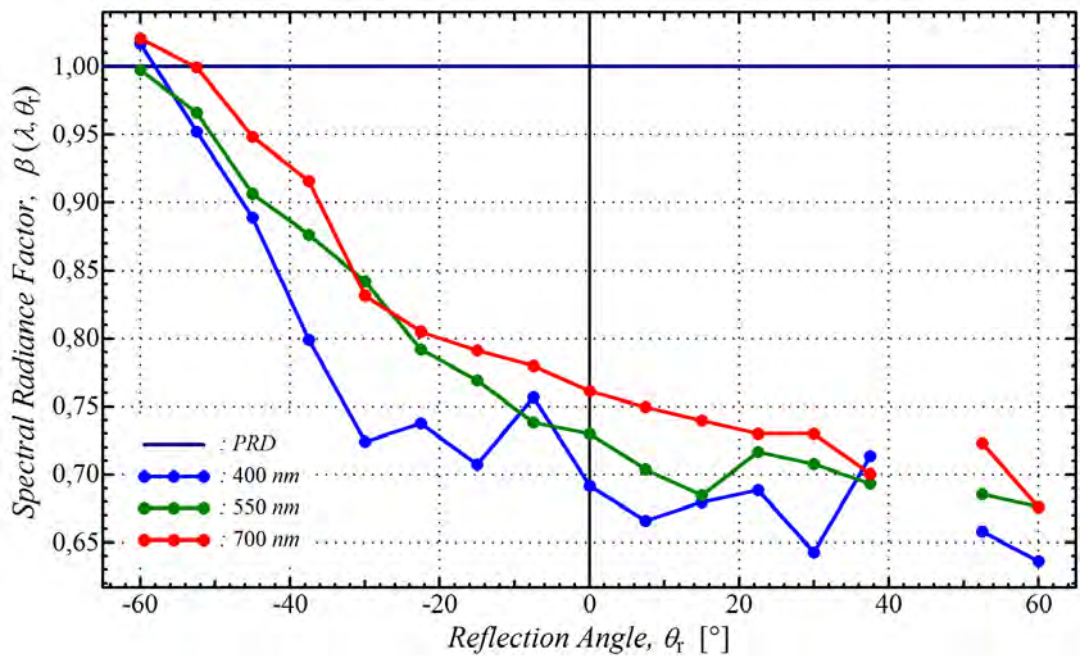

d.

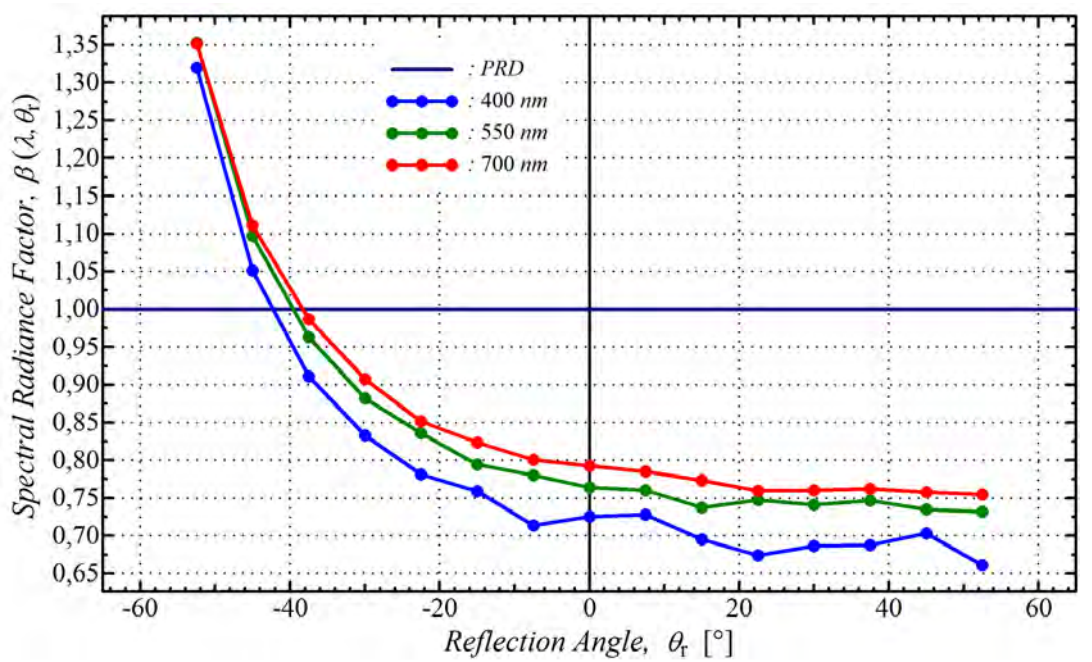

Figure B.6: The "in–plane" reflection indicatrix of the standard reflection material matt ceramic title (Ceram#35) for wavelengths 400 nm, 550 nm and 700 nm at different incident irradiation angles: a. at 0° b. at 22.5° c. at 45° and d. at 67.5°

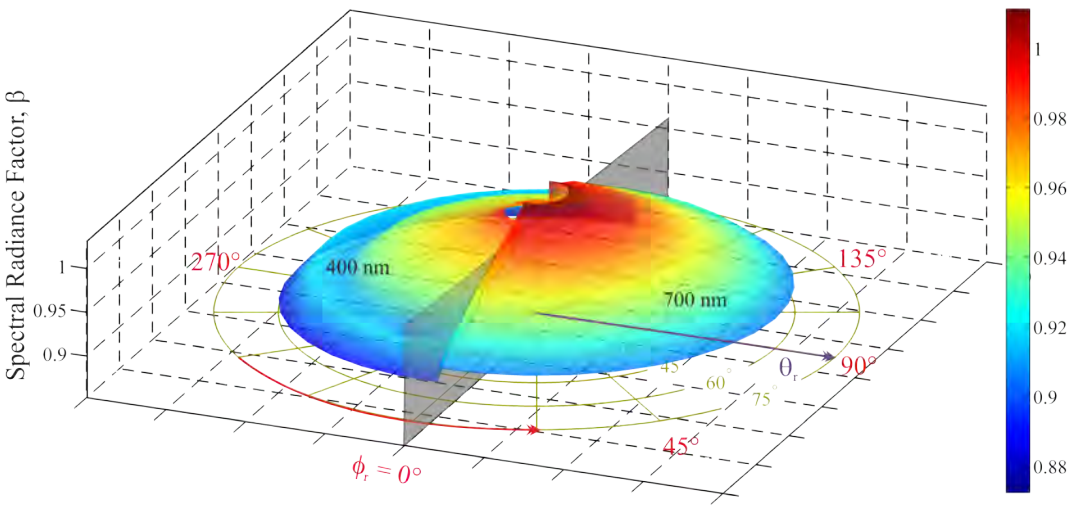
Spectral Radiance Factor, β
1
0.95
0.9
270°
400 nm
700 nm
135°
90°
θ_r
45°
60°
75°
$\phi_r = 0°$
1
0.98
0.96
0.94
0.92
0.9
0.88

a.

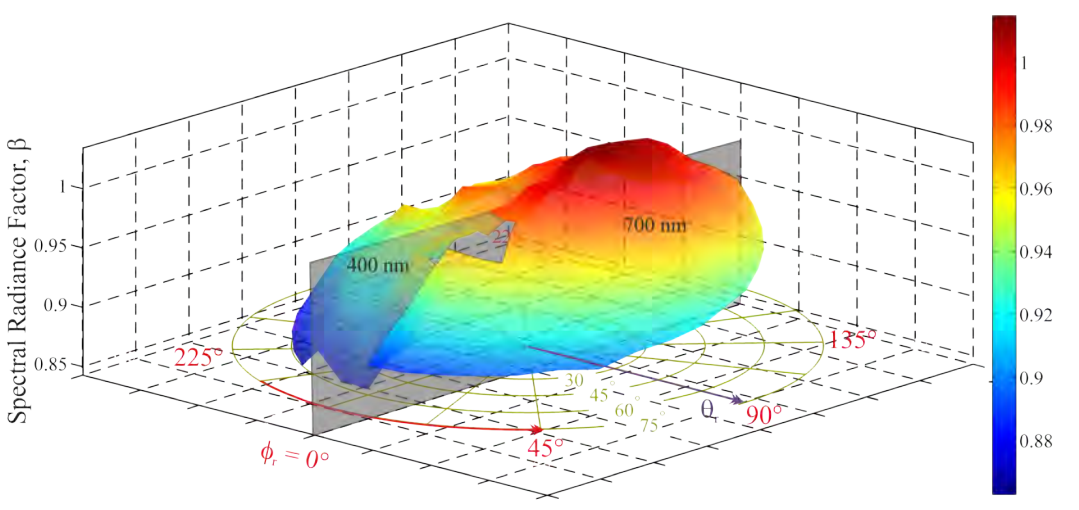
Spectral Radiance Factor, β
1
0.95
0.9
0.85
225°
400 nm
700 nm
135°
90°
θ_r
30
45
60
75
45°
$\phi_r = 0°$
1
0.98
0.96
0.94
0.92
0.9
0.88

b.

c.

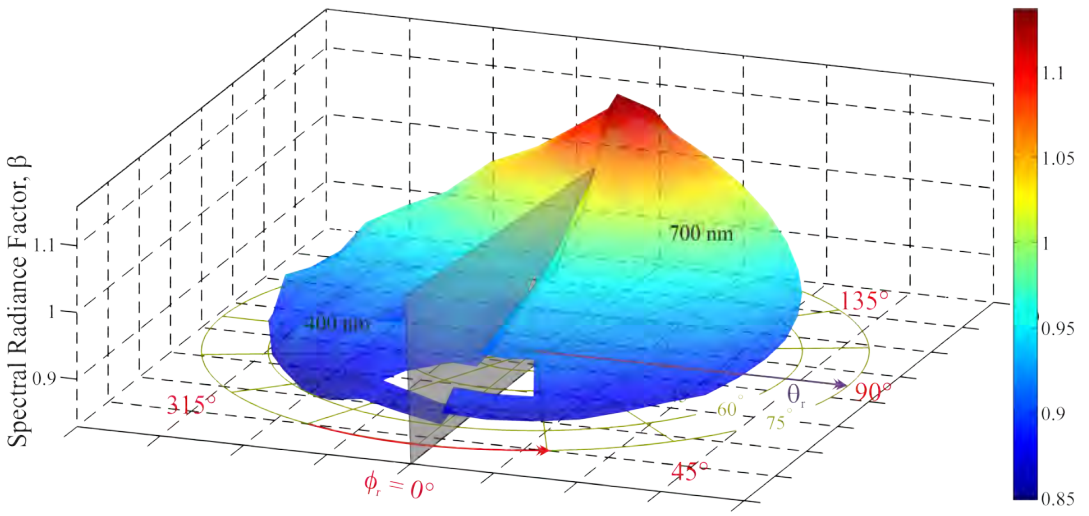

d.

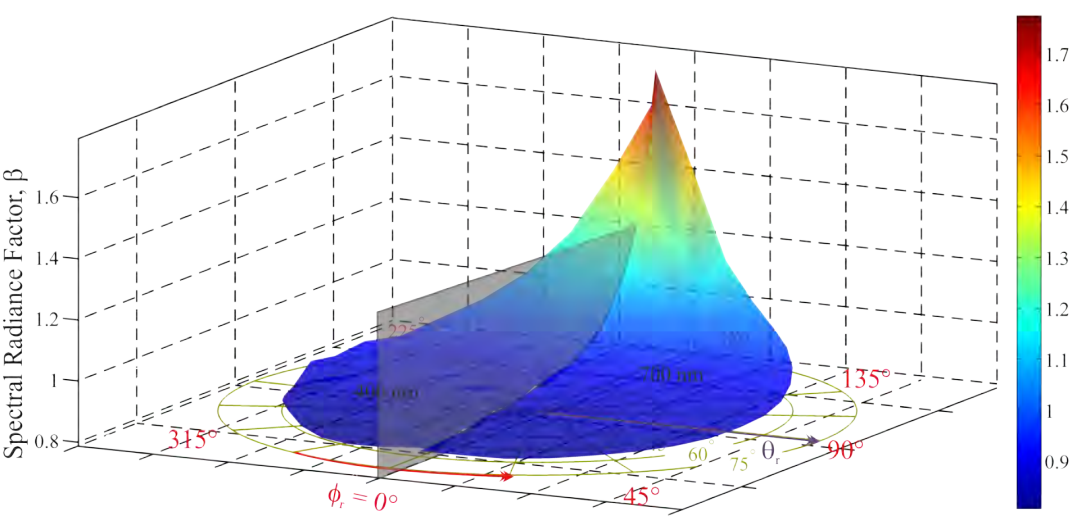

Figure B.7: Three–dimensional reflection indicatrix of the standard reflection material sintered PTFE (PTBSRS–1) for wavelengths 400 nm (left part of the surface at every plot) and 700 nm (right side of the surface at the plot) at different incident irradiation angles: a. at 0° b. at 22.5° c. at 45° and d. at 67.5°

a.

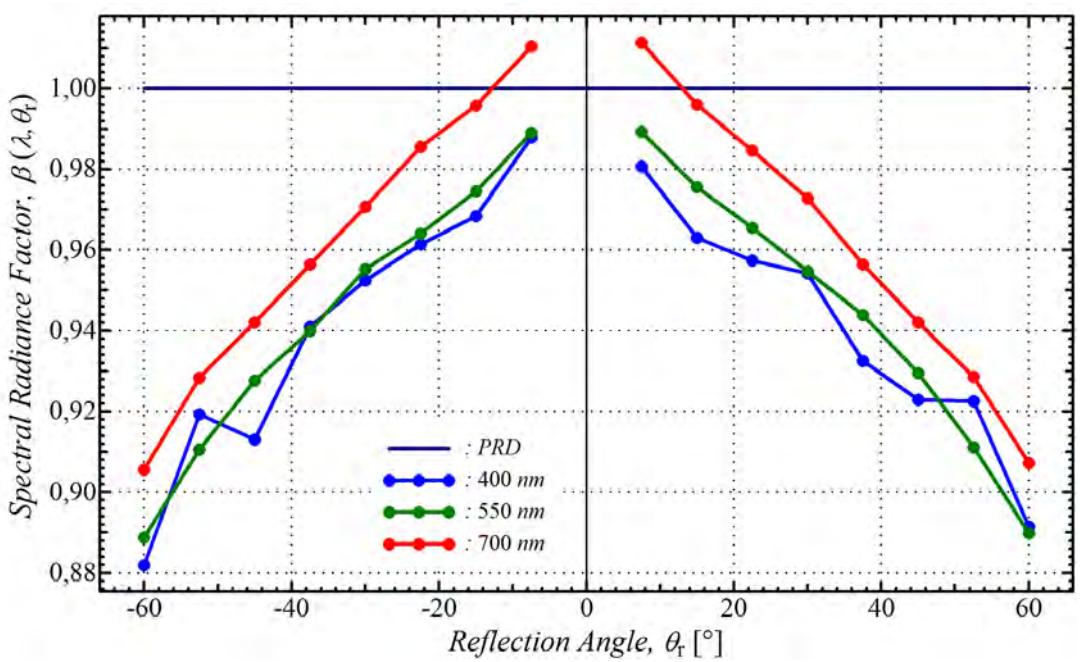
Spectral Radiance Factor, $\beta(\lambda, \theta_r)$
1,00
0,98
0,96
0,94
0,92
0,90
0,88
-60
-40
-20
0
20
40
60
Reflection Angle, θ_r [°]
: PRD
: 400 nm
: 550 nm
: 700 nm

b.

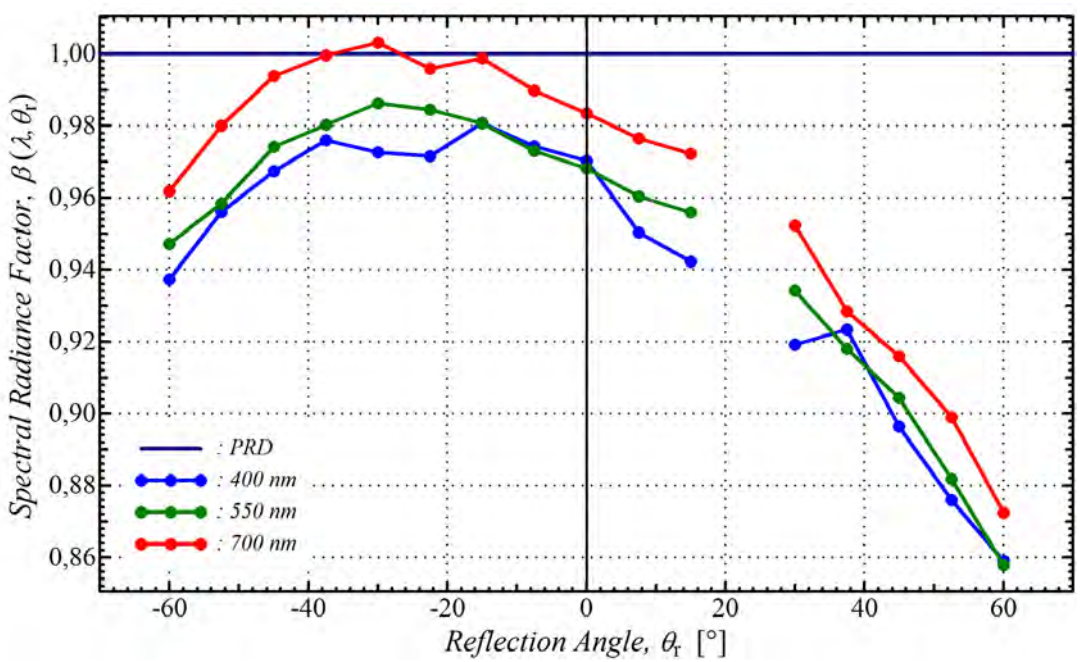
Spectral Radiance Factor, $\beta(\lambda, \theta_r)$
1,00
0,98
0,96
0,94
0,92
0,90
0,88
0,86
-60
-40
-20
0
20
40
60
Reflection Angle, θ_r [°]
: PRD
: 400 nm
: 550 nm
: 700 nm

c.

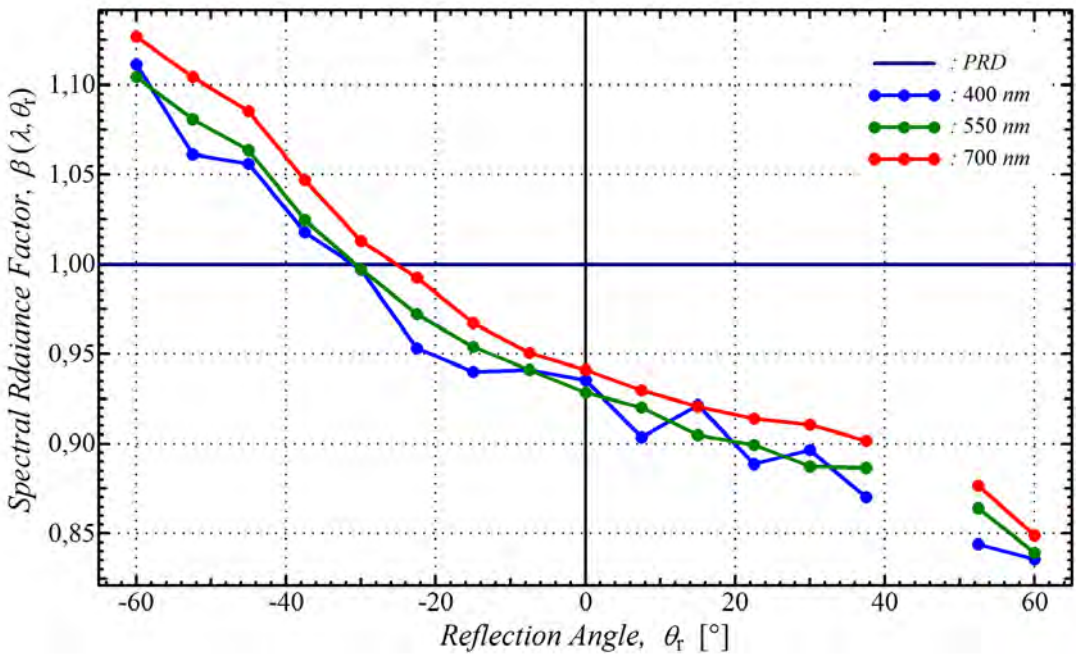

d.

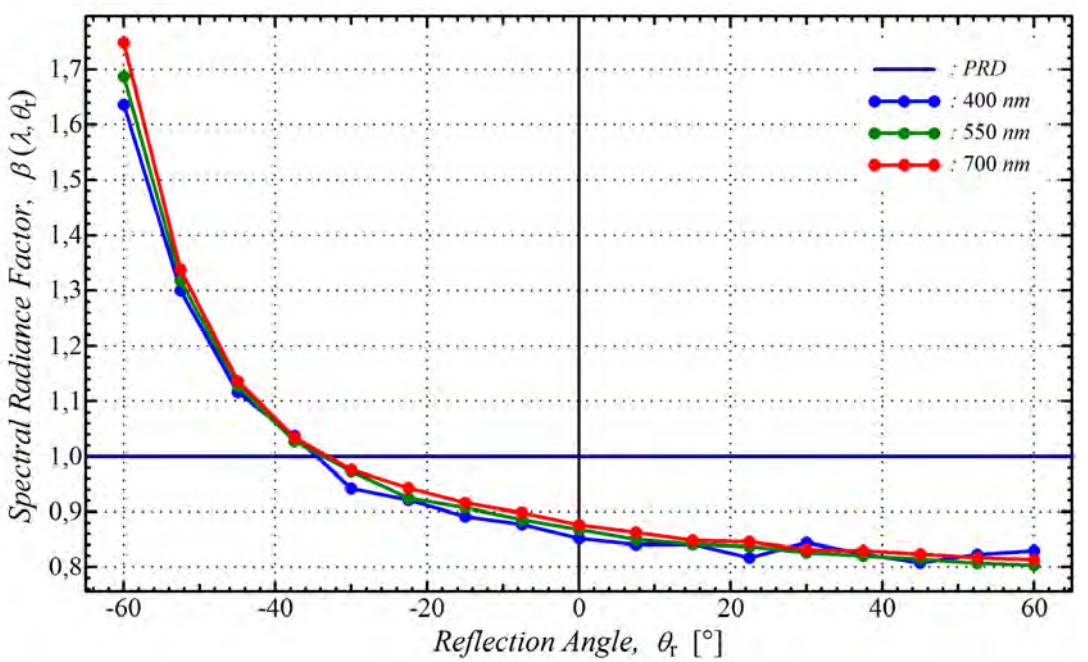

Figure B.8: The "in–plane" reflection indicatrix of the standard reflection material sintered PTFE (PTBSRS–1) for wavelengths 400 nm, 550 nm and 700 nm at different incident irradiation angles: a. at 0° b. at 22.5° c. at 45° and d. at 67.5°

REFERENCES

[1] A. Ryer. Light Measurement Handbook. International Light, February 2002.

[2] NPL. Harmonisation of national scales of surface colour measurements. report COEMS33, NPL, Luxembourg, 2000.

[3] European Commission. Intercomparison of colour measurements. Synthesis Report report EUR 14982 EN, European Commission, Luxembourg, 1993.

[4] D. C. Rich. Industrial color specifications: Reducing the uncertainty beyond the limits of absolute reflectometry. In *CORM Annual Conference*, Rochester, New York, 2000.

[5] R. W. G. Hunt. *Measuring Colour*. Ellis Horwood Ltd., Chichester, 1987.

[6] CIE. Publication 15.2 Colorimetry. Technical report, Central Bureau of the CIE, Vienna, 1986.

[7] C. DeCusatis ed. *Handbook of applied photometry*. Springer, 1998.

[8] K.J. Gåsvik. *Optical Metrology*. John Wiley and Sons, Ltd, third edition, 2002.

[9] P. Flesch. *Light and Light Sources*. Springer, 2004.

[10] T. Yoshizawa. *Handbook of optical metrology: principles and applications*. Taylor and Francis Group, LLC, 2009.

[11] R.H. Kingston. *Optical sources, detectors, and systems: fundamentals and applications*. Academic Press, 1995.

[12] G.A. Klein. *Industrial color physics*. Springer Series in optical sciences 154. Springer, 2010.

[13] IES The Lighting Autority. *The IESNA Lighting handbook*. Publications Department IESNA, ninth edition, 2000.

[14] M.D. Fairchild. *Color appearance models*. John Wiley and Sons, USA, second edition, 2006.

[15] T. Young. Bakerian lecture. On the theory of light and colours. *Phil. Trans. R. Soc.*, 92:12–48, 1802.

[16] H. von Helmholtz. *Handbuch der physiologischen Optik*. Hamburg, Voss, Leipzig, Voss, 1st, 2nd, 3rd edition, 1866, 1896, 1911.

[17] R.W.G. Hunt and M.R. Pointer. *Measuring colour*. ISandT in Imaging Science and Technology. WILEY, fourth edition, 2011.

[18] J. Guild. *The Colorimetric Properties of the Spectrum*. Phil. Trans. Roy. Soc., London, 1931.

[19] H.S. Fairman, M.H. Brill, and H. Hemmendinger. How the CIE 1931 Color-matching Functions were Derived from Wright-Guild Data. *Col. Res. Appl.*, 22:11–23, 1997.

[20] M.H. Brill. How the CIE 1931 Color-matching Functions were Derived from Wright-Guild Data. *Col. Res. Appl.*, 23:259, 1998.

[21] G. Wyszecki and W.S. Stiles. *Color Science and Industry*. WILEY-New York, second edition, 2000.

[22] CIE. Colorimetry - Part 1/E: CIE standard colorimetric observer. Technical report, CIE, Vienna, 2006.

[23] CIE. *International Lighting Vocabulary*, volume 017-1987. CIE and IEC, 4th edition, 1987.

[24] D. MacAdam. Visual sesitivities to color differences in daylight. *J. Opt. Soc. Am.*, 32:247, 1942.

[25] D.B Judd and G. Wyszecki. *Color in Business, Science and Industry*. WILEY-New York, second edition, 1975.

[26] D. Judd. Ideal color space. *Color Engineering*, 8(2):37, 1970.

[27] Y. Nakano, R. Yamashita, Y. Fukuda, K.-I. Suehara, T. Yano. Uniform color space based on color vision mechanisms. In *9th Congress of the International Colour Association*, volume 4421, pages 291–294, 2002.

[28] CIE. CIE 15:2004 colorimetry, 3rd edition. Technical report, CIE, 2004.

[29] CIE. ISO 11664-5:2009 colorimetry – Part 5: CIE 1976 L*u*v* colour space and u', v' uniform chromaticity scale diagram. Technical report ISO/TC 274, CIE, 2009.

[30] J. Schanda. *Colorimetry: Understanding the CIE System*. John Wiley & Sons, 2007.

[31] A. Höpe, T. Atamas, D. Hünerhoff, S. Teicher, K.-O. Hauer. ARGon^3–"3D Appearance Robot–based Reflectometer Gonioreflectometer at PTB". *Rev. Sci. Instrum.*, 83(4), April 2012.

[32] K.-O. Hauer. Aufbau und Charakterisierung eines homogenen Strahlers für radiometrische Anwendungen. Diplomarbeit, Fachhochschule Lübeck, University of Applied Sciences, Dezember 2005.

[33] K.-O. Hauer, A. Höpe. High-grade uniform light source for radiometric and photometric applications. *MAPAN*, 24(3):175–182, 2009.

[34] ISO/CIE Standard, Wien. *CIE Colorimetry–Part 2: Standard Illuminants for Colorimetry*, 2007. ISO 11664–2.2007(E)CIE S 014-2E.2006.

[35] https://mitsubishielectric.com.

[36] A. Höpe, T. Atamas, D. Hünerhoff, S. Teicher, K.-O. Hauer. ARGon^3–"3D Appearance Robot–based Reflectometer Gonioreflectometer at PTB". In *Proceedings of NEWRAD 2011*, 2011.

[37] http://horiba.com.

[38] http://hamamatsu.com.

[39] http://keithley.com.

[40] S.B. Howell. *Handbook of CCD Astronomy.* Cambridge University Press, second edition, 2006.

[41] http://technoteam.de.

[42] L.Simonot, M. Hebet, D. Dupraz. Goniocolorimetry: From Measurement to Representation in the CIELAB Color Space. *Col. Res. and Appl.*, 36(3):169–178, June 2011.

[43] W.R. McCluney. *Introduction to Radiometry and Photometry.* Artech House, Boston, 1994.

[44] A. Höpe and K.-O. Hauer. Three-dimensional appearance characterization of diffuse standard reflection materials. *Metrologia*, 47(3):295, Februar 2010.

[45] Victor R. Weidner and Jack J. Hsia. Reflection properties of pressed polytetrafluoroethylene powder. *J. Opt. Soc. Am.*, 71(7):856–861, Jul 1981.

[46] W. Erb. Requirements for reflection standards and the measurement of their reflection values. *Applied Optics*, 14(2):493–499, February 1975.

[47] ISO: International Organisation for Standardization. GUM: Guide to the Expression of Uncertainty in Measurement, 1993.

[48] United Kindom Accreditation Service (UKAS). The expression of uncertainty and confidence in measurement. Technical report, UKAS, January 2007.

[49] National Institute of Standards and Technology. Guidelines for evaluating and expressing the uncertainty of NIST measurement results. Technical Report 1297, NIST, 2003. Technical.

[50] CIE, editor. *Proceedings of 2nd CIE Expert Symposium on mesurement uncertainty*, Braunschweig, Germany, 12-13 June 2006. CIE.

[51] D. Hünerhoff, U. Grusemann and A. Höpe. New robot-based gonioreflectometer for measuring spectral diffuse reflection. *Metrologia*, 43(2):S11, April 2006.

[52] R. Christoph, H. Neumann. Multisensor coordinate metrology. *CV cooporate Media*, 2007. ISBM 978-3-937889-66-5.

[53] Calibration Certificate 50735-PTB-12, August 2012.

[54] Performance report, May 2010.

[55] Calibration Certificate 87320-PTB-13, August 2012.

[56] S. Nevas, G. Wübbeler, A.Sperling, C.Elster and A. Teuber. Simultaneuous correction of bandpass and stray-light effects in array spectroradiometer data. *Metrologia*, 49:S43–47, 2012.

[57] S.G.R. Salim, N.P. Fox, W.S. Hartree, E.R. Woolliams, T.Sun and K.T.V. Grattan. Stray light correction for diode-array-based spectrometers using a monochromator. *App.Opt.*, 50(26):5130–5138, September 2011.

[58] S. Nevas, J. Gröbner. Stray light correction of array spectroradiometer data for solar UV measurements. UV News: the Official Newsletter of the Thematic Network for UV Measurements, 9,17-19 2013. ISBN 1456-2537.

[59] H.W. Engl, M. Hanke and A. Neubauer. *Regularization of Inverse Problems*. Kluwer Acadenic Publishers, 2000.

[60] H.W.Engl, M. Hanke, A. Neubauer. *Regularization of Inverse Problems*. Mathematics and Its Applications. Springer, 1996.

[61] A. Höpe, D. Hünerhoff, K.-O. Hauer. Robot–based Gonioreflectometer. In Low Kin Huat, editor, *Industrial Robotics: Programming, Simulation and Applications*. Pro Literatur Verlag, Germany / ARS, Austria, December 2006.

[62] G. Pfaff. *Special Effect Pigments*. Vincentz Network GmbH and Co. KG, Hannover, 2 Revised edition, 2008.

[63] DIN, Berlin. *DIN 55943:2001-10 Colouring materials – Terms and Definitions*, 2001.

[64] C.S. McCamy. Observation and measurement of the appearance of metallic materials. part ii. micro appaerance. *Col. Res. Appl.*, 23(3362-3373), 1998.

[65] N. Dekker, E.J.J. Kirchner, R. Super, G.J. van den Kieboom, R. Gottenbos. Total appearance diffrences for metallic and pearlescent materials: Contributions from color and texture. *Col. Res. Appl.*, 2010.

[66] American Society for Testing and Materials, West Conshohocken, PA. *ASTM D 16-08 Standard Terminology for Paint, Related Coatings, Materials, and Applications*, 2008.

[67] A. Argoitia, M. Witzman. Pigments exhibiting diffractive effects. In *45th Ann Techn. Conf. Proceedings*. Soc. Vacuum Coaters, 2002.

[68] P. Wissling et al. *Metallic effect pigments*. Vincentz Network, Hannover, 2007.

[69] R.M. Johnston. Geometric metamerism. *Color Eng.*, 54(3):42–47, 1967.

[70] H. Hemmendinger and R.M.Johnston. Goniospectrophotometric color measurement: use of the Triclac goniospectrophotometer. In *Color 69; Proceedings of the 1st AIC Congress*, volume 69, Stockholm, June 1969. 1st AIC Congress, Color.

[71] DIN, Berlin. *DIN 6175-1, Tolerances for automotive paints - Part 1: Unipaints*, 2009-07.

[72] American Society for Testing and Materials, West Conshohocken, PA. *ASTM E 2194-03 Standard Practice for Multiangle Color Measurement of Metal Flake Pigmented Materials*, 2003.

[73] American Society for Testing and Materials, West Conshohocken, PA. *ASTM E 2539-08 Standard Practice for Multiangle Color Measurement of Interference Pigmens*, 2008.

[74] American Society for Testing and Materials, West Conshohocken, PA. *ASTM WK 1164 New Standard Practice for Multiangle Color Measurement of Interference Pigmented Materials*, 2006.

[75] DIN, Berlin. *DIN 6175-2:2001-03 Farbtoleranzen für Automobillackierungen - Teil 2: Effektlackierungen*, 2001.

[76] R. Maisch and M. Weigand. *Perlglanzpigmente - Physikalische Grundlagen, Eigenschaften, Anforderungen*. Moderne Industrie, Landsberg am Lech, 1991.

[77] R. Glausch, M. Kieser, R. Maisch, G. Pfaff, and J. Weitzel. *Perlglanzpigmente*. Vincentz, Hannover, 1996.

[78] T. Atamas, K.-O. Hauer and A. Höpe. Appearance measurements of goniochromatic colours. In *Predicting Perceptions: Proceedings of the 3rd International Conference on Appearance*, pages 149–154. Lulu Press, Edinburgh UK, 2012.

[79] D.F. Vanderwerf. *Applied Prismatic and Reflective Optics*, volume PM200. SPIE PRESS BOOK, July 2010.

[80] T. Jaap. *Astronomical Polarimetry*. Cambridge University Press, 1996.

[81] D. Goldstein. *Polarized Light*. Marcel Dekker, Inc. All Rights Reserved, second revised and expanded edition, 2003.

[82] A.R. Jones. Light scattering for particle characterization. *Progress in Energy and Combustion Science*, 25(1):1 – 53, 1999.

[83] J.M. Bennett. *Handbook of Optics: Geometrical and Physical Optics, Polarized Light, Components and Instruments*, volume 1, chapter 12. Polarization. The McGraw-Hill Companies, Inc., New York, 3rd edition, 2010.

[84] F.E. Nicodemus, J.C. Richmond and J.J. Hsia. Geometrical considerations and nomenclature for reflectance. Technical report, American Society for Testing and Materials, 1977.

[85] P.J. Clarke. Surface colour measurements. Measurement Good Practice Guide 96, NPL, UK, May 2006.

[86] J.L. Gardner. Uncertainties in surface colour measurements. Measurement Good Practice Guide 95, NPL, UK, 2006.

[87] S. Bell. A Beginners Guide to Uncertainty in Measurement. Measurement Good Practice Guide 11, NPL, UK, 1999.

[88] J. Taylor, A.R. Hanson, P.J. Clarke, J. Campos Acosta, A. Pons, W. Czepluch, T. Jaaskelainen, J. Hiltunen, J. Gaudemer, O. Soares, J.L.C. Costa and L. Liedquist. Good practice guide to surface colour measurements. measurement good practice guide. EUR19553, European Commission, Luxembourg, 2006.

[89] J.L. Gardner. Uncertainties in interpolated spectral data. *J. Res. Natl. Inst. Stand.Technol.*, (108):69–78, 2003.

[90] International Organisation for Standardization, International Vocabulary of basic and general terms in metrology, 1993.

[91] P.J. Clarke, A.R. Hanson and J.F. Verrill. The determination of colorimetric uncertainties in the spectrophotometric measurement of colour. *Analytica Chimica Acta*, 380(2-3):277–284, 1999.

[92] J.F. Verrill, P.J. Clarke and J.O. Halloran. Study of improved methods for absolute colorimetry. study of colorimetric errors on industrial instruments. Report Fifth, NPL, 1997. COEM 2 report.

[93] ASTM. *Standard practice for computing the colors of objects by the CIE system*, ASTM E308-01 edition, 2001.

[94] Y. Ohno. A numerical method for color uncertainty. CIE x020, CIE Expert Symposium, Vienna, January 2001.

[95] E.A. Early, M.E. Nadal. Uncertainty analysis for reflectance colorimetry. *Col. Res. Appl.*, 2004.

[96] J.L. Gardner. Uncertainties in Color Measurements. Technical Report NMI TR8, National Measurement Institute Australia, Australia, 2005.

CURRICULUM VITAE

Name:	Tatsiana Wiegner (geb. Atamas)
Address:	Cyriaksring, 50 38118 Braunschweig Germany
Date of birth:	15.07.1981
Place of birth:	Baranovichy, Belarus
Nationality:	Belarussian
June 1999	High School "Lyceum No 1", Baranovichy, Belarus
Sept 2000 – Sept 2004	Bachelor degree in Physics Belarusian State University (`http://www.bsu.by/en/`), Minsk, Belarus
Sept 2004 – June 2005	Diploma in Physics, Belarusian State University (`http://www.bsu.by/en/`), Minsk, Belarus
Feb 2005 – May 2005	Intern in Belarusian State Institute of Metrology, Minsk, Belarus Division of Physical, Chemical and Optical Research
Aug 2005 – May 2010	Physics–Engineer in Belarusian State Institute of Metrology (BelGIM), NMI Belarus, Minsk, Belarus Division of Physical, Chemical and Optical Research `http://www.belgim.by/en`
June 2010 – Oct 2014	PhD studies in the Technischen Universität Braunschweig in collaboration with the Physikalisch–Technischen Bundesanstalt, Braunschweig Germany

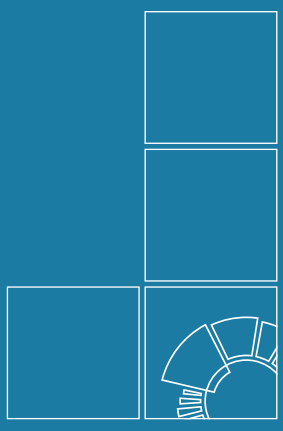

Herausgeber:
Physikalisch-Technische Bundesanstalt
Braunschweig und Berlin

Presse und Öffentlichkeitsarbeit

Bundesallee 100
38116 Braunschweig

Telefon: (05 31) 592-93 21
Telefax: (05 31) 592-92 92
www.ptb.de

Vertrieb:
Fachverlag NW in der
Carl Schünemann Verlag GmbH

Zweite Schlachtpforte 7
28195 Bremen

Telefon: (04 21) 369 03-0
Telefax: (04 21) 369 03-63
www.schuenemann-verlag.de